

Self-organized quantum wires on patterned GaAs(311)A and on unpatterned GaAs(100)

D I S S E R T A T I O N

zur Erlangung des akademischen Grades
doctor rerum naturalium
(Dr. rer. nat.)
im Fach Physik

eingereicht an der
Mathematisch-Naturwissenschaftlichen Fakultät I
Humboldt-Universität zu Berlin

von
MSc Wenquan Ma
geboren am 22.3.1968 in Gansu, VR. China

Präsident der Humboldt-Universität zu Berlin:
Prof. Dr. Jürgen Mlynek

Dekan der Mathematisch-Naturwissenschaftlichen Fakultät I:
Prof. Dr. Bernhard Ronacher

Gutachter:

1. Prof. Dr. K. H. Ploog
2. Prof. Dr. J. H. Wolter
3. Prof. Dr. W. Neumann

eingereicht am: 27, 02, 2001
Tag der mündlichen Prüfung: 24, 10, 2001

Zusammenfassung

In der vorgelegten Arbeit wurden zwei Arten von Quantendrahtstrukturen untersucht, die mittels Molekularstrahlepitaxie (MBE) hergestellt wurden. Erstens ist dies eine laterale Quantendrahtstruktur, die sich entlang einer Mesokante durch selektives Wachstum auf strukturierten GaAs (311)A-Substraten ausbildet. Zunächst wurden vertikal gestapelte Quantendrähte mit starker elektronischer Kopplung realisiert. Weiterhin wurden, unter Nutzung des amphoteren Einbaus von Si, p-i-n-Leuchtdioden mit einem einzelnen Quantendraht in der aktiven Zone hergestellt, die sich durch selektive Ladungsträgerinjektion in die Quantendrähte auszeichnen. Die Leuchtdioden wurden weitergehend mittels Mikrophotolumineszenz (μ -PL), Kathodolumineszenz (CL) und Elektronenstrahl-induziertem Strom (EBIC) charakterisiert. Zur Erklärung der selektiven Elektrolumineszenz (EL) wurde ein Modell, basierend auf der lateralen Diffusion von Elektronen und Löchern, vorgeschlagen. Für verspannte Systeme wurde der Einfluss von atomarem Wasserstoff auf das Wachstum von (In,Ga)As auf GaAs (311)A und die Bildung von lateralen Quantendrähten untersucht. Atomarer Wasserstoff spielt dabei die Rolle eines Surftandens und unterdrückt deutlich die Bildung von dreidimensionalen Inseln.

Zweitens wurde das Wachstum von verspannten (In,Ga)As-Schichten auf GaAs (100) untersucht. Es zeigte sich, dass die dreidimensionale Inselbildung durch die Wachstumskinetik bestimmt ist, und ein Übergang von symmetrischen zu asymmetrisch verlängerten Inseln bei Erhöhung der Wachstumstemperatur auftritt. Dieser Prozeß wird durch das Zusammenspiel von Oberflächen- und Verspannungsenergie bestimmt, wobei die experimentellen Befunde in guter Übereinstimmung mit den theoretischen Arbeiten von Tersoff und Tromp sind. Ausgehend von asymmetrischen (In,Ga)As-Inseln wurden selbstorganisierte Quantendrähte hergestellt, deren Homogenität und Länge sich durch Wachstum einer Vielschichtstruktur deutlich erhöhen. Strukturell wurden die (In,Ga)As-Quantendrähte mittels Rasterkraftmikroskopie (AFM), Röntgendiffraktometrie (XRD) und Transmissionselektronenmikroskopie (TEM) untersucht. Der laterale Ladungsträgeranschluss in den Quantendrähten zeigte sich deutlich in polarisationsabhängigen Photolumineszenz- und Magnetophotolumineszenzmessungen.

Abstract

The present work focuses on two types of quantum wire structures which were grown by molecular beam epitaxy (MBE). First, the sidewall quantum wires based on the selective growth on mesa stripe patterned GaAs(311)A are studied. Single stacked sidewall quantum wires with strong electronic coupling have been fabricated. p-i-n type LEDs of the quantum wires employing the amphoteric Si incorporation for p- and n-type doping on GaAs(311)A have been fabricated. Strong selective carrier injection into the quantum wires is observed in electroluminescence (EL) measurements. The samples are characterized by micro-photoluminescence (μ -PL), cathodoluminescence (CL), as well as electron beam induced current (EBIC) measurements. To account for the highly selective EL, a model is proposed, which is based on the lateral diffusion of electrons and holes resulting in self-enhanced carrier injection into the quantum wires.

Atomic hydrogen effects in the growth of (In,Ga)As on GaAs(311)A and its application to the sidewall quantum wire are investigated. It is found that atomic hydrogen suppresses island formation. Atomic hydrogen delays the relaxation by islanding thus playing the role of a surfactant.

Second, the growth of (In,Ga)As layers on GaAs(100) is investigated showing that the formation of coherent 3D islands is a kinetically limited process. The transition from square-shaped islands to elongated islands is observed by changing the growth temperature for the growth of (In,Ga)As single layers. The elongation of the islands is a tradeoff between the surface free energy and the strain energy. A quantitative comparison between the experimental results and the theoretical work done by Tersoff and Tromp shows a good agreement. Self-organized quantum wires based on elongated dislocation-free islands have been fabricated. The uniformity of the quantum wires is greatly improved by a superlattice growth scheme which also makes the wires much longer. The structural characterization of the quantum wires is performed by atomic force microscopy (AFM), x-ray diffractometry (XRD), and transmission electron microscopy (TEM). The lateral carrier confinement in the quantum wires is confirmed by polarization dependent PL and magneto-PL measurements.

Contents

Introduction	1
1 Quantum wires on patterned GaAs(311)A	8
1.1 Introduction to sidewall quantum wires	8
1.2 Strongly coupled sidewall quantum wires	12
1.2.1 Introduction	12
1.2.2 Fabrication	14
1.2.3 Results and discussion	14
1.3 p-i-n type LEDs of the sidewall quantum wires	17
1.3.1 Fabrication of p-i-n type LED	17
1.3.2 Injection EL	21
1.3.3 Selective carrier injection into the quantum wires	23
1.3.4 Electron beam induced current	28
1.3.5 A model for the selective EL	31
1.3.6 Stark effect of the sidewall quantum wires	35
1.4 Atomic hydrogen effect and its application to the sidewall quantum wires	40
1.4.1 Introduction	40
1.4.2 Results and discussion	41
2 Self-organized quantum wires on GaAs(100)	47
2.1 Shape transition	47
2.1.1 Growth mode	47
2.1.2 Surface morphology of (In,Ga)As single layers	48
2.1.3 RHEED characterization	53
2.1.4 Shape transition	59
2.2 Self-organized quantum wires	66
2.2.1 Fabrication of self-organized quantum wires	66

2.2.2	X-ray diffraction characterization	72
2.2.3	Results and discussions	82
2.3	TEM characterization	85
2.4	Lateral confinement of the quantum wires	88
2.4.1	Lateral confinement induced polarization anisotropy	88
2.4.2	Separation of strain and lateral confinement induced polarization anisotropy	89
2.4.3	Results and discussion	90
2.5	Piezoelectric effect	95
	References	101
	Acknowledgments	111
	List of Abbreviations and Symbols	113
	Publications	114
	Curriculum vitae	115
	Selbständigkeitserklärung	116

Introduction

With the refinement of crystal growth technologies, especially molecular beam epitaxy (MBE) and metalorganic vapor phase epitaxy (MOVPE), heteroepitaxial films with thickness accuracy on the atomic layer scale can be fabricated [1]. This opens up the possibility to fabricate novel electronic devices utilizing quantum size effects. If a thin semiconductor layer is grown between two semiconductor barriers with wider energy gap, one dimensional (1D) quantum confinement is achieved when the layer thickness is smaller than or comparable to the de Broglie wavelength of the electron. This is the quantum well structure in which carriers are confined in one dimension. The quantum confinement will modify the density of states affecting the electronic properties. Compared to conventional double heterostructure lasers, quantum well lasers exhibit superior characteristics such as ultra low threshold current density [2], less temperature dependence of the threshold current [3], narrow gain spectrum [4, 5], etc. Further reduction of the dimensionality will make these advantages more remarkable due to a more peaked energy dependence of the density of states [3, 4]. It is also expected that the exciton binding energy is enhanced with reducing the dimensionality [1]. The structures in which carriers are confined in two or three dimensions are the so-called quantum wires (1D free motion) or quantum dots (0D free motion). The density of states of electrons ρ_c for the bulk crystal (ρ_c^b), quantum well (ρ_c^{2D}), quantum wire (ρ_c^{1D}), and quantum dot (box) (ρ_c^{0D}) structures, respectively, are expressed as [3]

$$\rho_c^b(E) = \frac{(2m_c/\hbar^2)^{\frac{3}{2}}}{(2\pi^2)} E^{\frac{1}{2}}, \quad (1)$$

$$\rho_c^{2D}(E) = \sum_n \frac{m_c}{(\pi\hbar^2 L_z)} H(E - E_z(n)), \quad (2)$$

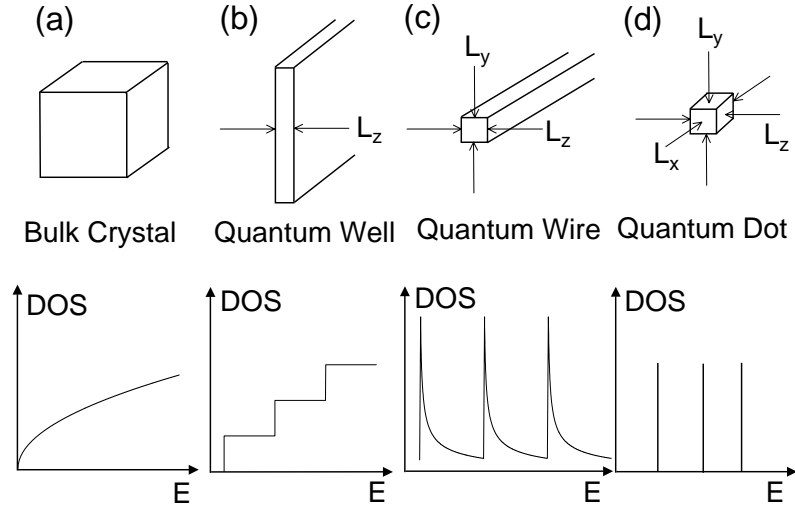


Figure 1: Schematic drawing of the physical shape and the corresponding density of states of electrons for bulk crystal (a), quantum well (b), quantum wire (c), and quantum dot (d).

$$\rho_c^{1D}(E) = \sum_{n,l} \frac{\left(\frac{m_c}{2\hbar^2}\right)^{\frac{1}{2}} / (\pi L_y L_z)}{[E - E_y(l) - E_z(n)]^{\frac{1}{2}}}, \quad (3)$$

$$\rho_c^{0D}(E) = \sum_{n,l,k} \frac{1}{(L_z L_y L_x)} \delta(E - E_x(k) - E_y(l) - E_z(n)). \quad (4)$$

Here, m_c is the effective mass of the electron; E is the energy measured from the bottom of the conduction band and $E(n), E(l)$, and $E(k)$ denote the quantized energy levels with quantum numbers n, l, k ; \hbar is the reduced Planck's constant; $H(E)$ is the Heaviside function, i.e., $E = 0$ for $E < 0$ and $E = 1$ for $E \geq 0$; L_x, L_y , and L_z denote, respectively, the thickness in the x, y , and z directions where the quantum confinement arises from and $\delta(E)$ is the delta function. The density of states of holes is analogous. Figures 1(a), (b), (c), and (d) schematically depict the physical shape and the corresponding density of states of electrons for bulk crystal, quantum well, quantum wire, and quantum dot structures, respectively. It can be seen that the reduced dimensionality results in a more peaked density of states.

In spite of the attractive properties of low dimensional structures, it is proved that the fabrication of quantum wire and quantum dot structures has always been a challenge for state-of-the-art crystal growth technology. There is a wide variety of methods for the fabrication of quantum wire and quantum dot structures. The conventional methods to fabricate quantum wire structures include mesa etching followed by a subsequent epitaxial regrowth [6]. The first evidence of the lateral quantum confinement was the observation of a blueshift of the cathodoluminescence peak for the mesa etched quantum wire [6]. However, the wet and dry chemical etchings always cause damages at the interfaces resulting in nonradiative centers. Therefore, this method is detrimental for device applications. Quantum wire structures have also been obtained by focused-ion-beam implantation of Ga atoms producing lateral potential barriers [7]. At present, the fabrication methods may be roughly classified in two groups: one is based on the selective growth on patterned substrates and the other is based on the self-organized formation of three dimensional (3D) islands. Here, we briefly introduce some typical methods for the fabrication of quantum wires. Of course, it is impossible to include all methods for the fabrication of quantum wires considering the very large amount of literature.

(a) Ridge quantum wire

The ridge quantum wire is formed by selective epitaxy on mesa stripe etched GaAs (100) substrates prepared by photolithography and reactive ion etching with SiCl_4 [8, 9]. The depth and width of the etched mesa is several μm . For the etched mesa stripe along the [011] direction, under certain growth conditions, (100)- $\{111\}$ B facet structures appear. When continuing the growth of GaAs, the (100) facet diminishes its width due to the migration of Ga adatoms from the $\{111\}$ B facets to the (100) plane resulting in a sharp ridge structure with $\{111\}$ B side-facets (the width of the ridge is typically about 20 nm in MBE) [9]. After the sharp ridge structure is formed, an AlAs/GaAs/AlAs quantum well structure is deposited, The quantum well on the top of the ridge is thicker than that on the $\{111\}$ B facets due to the migration of Ga adatoms from the $\{111\}$ B facets to the (100) plane and the different angles of the incoming Ga flux. Therefore, electrons and holes are laterally confined in the thicker GaAs region at the top of the ridge making this ridge structure acting as a quantum wire structure. Figure 2(a) schematically illustrates this process. This ridge quantum wire structure can be grown by MBE and MOVPE [8, 9]. For the mesa stripe oriented along the $[01\bar{1}]$ direction, $\{111\}$ A side-facets are formed and the quantum wire struc-

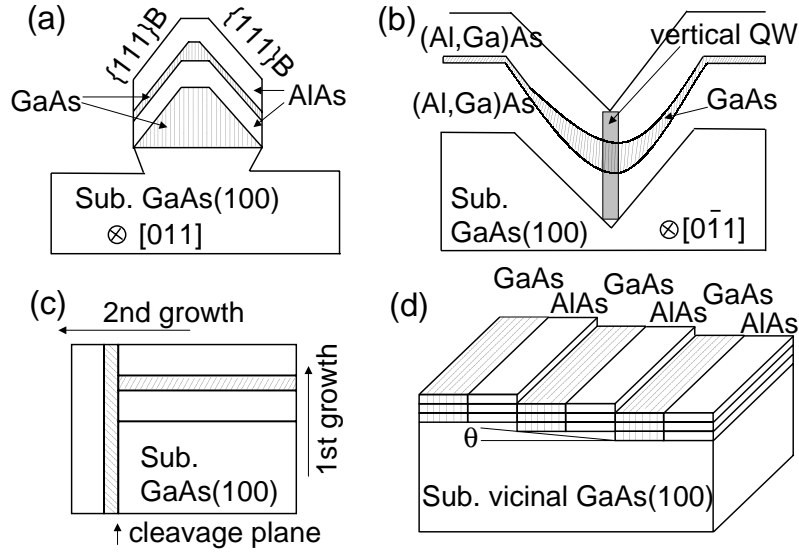


Figure 2: Schematic drawing of different methods for the fabrication of quantum wire structures. (a): ridge quantum wire; (b): quantum wire on V-grooved GaAs(100); (c): T-shaped edge quantum wire; (d): fractional layer superlattice quantum wire.

ture can similarly be realized [10]. However, experimental results indicate that the stripe orientation along the $[011]$ direction is better for the formation of quantum wire structures than that along the $[01\bar{1}]$ direction because, for the $[01\bar{1}]$ stripe orientation, some macrosteps are formed on the $\{111\}A$ planes resulting in kinks on the top of the (100) plane [10].

(b) Quantum wire on V-grooved substrate

Figure 2(b) schematically shows the quantum wire on V-grooved GaAs(100) [11]. The V-groove oriented along the $[01\bar{1}]$ direction is patterned by photolithography and conventional wet chemical etching. The V-groove is usually several μm wide and deep. For the $[01\bar{1}]$ oriented V-groove, $\{111\}A$ crystal planes are formed on the sides of the V-groove and the bottom of the V-groove is the (100) plane. During the growth of GaAs, because the growth rate is larger for the (100) plane than for the $\{111\}A$ sidewalls, the bottom of the V-groove becomes thicker leading to a crescent-shaped GaAs region. The carriers are laterally confined in the thicker crescent-shaped GaAs region due to the lateral thickness variation of the quantum well which serves as a lateral potential well [12]. Therefore, the crescent-shaped quantum well acts as a

quantum wire. For the vertical stack of the quantum wires, a relatively thick (Al,Ga)As layer has to be grown to sharpen the V-groove bottom because the $\{111\}$ A crystal planes grows faster. In this quantum wire structure, a vertical quantum well is inserted, as depicted in Figure 2(b). Because Ga adatoms migrate faster towards the bottom of the V-groove than Al adatoms, the Al concentration at the bottom is lower than in the surrounding regions resulting in a vertical quantum well. A significant linear polarization anisotropy of photoluminescence (PL) and PL excitation (PLE) was observed for the quantum wire structure on V-grooved substrates demonstrating an effective lateral carrier confinement [13]. V-groove quantum wire lasers have been fabricated [14]. This quantum wire structure is very successful.

(c) T-shaped edge quantum wire

T-shaped edge quantum wires are formed by overgrowth of a cleaved edge [15]. As schematically illustrated in Figure 2(c), a conventional quantum well structure is first grown on the GaAs (100) substrate. Then the substrate is cleaved in the ultra high vacuum chamber. The cleaved cross-sectional edge is treated as a new surface for the growth of the second quantum well. Electrons and holes can be confined at the intersection region of the edge (T-junction) where the quantum energy has a minimum [16]. Very small scale 1D structures can be fabricated because the size of the edge quantum wire depends on the thickness of the quantum well which can be well controlled. It was reported that the lasers made from this quantum wire operate at 4.2 K [17]. However, because the quantum wire is formed on the very narrow cleavage plane, further processing of this quantum wire structure by photolithography and metallization is difficult.

(d) Fractional layer superlattice quantum wire on vicinal GaAs(100)

The fractional layer superlattice quantum wire is formed on a vicinal surface by step flow growth [18, 19]. The vicinal surface, where the surface orientation is not along one of the primary crystallographic axis, but is cut several degrees off is composed of periodic step arrays with monolayer height. As schematically shown in Figure 2(d), the width of the step p is determined by the miscut angle θ by the relation: $p = h / \tan \theta$, where h is the monolayer height (for the vicinal GaAs(100), $h = 2.83 \text{ \AA}$). For example, on the vicinal GaAs (100) surface, a miscut angle of 2° corresponds to a surface step width of 81 \AA . Under step flow growth, the impinging atoms tend to migrate and deposit at the step edge rather than to deposit on the top of the terrace. In this case, the surface morphology during growth propagates rather than changes periodically, therefore, the reflection high energy electron diffraction

(RHEED) oscillations do not occur. If a fraction of one monolayer material like GaAs is deposited under the step flow growth conditions, the deposited material will cover a fraction of the step terraces near the step edges. Afterwards, if another material like AlAs is deposited also under step flow growth mode, the material will cover the remaining area of the terrace. If the quantity of the two deposited materials exactly amounts to one monolayer, the step edges will be the same as those before the depositions. Periodic repetition of this process generates a lateral superlattice in which the two materials are vertically stacked. Electrons and holes are confined laterally producing a 1D quantum wire structure. For the current MBE equipment, it is difficult to control the deposited materials to be exactly one monolayer. A slight deviation away from one monolayer per cycle will result in a large tilt of the stacked materials, therefore, this structure is also called tilted superlattice quantum wires [19]. However, it has been shown that this structure is not truly 1D. This is caused by two reasons. One is that the steps on the vicinal surface are not ideal resulting in a nonuniform distribution of the lateral confinement regions. The other reason is the intermixing between the two deposited materials resulting in a reduction of the energy barrier height. If the tilt of the stacked materials is varied continuously by controlling the amount of the deposition per cycle, a structure called serpentine superlattice quantum wire can be obtained [20]. Compared to the tilted superlattice structure, the 1D characteristic of the serpentine superlattice quantum wire structure is reinforced because the carriers are mainly confined in the thicker middle part of the serpentine-shaped region and the tilt sensitivity is partly avoided [20].

(e) Strained quantum wires based on 3D islands

In Stranski-Krastanov systems, on the one hand, great efforts have been devoted to the fabrication of quantum dots which are based on symmetrically shaped 3D islands [21, 22, 23, 24, 25]; on the other hand, elongated islands have been reported [26, 27, 28, 29, 30]. These elongated islands may be used as templates to fabricate quantum wires. However, these elongated islands usually have a large size nonuniformity which can wash out the expected 1D saw-tooth like density of states. Therefore, it is very critical to improve the size uniformity of the elongated islands. In the meantime, the physical process which governs the formation of the elongated islands is still discussed.

In this work, we investigate some properties and fabrication technologies of quantum wire structure from two aspects. Two kinds of quantum wire structures are prepared by MBE. The first one is the quantum wire struc-

ture based on selective epitaxy on stripe-patterned GaAs (311)A substrates. For this part (Chapter 1), we focus on some applications of this quantum wire structure instead of its formation mechanism, which has been investigated in previously published articles. A p-i-n type light emitting diode of the sidewall quantum wires has been fabricated. A strongly selective carrier injection into the quantum wires is observed and its mechanism is discussed. Strongly coupled sidewall quantum wires have also been fabricated. The role of atomic hydrogen during the growth of (In,Ga)As on GaAs(311)A and its influence on the formation of the strained sidewall quantum wires are investigated. Second (Chapter 2), we have developed a self-organized quantum wire structure based on elongated dislocation-free islands formed during growth of (In,Ga)As/GaAs on GaAs(100). The uniformity of the quantum wire array is greatly improved by a superlattice growth scheme, which also makes the wires much longer. The quantum wires are characterized and the lateral carrier confinement is confirmed. The shape transition from symmetric to elongated islands is understood by the investigation of (In,Ga)As single layer growth. Finally, the work is summarized.

Chapter 1

Quantum wires on patterned GaAs(311)A

1.1 Introduction to sidewall quantum wires

Experimentally it was found that, during the MBE growth of GaAs, a fast growing sidewall is formed on mesa stripe patterned GaAs (311)A substrates along the $[01\bar{1}]$ direction in the sector towards the next (100) plane, while the opposite sidewall in the sector towards the next (111) plane shows a slow growing (111) side facet [31]. For mesa stripes oriented along the $[\bar{2}33]$ direction on patterned GaAs(311)A, two slow growing side facets towards the next $\{331\}$ planes are observed. The fast growing sidewall shows a smooth and convex-curved surface profile without facetting. It was shown that the formation of the fast growing sidewall is due to the preferential migration of Ga adatoms from the mesa top and the mesa bottom towards the sidewall, while the slow growing sidewall is formed due to the preferential migration of adatoms away from the sidewall generating a concave surface profile at the mesa bottom [31]. Figures 1.1(a) and (b) show the schematic illustration of the growth mode on patterned GaAs (311)A substrates with mesa stripes oriented along the $[01\bar{1}]$ and $[\bar{2}33]$ direction, respectively. Two samples composed of layered GaAs (100 nm)/(Al,Ga)As (100 nm) heterostructures with 30 nm thick GaAs buffer layers were grown on 400 nm high mesa stripes patterned on GaAs (311)A substrates along the $[01\bar{1}]$ and the $[\bar{2}33]$ directions. The AFM studies confirmed the surface morphology illustrated in Figures 1.1(a) and (b) [32]. The selectivity of growth for the formation of

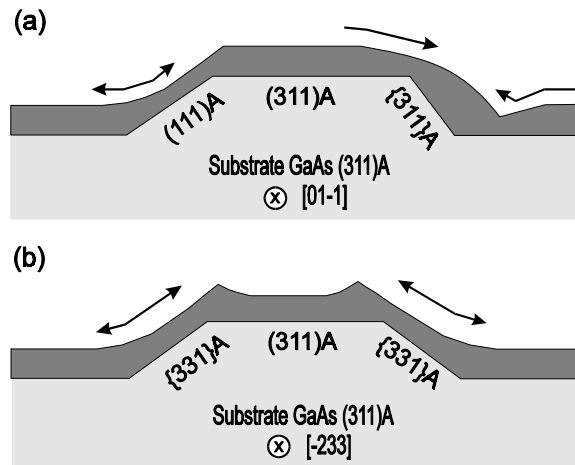


Figure 1.1: Schematics of the growth mode on patterned GaAs (311)A substrates with mesa stripes oriented along the $[01\bar{1}]$ (a) and $[\bar{2}33]$ (b) directions. The arrows indicate the preferential migration of Ga atoms. (R. Nötzel, et al., [31]).

the fast growing sidewall is stable when the misalignment angle of the patterned mesa stripe with respect to the $[01\bar{1}]$ direction is smaller than 20° [33].

The fast growing sidewall is only formed on the patterned GaAs (311)A substrate with mesa stripes oriented along the $[01\bar{1}]$ direction in the sector towards the next (100) plane. For other mesa stripe patterned substrates like GaAs (211)A, (411)A, (511)A, and (311)B, only slow growing sidewalls are formed, which was evidenced by the AFM investigations of the samples overgrown with layered GaAs/(Al,Ga)As on these substrates [35]. The evolution of the fast growing sidewall was studied by TEM for the GaAs/(Al,Ga)As multilayer structure grown on the 400 nm high mesa stripe [34]. Figures 1.2(a) and (b) show the cross-sectional TEM images with low and high magnification, respectively. It is seen that the fast growing sidewall diminishes its size with GaAs overgrowth to end up with a convex curved surface profile at the bottom of the sidewall. The GaAs layers at the bottom and the top of the mesa are thinner than that at the sidewall due to the preferential migration of Ga adatoms from the mesa top and bottom to the sidewall. No variation of the (Al,Ga)As layer thickness is found due to the small surface migration length of Al adatoms. Recently, the evolution of the

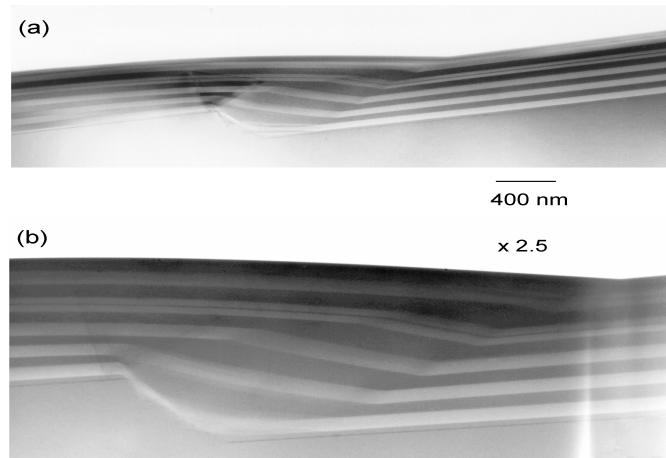


Figure 1.2: Cross-sectional TEM image viewed along the $[01\bar{1}]$ direction showing the evolution of the fast growing sidewall of the mesa stripe along the $[01\bar{1}]$ direction on patterned GaAs(311)A (a). In (b), the scale is magnified. The dark and white regions correspond to the GaAs and (Al,Ga)As layers, respectively. (R. Nötzel, et al., [34]).

fast and slow growing sidewalls were also studied by cross-sectional AFM showing good agreement with the cross-sectional TEM results [36].

The unique growth mechanism for the formation of the fast growing sidewall on stripe patterned GaAs(311) can be applied to fabricate quantum wire structures when the height of the mesa stripe is in the quantum size regime of 10-20 nm. In Ref. [37], a quantum wire sample with a 6 nm thick GaAs quantum well inserted in two 50-nm thick $Al_{0.5}Ga_{0.5}As$ barrier layers grown on a 50 nm thick GaAs buffer layer and capped with 20 nm GaAs was grown. The height of the mesa stripe was 15 nm. Figures 1.3(a) and (b) show the AFM image and the cross-sectional TEM image at the fast growing sidewall [37]. The TEM image [Figure 1.3(b)] shows that the fast growing sidewall has a convex curved surface profile with the GaAs quantum well thickness of about twice that of the adjacent well. CL spectra reveal two separated peaks, and spatially resolved CL images show that the peak at the low-energy side is due to the fast growing sidewall. It was also shown that the quantum well close to the edge of the sidewall is thinner. The lateral carrier confinement in the sidewall quantum wires was confirmed by linear-polarization dependent μ -PL measurements [38], by the appearance of the one dimensional subband

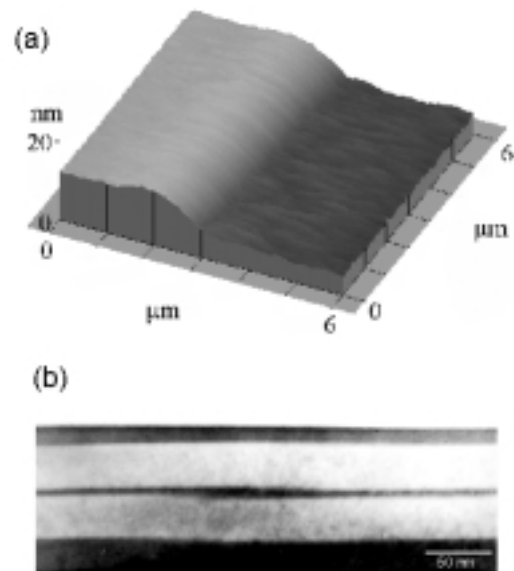


Figure 1.3: (a) AFM image of the convex curved sample surface of the fast growing sidewall with a height of 10-15 nm on patterned GaAs(311)A. (b) cross-sectional TEM image viewed along the $[01\bar{1}]$ direction. (R. Nötzel, et al., [37]).

structure in PL excitation (PLE) investigations performed by scanning near field optical microscopy [39], and by the observation of the transition from 2D to magnetic confinement in magneto-PL spectroscopy [35].

1.2 Strongly coupled sidewall quantum wires

1.2.1 Introduction

Strongly quantum-mechanically-coupled low-dimensional structures, in which the wave function is delocalized, are very important not only for fundamental research but also for potential applications in devices. They play a unique role for studying the tunneling and coupling of electronic states in different dimensions [40]. For quantum dot structures with quantum confinement in three dimensions, the behavior is similar to “artificial atoms” [41, 42]. Therefore, strongly coupled quantum dot structures are appropriate systems to study the bonding and anti-bonding states of the “artificial atoms” and their dependence on the separation between the dots, which is well described in the textbooks of quantum mechanics. Thus, such a study offers new insights into the fundamental physics of coupled quantum objects [41]. Strongly coupled quantum wire structures have also been used to investigate tunneling and coupling between one-dimensional states [40]. On the other hand, from the device application point of view, the coupled low-dimensional structures are unique candidates. Strongly coupled quantum dots have been utilized to fabricate semiconductor lasers whose performance is improved due to the enhanced active volume [23, 24]. Strongly coupled low-dimensional structures can also be used to make ultrafast optoelectronic devices utilizing quantum oscillations [43]. For example, supposing there are two quantum wells separated by a barrier: a wide one and a narrow one. We denote the wavefunction and the eigenenergy of the uncoupled wide quantum well as Ψ and E , respectively, and those of the narrow well with a prime, i.e., Ψ' and E' , respectively. If the barrier is very thin and the two wells are sufficiently close, an overlap of wavefunctions between the two wells will occur due to electronic coupling. In the meantime, if an electric field is applied to the strongly coupled structure, the two lowest energy levels for electrons (E_1 and E'_1) can be adjusted to resonance. Far away from resonance, the wavefunctions of the electrons are localized in one well or the other, while when resonance is approached, the wavefunctions of electrons become more delocalized (the energy levels for holes are still nonresonant). In this case, if an electronic wave packet is prepared in one well, for example, by an ultrafast laser pulse, the probability density of the electron wavefunctions will oscillate back and forth between the two quantum wells resulting in an oscillating electric dipole radiation. This process can be understood very well by

the time-dependent Schrödinger equation. The time evolution of the wave packet for electrons in the two coupled quantum wells is expressed as

$$\Psi(z, t) = \Psi_1(z, t)e^{-iE_1t/\hbar} + \Psi'_1(z, t)e^{-iE'_1t/\hbar}, \quad (1.1)$$

where z denotes the direction of wave packet oscillation. The probability density $P(z, t)$ is then given by

$$P(z, t) \equiv |\Psi(z, t)|^2 = |\Psi_1(z, t)|^2 + |\Psi'_1(z, t)|^2 + 2\text{Re}\Psi_1^*\Psi'_1e^{-i(E_1-E'_1)t/\hbar}. \quad (1.2)$$

Therefore, the probability density oscillates coherently in time between the two extreme values $(|\Psi_1| - |\Psi'_1|)^2$ and $(|\Psi_1| + |\Psi'_1|)^2$ with a period given by

$$\tau_{coh} = h/\Delta E, \quad (1.3)$$

where ΔE is the energy difference $|E_1 - E'_1|$ and $\tau_{coh}/2$ is called the tunneling time [44]. Such coherently oscillating waves have been experimentally observed [43]. A new quantum-effect electronic device called quantum field-effect directional coupler, which is based on the ideas discussed above, has been proposed [45].

However, the fabrication of strongly coupled quantum wire and quantum dot structures has always been a great challenge in spite of their attractive potential device applications. In fact, much efforts have been devoted to the fabrication of strongly coupled quantum dots and quantum wires. Strongly coupled quantum dots have been fabricated by the cleaved edge overgrowth method [41]. However, this method is very time-consuming and complicated and thus might not be a practical choice in terms of device application. Electronically coupled InAs quantum dots formed by the coherent Stranski-Krastanov growth have also been fabricated [46, 47, 48, 49]. However, the size and the distribution of the self-organized quantum dots are still difficult to control in a satisfactory way. Strong electronic coupling has also been demonstrated for V-grooved quantum wires [50, 51, 52]. In spite of the success, V-groove quantum wires can be fabricated to be strongly coupled, but the wires then are different. This restriction arises from the growth mechanism because, in order to obtain identical wires, the barrier layer which separates the top wire and the bottom wire should be thick enough to recover the “V” shape [12]. Therefore, for strongly coupled V-groove quantum wires, the top quantum wire is slightly thinner and wider than the bottom one [50, 51]. However, the largest electronic coupling is achieved when the two quantum wires are identical.

It has been shown that the sidewall quantum wires on patterned GaAs (311)A substrates can be vertically stacked [53]. One experimental fact is that no variation of the thickness of the (Al,Ga)As layer across the patterned edge is observed due to the small surface migration length of Al atoms while a thicker fast growing GaAs sidewall is formed at the edge due to the preferential migration of Ga atoms. Therefore, the sidewall quantum wires may be strongly coupled with identical shape. For this purpose, a series of samples has been grown.

1.2.2 Fabrication

The semi-insulating GaAs (311)A substrates were patterned with mesa stripes of 15-20 nm depth oriented along the $[01\bar{1}]$ direction by standard photolithography and wet chemical etching. After cleaning with concentrated sulphuric acid and rinsing in de-ionized water, the sample was transferred into the MBE growth chamber. The native oxide was desorbed at 580°C and then the substrate was heated to 610°C for the growth of the other layers. After the deposition of a 50 nm thick GaAs buffer layer, a 50 nm thick $Al_{0.3}Ga_{0.7}As$ barrier was grown followed by two 3 nm thick GaAs quantum wells separated by a $Al_{0.3}Ga_{0.7}As$ barrier. Then a 50-nm-thick $Al_{0.3}Ga_{0.7}As$ layer was grown and finally, a 20-nm-thick GaAs cap layer was deposited. We grew four samples denoted as cpl1, cpl2, cpl3, and cpl10 corresponding to the $Al_{0.3}Ga_{0.7}As$ barrier thickness of 1, 2, 3, and 10 nm, respectively. The width of the patterned mesa stripe is $75\ \mu\text{m}$ for samples cp1 and cp3, and $16\ \mu\text{m}$ for samples cp2 and cp10. The As_4 to Ga flux ratio is about 5 and the growth rate of GaAs and AlAs is $0.5880\ \mu/\text{h}$ and $0.2732\ \mu/\text{h}$, respectively. Before growing this series of samples, the growth rates of GaAs and AlAs were carefully calibrated by x-ray diffraction. The whole growth process was monitored in situ by RHEED showing a clear (8×1) surface reconstruction during the growth of GaAs.

1.2.3 Results and discussion

Figure 1.4 depicts the AFM image of sample cp12 measured at the fast growing sidewall, showing a convex curved surface profile. The samples were characterized by μ -PL which uses a microscope to focus the optical excitation and/or detection on the sample surface. The spot diameter on the sample was reduced by a confocal imaging system to about $2\ \mu\text{m}$. The Ar^+ laser (514.5

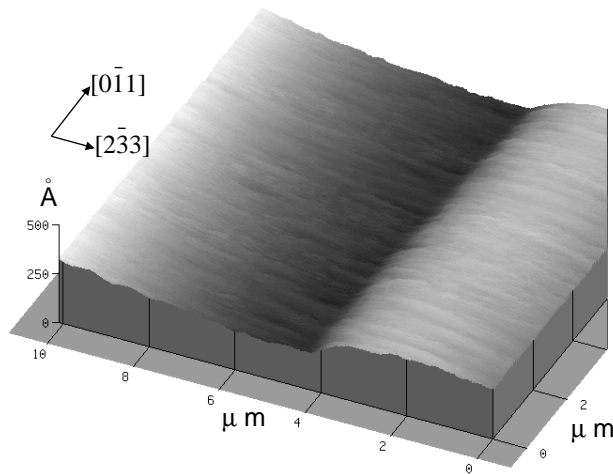


Figure 1.4: AFM image of the fast growing sidewall of sample cpl2 showing a convex curved surface profile.

nm) was used as excitation source for the μ -PL measurements. Figure 1.5 shows the μ -PL spectra of the series of samples taken at 10 K with the laser spot exciting at the fast growing sidewall. The peak at the low-energy side is attributed to the quantum wire peak and that at high-energy side to the quantum well. The linewidth of the quantum wire peak is about 10 meV for all samples indicating a good quality of the quantum wires. The deterioration of the shape of the quantum well peak for samples cp2 and cp10 might be due to the smaller width of the patterned stripes. The μ -PL spectra clearly show a redshift of the quantum wire peak with decreasing (Al,Ga)As barrier thickness. This redshift is due to the electronic coupling. The (Al,Ga)As barrier of sample cp10 is 10 nm and, thus there is almost no coupling while the other three samples are strongly coupled. When the (Al,Ga)As barrier thickness varies from 10 to 1 nm, the quantum wire peak redshifts by 18 meV.

Although the redshift of the quantum wire peak with decreasing barrier thickness proves that strong electronic-coupling between the two stacked quantum wires has been achieved, it is difficult to know whether or not the two strongly coupled quantum wires are identical. For this purpose, the Schrödinger equation should be solved numerically and then the obtained energy values should be compared with the PL peak energy positions. Pre-

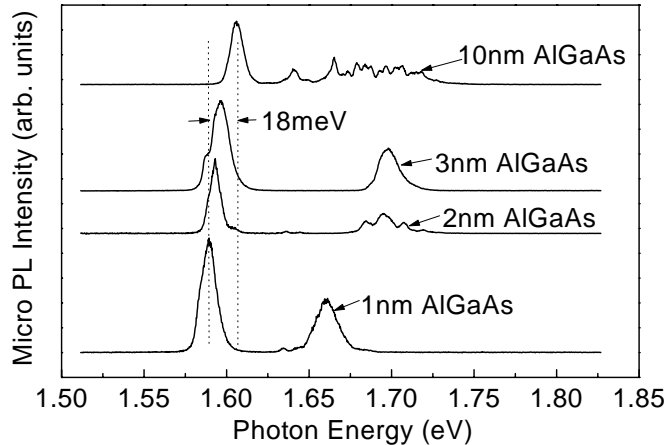


Figure 1.5: μ -PL spectra of the series of samples with (Al,Ga)As barrier thickness of 10, 3, 2, and 1 nm, respectively, measured at the fast growing sidewall at 10 K. The peak at the low energy side is attributed to the quantum wire.

vious investigations show that the PL peak energy position of the sidewall quantum wire corresponds to that of a quantum well whose thickness is twice the nominal thickness of the grown quantum well [37]. Therefore, as an approximation, we treat the sidewall quantum wire as a 6 nm thick quantum well and solve the one-dimensional Schrödinger equation numerically. The used conduction to valence band offset ratio is 60:40, which is widely accepted for the (Al,Ga)As/GaAs system [54]. The $Al_xGa_{1-x}As$ band gap at the Γ point, E_g , at room temperature ($T=300$ K) is $E_g = 1.424 + 1.247x$ eV for $0 < x < 0.45$, and the temperature dependence of the energy gap at the Γ point is obtained by the linear dependence: $\frac{dE_g}{dT} = (-3.95 - 1.15x) \cdot 10^{-4} eV/K$ [55]. The obtained band gap of $Al_{0.3}Ga_{0.7}As$ is 1.92266 eV at 10 K. For GaAs, the band gap at 10 K is 1.51875 eV, which is obtained by the empirical relation $E_g = 1.519 - 5.408 \times 10^{-4} T^2 / (T + 204)$ [55], where the unit of the energy is eV and that of the temperature is K. The different effective mass of the heavy hole m_{hh}^* for the [311] orientation has been taken into account [56]. For GaAs(311)A, $m_{hh}^* = 0.49m_0$, while $m_{hh}^* = 0.34m_0$ for GaAs(100), where m_0 is the free electron mass. The effective mass of heavy holes for $Al_{0.3}Ga_{0.7}As$ on GaAs(311)A is $m_{hh}^* = 0.601m_0$, which is obtained by interpolating the values between GaAs ($0.49 m_0$) and AlAs ($0.86m_0$) according

to the Al composition x [57]. The effective mass of the electron, which is not related to substrate orientation, is $m_e^* = 0.0665 + 0.0835x$ in units of m_0 for $Al_xGa_{1-x}As$. Figure 1.6 shows the calculated energy value of the $e_1 - hh_1$ transition and the PL peak energy position in dependence on the (Al,Ga)As barrier thickness for the quantum well and the quantum wire. The peak position of the quantum wells is obtained by measuring at the flat part of the mesa because the quantum well at the edge is thinner than that in the flat part [37]. For the quantum well, the calculation and the experiments show an agreement except for the sample with 10-nm thick barrier. The discrepancy between the calculation and the experiments could be caused by the exciton effect which is not taken into account in the calculation. The exciton binding energy increases for narrower quantum wells [58], therefore, for the 10 nm barrier sample whose wavefunction is localized in the two quantum wells, the exciton binding energy is larger than that of the strongly coupled samples whose wavefunctions are delocalized in the two quantum wells. For the quantum wire, except for the sample with 1 nm thick barrier, an agreement between the calculation and the experiments is obtained considering the small corrections caused by exciton effects. The μ -PL measurements seem to support that the two strongly coupled quantum wires are identical, even when the barrier is only 2 nm thick. However, a definite conclusion needs further evidences, such as TEM and PLE, etc.

1.3 p-i-n type LEDs of the sidewall quantum wires

1.3.1 Fabrication of p-i-n type LED

We have fabricated p-i-n type light emitting diodes (LEDs) with the sidewall quantum wires and observed strongly selective carrier injection into the quantum wires [59]. Also, in order to investigate the Stark effect of the strongly coupled wires, the sidewall quantum wires are single-stacked in the intrinsic region. Amphoteric incorporation of Si is used for the p- and n-type doping. Before we discuss the fabrication process of the sidewall quantum wire LED, two things should be explained in advance. First, appropriate thicknesses of the undoped (Al,Ga)As layers in the intrinsic region are important. Figure 1.7 depicts the schematic cross-section of the structure of the sidewall quantum wire LED. For the quantum confined Stark effect, the

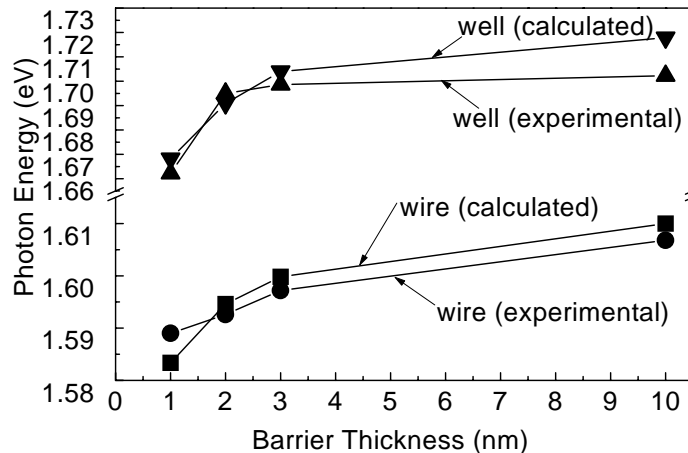


Figure 1.6: Quantum wire and quantum well peak position versus the (Al,Ga)As barrier thickness for the series of samples. The experimental and calculated values, respectively, are obtained from μ -PL measurements and by solving the Schrödinger equation numerically.

maximum electric field is usually smaller than 1×10^5 V/cm. Therefore, the (Al,Ga)As layers should not be too thin; otherwise, the generated electric field will be too strong resulting in a breakdown of the p-i-n junction. It may be a good choice that several volts of the applied bias generate the electric field of 5×10^4 V/cm. When $v_{ext} - v_{bi}$ is 1.5, 2, and 3 V, the obtained thickness of the undoped (Al,Ga)As layer is 150, 200 and 300 nm, respectively, where v_{ext} and v_{bi} denote the applied bias and the built-in voltage, respectively. Therefore, the (Al,Ga)As layers are selected to be 200-nm thick.

Second, the amphoteric Si doping on GaAs(311)A should be discussed. Si is an n-type dopant for [100]-oriented GaAs in MBE growth and the conventional p-type dopant is Be, while it was found that the conduction type of Si can be p- and n-type on GaAs (311)A substrates, depending on the growth conditions [60]. The advantage of the replacement of Be by Si for the p-type doping is to avoid the strong segregation of Be. P-type doping of Si on GaAs(311)A can be achieved at higher growth temperature and/or lower V_4 to III flux ratio, while n-type doping can be accomplished at lower growth temperature and/or higher V_4 to III flux ratio. The GaAs buffer layer grown at higher substrate temperature has a better surface morphology, therefore,

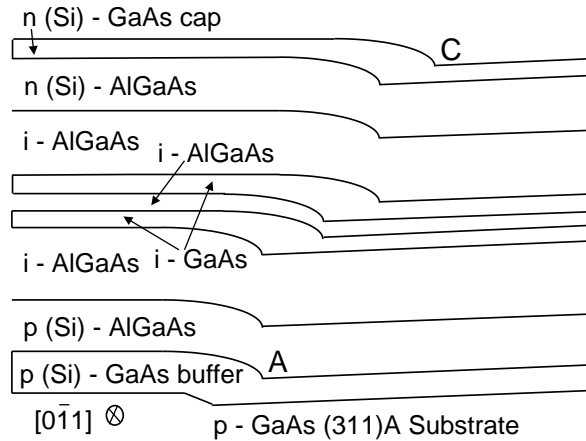


Figure 1.7: Schematic drawing of the structure of the p-i-n type LED of the sidewall quantum wire. The denotations of A and C are for the discussion in 1.3.4.

a p-type GaAs buffer layer grown at higher temperature is preferential to a n-type buffer grown at lower temperature. This is the reason why a p-type GaAs (311)A substrate is selected for the LED structure. The phase diagram for the conduction type of Si doping on GaAs(311)A in [60] shows that the conduction conversion between p- and n-type is quite abrupt. The amphoteric incorporation behavior of Si on GaAs(311)A is as yet not well understood, but the possible mechanism might be related to the microscopic corrugation-like reconstruction of the GaAs (311)A surface [60].

The p-type GaAs (311)A substrates were patterned with mesa stripes of $75 \mu\text{m}$ width and 17 nm depth oriented along the $[0\bar{1}1]$ direction by standard photolithography and wet chemical etching. After cleaning with concentrated sulphuric acid and rinsing in de-ionized water, the sample was transferred into the MBE growth chamber. The native oxide was desorbed at 580°C . The Si-doped 50 nm thick $\text{p}^+ (1 \times 10^{18} \text{ cm}^{-3})$ GaAs buffer layer was grown at 610°C for the sake of better surface morphology. The As_4 to Ga flux ratio was about 5 so that Si is incorporated as an acceptor. The intrinsic layers were grown at the same conditions and are comprised of two 200 nm thick $\text{Al}_{0.3}\text{Ga}_{0.7}\text{As}$ layers interspersed by a stack of two 3-nm -thick GaAs quantum well layers separated by an $\text{Al}_{0.3}\text{Ga}_{0.7}\text{As}$ barrier. We grew four samples among which the only difference is the thickness of the $\text{Al}_{0.3}\text{Ga}_{0.7}\text{As}$

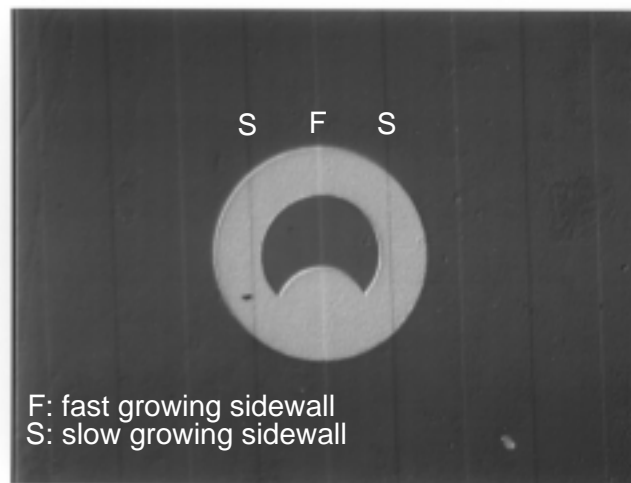


Figure 1.8: Microscopic image of the photolithographic mask pattern projected onto the surface of the as-grown samples for the fabrication of the small contacts.

barrier inserted in between the two GaAs layers. The four samples with the $Al_{0.3}Ga_{0.7}As$ layer thickness of 1, 2, 3, and 10 nm are denoted as pin1, pin2, pin3 and pin10, respectively. After growth of the intrinsic layer, the substrate was cooled down to $490^{\circ}C$ and, simultaneously, the As_4/Ga flux ratio was increased to about 20 in order to obtain n-type doping by Si for the following 100 nm n- ($0.6 \times 10^{18}cm^{-3}$) $Al_{0.3}Ga_{0.7}As$ layer capped by a 40 nm n^+ - ($1 \times 10^{18}cm^{-3}$) GaAs contact layer. The as-grown structures were processed into circular mesas which are etched down to the p- $Al_{0.3}Ga_{0.7}As$ layer. Ohmic Au/Be ring contacts were fabricated on the mesa top and ohmic Au/Ge contacts were prepared on the backside of the substrate by the techniques of metal evaporation and photolithography. The contact points (similar to the bonding area) were fabricated with a two-component silver-filled epoxy which was hardened at $150^{\circ}C$ for about 15 minutes. After the hardening, the epoxy points become conductive. Two kinds of mesas with the inner diameter of the ring of 120 and 220 μm were utilized. Figure 1.8 shows the microscopic images of the photolithographic mask pattern projected onto the surfaces of the as-grown samples for the fabrication of the small ring contacts. The patterned stripes after the overgrowth can be seen clearly, and “F” and “S” in the two images denote fast-growing and slow-growing sidewalls, respectively. For the small ring contacts with the inner diameter

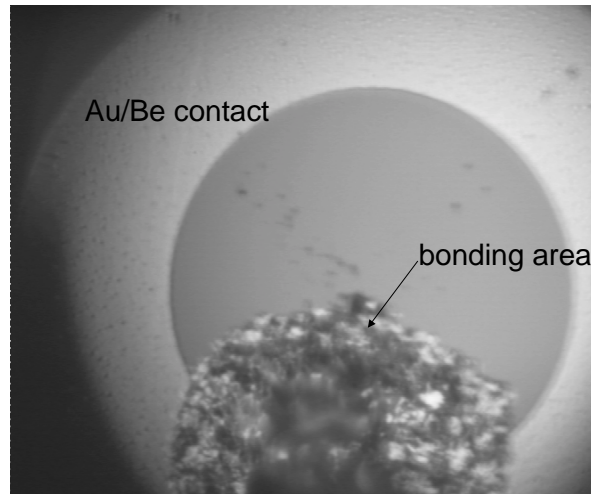


Figure 1.9: Top view of the processed mesa diode with the small ring contacts viewed through an optical microscope.

of $120\ \mu\text{m}$ (Figure 1.8), the photolithographic alignment is adjusted so that there is only one fast growing sidewall within the inner part of the ring contacts. Figure 1.9 shows the top view of the processed mesa diode with the small ring contacts viewed through an optical microscope.

1.3.2 Injection EL

Electroluminescence (EL) refers to excitation by a voltage applied to a luminescent substance. In order to convert the electric energy from the applied voltage into radiation, usually three sequential processes are involved: excitation by the applied field, energy transport and radiative de-excitation [61]. There are several mechanisms of EL [61, 62]. Here we focus on injection EL in a p-n junction (p-i-n junction is similar). In this case, the excitation first injects minority charge carriers to become “hot” carriers. After excitation it is necessary to transport the excitation energy to a region where radiative de-excitation, which may be inter- or intraband transition, can occur. This process can be understood clearly using a band model. At zero bias, which corresponds to the equilibrium condition, the Fermi level of the p-n junction is horizontal and continuous across the junction, determining the majority carrier densities (electrons on the n-side and holes on the p-side).

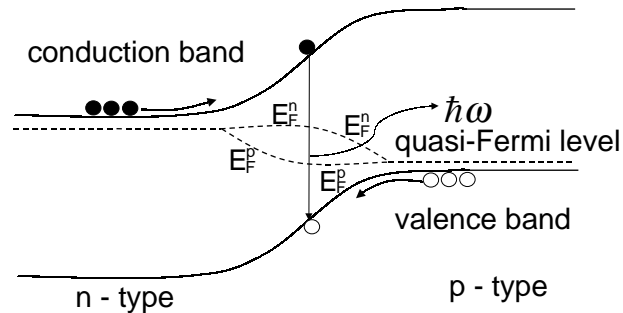


Figure 1.10: Schematic illustration showing the process of injection EL in a p-n junction biased in the forward direction using the band model.

When a forward bias is applied, the built-in voltage is diminished and more carriers can then cross the reduced barrier. After traversing the barrier, the injected carriers become minority carriers. In this case, the applied forward bias separates the Fermi levels and the concentration of free minority carriers can be described by a quasi-Fermi level. Here we denote E_F^n and E_F^p the quasi-Fermi levels for electrons and holes, respectively. The change of the quasi-Fermi level depends on the position. For instance, in the diffusion region of holes (located near the n-side), because the concentration of electrons is very high, the change of the quasi-Fermi level of electrons can be neglected and the quasi-Fermi level of electrons E_F^n can be regarded as constant. However, the concentration of holes is very small in this region. Therefore, the quasi-Fermi level of holes E_F^p varies drastically. When the holes are injected into the n-type part from the p-type part, their concentration is decreased due to recombination. In the n-side region far away from the boundary of the n-side, the concentration of non-equilibrium holes attenuates to zero and therefore, the quasi-Fermi level of the holes equals that of the electrons, i.e., $E_F^p = E_F^n$. The case for electrons can be analyzed analogously. Figure 1.10 schematically shows the process of injection EL in a p-n junction biased in the forward direction using the band model.

1.3.3 Selective carrier injection into the quantum wires

The EL properties were examined for all samples. Strongly selective carrier injection into the quantum wires were observed for all samples. The use of a single stack of quantum wires enhances the overall efficiency of the LED, however, it is not relevant to the selective carrier injection discussed here. At low temperatures and small injection currents, the EL of our quantum wire LED solely originates from the single stack of quantum wires within the inner ring contacts without detectable emission from the surrounding quantum wells. Although the EL from the quantum wells increases relative to that from the quantum wires with increasing temperature, the EL emission density, i.e., intensity per unit area in the quantum wire regions, is still two orders of magnitude larger than that in the well regions even at room temperature. The spatially well defined emission pattern from the quantum wires is directly observed through an optical microscope as a bright line within the otherwise dark mesa.

Here we focus on sample pin2 for the discussion of the EL properties. Figure 1.11 shows the EL spectra for increasing forward bias detected at 10 K through a confocal imaging system with the diameter of the optical probe area of 10 μm . Starting from the onset of the EL at about 1.8 V, strong emission is observed solely from the quantum wire up to a forward bias of 1.9 V (0.7 mA). With increasing forward bias from 2.1 V (1.3 mA) to 2.3 V (3.2 mA), a weak emission from the quantum wells appears. Figure 1.12 shows the dependence of the EL peak intensities of the quantum wires and quantum wells on the forward bias displayed on logarithmic scale (a) and linear scale (b). The EL peak intensities of the quantum wires and quantum wells increase almost linearly with current in the measured regime. The absolute current values, however, may vary by several mA from measurement to measurement and after subsequent sample cooling, most probably due to persistent photoconductivity effects in the (Al,Ga)As layers at low temperatures. The selective carrier injection into the quantum wires is most effective at the onset of the EL emission and can be clearly seen in Figure 1.12(a) (logarithmic scale). With increasing forward bias, the EL emission from the quantum wells grows in intensity more slowly compared to that of the quantum wires, which can be seen clearly from Figure 1.12(b) (linear scale). The blueshift and linewidth broadening of the quantum wire and quantum well EL peaks with increasing forward bias are attributed to band filling effects.

Selective carrier injection into the quantum wires is observed up to room

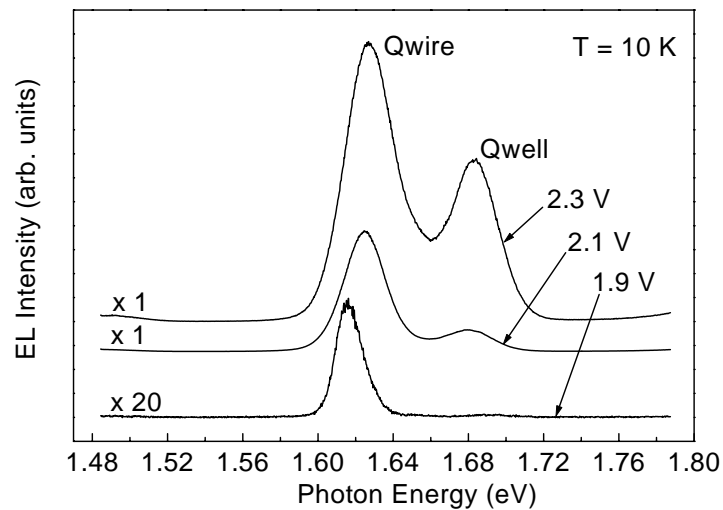


Figure 1.11: EL spectra of the quantum wire LED detected at 10 K for increasing forward bias.

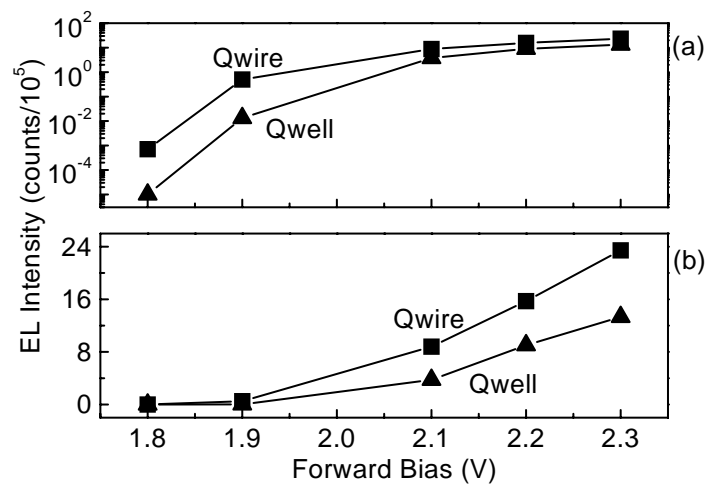


Figure 1.12: EL emission intensity from the quantum wire and quantum well versus the applied forward bias drawn in logarithmic (a) and linear scale (b).

temperature. Figure 1.13 shows the EL spectra as a function of temperature keeping the injection current fixed at about 5 mA. With increasing temperature, the selectivity of the EL emission is gradually reduced. This is attributed to carrier heating which increases the carrier injection into the quantum wells relative to that into the quantum wires. The nonequilibrium carriers should adhere to the Fermi-Dirac distribution resulting in a larger possibility of recombination for electrons and holes in quantum wells at higher temperature. Therefore, with increasing temperature, the quantum well peak becomes stronger. However, if we take into account the area ratio of the quantum well to the quantum wire, i.e., the diameter of the optical probe area (about $10\ \mu\text{m}$) divided by the effective quantum wire width of about 50 nm, and assume a comparable radiative efficiency of the quantum wells and quantum wires (indicated by the comparable intensity ratio of the quantum well to quantum wire emission at 10 K and room temperature in $\mu\text{-PL}$), the EL intensity per unit area and the electron-hole pair density for the quantum wire position at room temperature are still about two orders of magnitude larger than that of the quantum wells. With increasing temperature, the EL efficiency is reduced by increased non-radiative recombination channels as its selectivity. The redshifts of the quantum well peak and quantum wire peak at higher temperature are attributed to the shrinkage of the band gap. The inset of Figure 1.13 depicts the current-voltage characteristic of the quantum wire LED measured at room temperature. The I-V characteristic follows the exponential relation $i_0 = e^{\frac{eV}{kT}}$ in the transition region corresponding to very low injection current. When the injected carrier density is small and diffusion-limited, the minority carrier current is expressed as [61]

$$I = en\left(\frac{D}{\tau}\right)^{\frac{1}{2}}\left(e^{\frac{eV}{kT}} - 1\right), \quad (1.4)$$

where n is the density of excess minority carriers, τ is their lifetime, and D is their diffusion constant, which is related to the drift mobility μ by $D = \frac{kT}{e}\mu$. At higher applied voltage, the carrier motion is determined by the electric field, not by diffusion, and equation (1.4) does not apply [61].

As a consequence of the high emission density, the EL emission of the quantum wires is directly visible through an optical microscope as a bright line inside the ring contact. Figures 1.14(a) and (b) show the images of the EL through an optical microscope measured at 10 K and at room temperature, respectively, for the small mesa (the inner diameter of the ring contact is $120\ \mu\text{m}$). At low temperature [Figure 1.14(a)], the bright quantum wire EL is

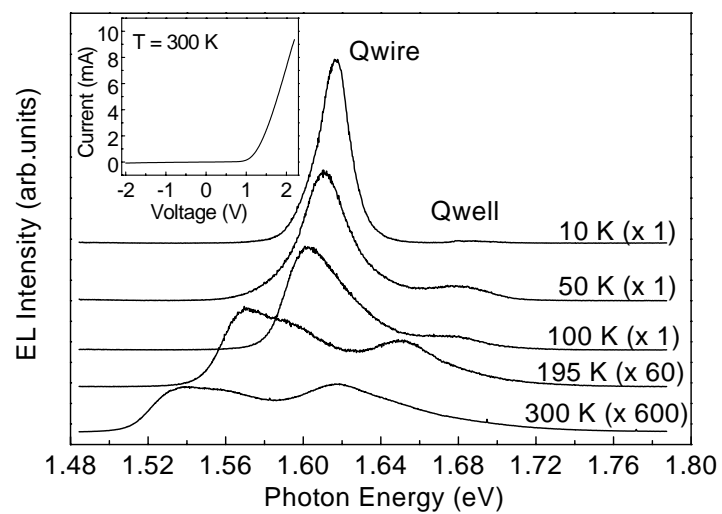


Figure 1.13: EL spectra of the quantum wire LED for about 5 mA forward current between 10 K and room temperature. The inset shows the current-voltage characteristic at room temperature.

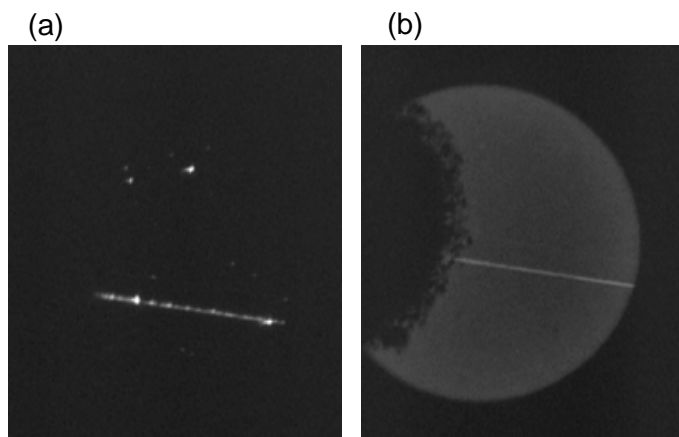


Figure 1.14: Images of the EL through an optical microscope (a) at 10 K and (b) at room temperature. The inner diameter of the ring contact is 120 μm.

seen with several bright spots along its line, which also appear in the quantum well regions. These bright spots are attributed to several cluster-like defects in the quantum wires and quantum wells involving regions of lower band gap energy compared to that of the surrounding quantum wire and quantum well regions. Therefore, similar selective carrier injection is assumed to apply for these clusters. But the energy difference between these cluster-like defects and the surrounding quantum wire and well regions is only several meV, which is much smaller than the energy difference of 70 meV between the quantum wire and the quantum-well peaks. Therefore, the EL emission from these localized clusters vanishes at about 50 K due to the thermally activated escape of the injected carriers, while that of the quantum wires persists up to room temperature. Consequently, the spatial homogeneity of the EL emission of the quantum wires at room temperature in Figure 1.14(b) becomes much more uniform compared to that at low temperatures due to the suppression of the EL emission from the cluster-like defects. To get a more direct impression of the EL emission from the quantum wires, we recorded two images [Figures 1.15(a) and (b)] viewed through an optical microscope and measured at room temperature. Figure 1.15(a) shows the top view of a small mesa of the quantum wire LED illuminated with white light, but no forward bias is applied. Figure 1.15(b) shows the same image, with a forward bias of 1.9 V applied. The EL emission from the quantum wires is only seen as a bright line when the forward bias is applied.

As discussed in section 1.1, the quantum wires are formed at a fast growing sidewall. To address the question about the EL properties of the slow growing sidewall, an optical microscope image of the EL from the large mesa (the inner diameter of the ring contact is $220 \mu\text{m}$) measured at 10 K is shown in Figure 1.16. The slow growing sidewall is imaged as a dark line indicating that there is no EL emission coming from the slow growing sidewall, while the fast growing sidewalls still demonstrate EL emission as two bright lines. This indicates that selective carrier injection only occurs in the fast growing sidewalls. The distance between the slow growing sidewall and the fast growing sidewall is $75 \mu\text{m}$, which is just the width of the patterned stripe of the substrate. Figure 1.16 clearly shows the difference of the EL properties between the fast growing and slow growing sidewalls, which is due to the absence of the growth selectivity for the slow growing sidewall.

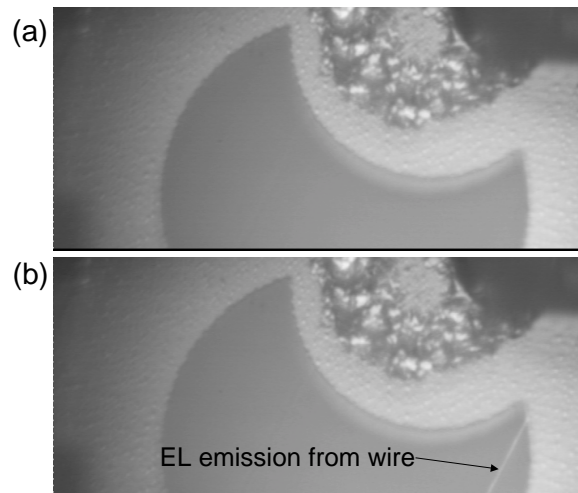


Figure 1.15: (a) shows the top view of a small mesa of the quantum wire LED at room temperature illuminated with white light, but no forward bias is applied. (b) shows the same image, but 1.9 V forward bias is applied.

1.3.4 Electron beam induced current

In order to account for the selective carrier injection into the quantum wire, electron beam induced current (EBIC) measurements, which are very sensitive to the carrier capture, were performed for the series of p-i-n type LED samples. The technique of EBIC has been widely used for characterization of semiconductor materials and structures [63, 64, 65]. It can provide spatially resolved information about extended defect properties and recombination center distributions and is very useful for the investigation of electrically active inhomogeneities in as-grown as well as in processed materials [66]. For the measurement of EBIC, the formation of a depletion layer built in by Schottky barrier or p-n junction is indispensable. This technique utilizes the imaging of the electron beam induced current between two sample contacts as a function of incident electron beam position. When the sample is irradiated by electrons, the generated electron-hole pairs are separated by the built-in electric fields. Then carriers redistribute within and outside the field of the depletion region to minimize their free energy. This relaxation from a configuration of high concentration near the generation point occurs through all available current paths and some of them produce the charge-collection

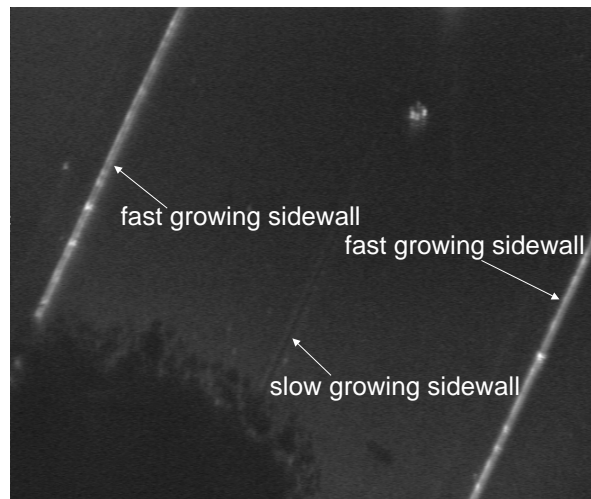


Figure 1.16: Images of the EL through an optical microscope at 10 K. The inner diameter of the ring contact is $220 \mu\text{m}$. No EL emission is observed from the slow growing sidewall.

current or EBIC current in an external circuit which, after amplification, is used to form an EBIC image [66, 67]. For a p-n junction, the built-in electric field always points from the n-type part to the p-type part, therefore, the direction of the EBIC current flow is also from n-type to p-type. There are different geometries for observing EBIC. The schematic drawing of the EBIC geometry employed in our experiments is shown in Figure 1.17. EBIC is very sensitive to the presence of dislocations, strain, damage, doping variations, compositional variations (band gap), and width variations of the depletion region of the respective p-n junction. Anything modifying recombination lifetime due to the variation of carrier capture can result in a local variation of the EBIC signal producing a corresponding contrast. For example, dislocations decrease the locally induced current and are imaged as dark regions in EBIC images [63, 64]. The disadvantage of EBIC microscopy is that the measured EBIC current integrates over the whole layer and over different contributions. Since it is difficult to distinguish between different contributions, the resulting EBIC contrast is hard to interpret clearly.

EBIC measurements were performed for all the p-i-n type LED samples. Because of the disadvantage mentioned above, some details of the EBIC results of our p-i-n type LED samples are not yet well understood. Here, we focus our discussion on sample pin1. Figures 1.18(a), (b) (the bottom part)

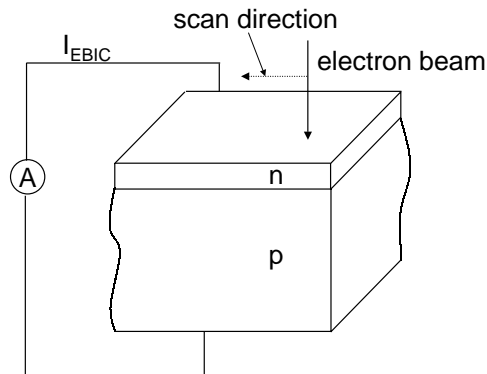


Figure 1.17: Schematic drawing of the experimental setup of EBIC microscopy.

and (c) depict the EBIC images of sample pin1 taken at 5 K with an applied forward bias voltage of 1.45, 1.5 and 1.55 V, respectively. The top part of Figure 1.18(b) shows the CL-intensity mapping for a CL detection energy set to the quantum wire peak position. Three dark stripes denoted as A, B and C are observed indicating regions with lower EBIC current compared with the surrounding neighborhood. To clarify the origin of the contrast, we varied the excitation depth by varying the electron beam energy. For the excitation with low-energy electrons (not shown here), only the regions B and C are observed. Moreover, a comparison of the secondary electron image with the EBIC one reveals that region C appears at a surface edge corresponding to the patterning position of the sample after the growth. With increasing excitation energy of the electrons, region A appears. Therefore, regions C and A are attributed to the mesa edge regions on the surface after and before overgrowth, respectively, approximately corresponding to the positions denoted as C and A in Figure 1.7. As discussed above in 1.3.1, the sidewall quantum wires are formed on patterned substrates. The corresponding wet chemical mesa-etching gives probably rise to an accumulation of nonradiative centers in particular at the mesa edges. Therefore, the EBIC current is decreased due to the enhanced carrier capture by these nonradiative centers. Consequently, the distance between the regions A and C of the EBIC images suggests a lateral shift of the mesa edge of about $3 \mu\text{m}$ during the growth of the p-i-n structure. This observation is consistent with TEM

results of a threefold stacked sidewall quantum wire system grown under similar conditions as the present p-i-n structures [53]. The respective TEM images reveal a lateral movement of the mesa edge during the deposition of the GaAs quantum wells due to the accumulation of material at the fast growing sidewall. The angle between the shift direction and the sample surface amounts to about 12° . Since the shape of the deposited layers does not change for the MBE growth of (Al,Ga)As, the shift angle should be nearly constant for various GaAs/(Al,Ga)As structures. Assuming a movement of the mesa edge during the growth of the p-i-n structure discussed above under the same angle we obtain indeed a lateral shift of the edge of about $3 \mu\text{m}$. From Figure 1.18(b), it can be seen that the spatial position of the quantum wire related CL emission corresponds to region B of the EBIC image indicating that region B is due to the sidewall quantum wire. With increasing forward bias voltage, the EBIC contrast of this region becomes darker and wider indicating an enhancement of carrier capture with a subsequent radiative and/or nonradiative recombination in the vicinity of the wire, which is not observed for the surrounding quantum well regions. The reason for this enhanced carrier capture in the quantum wire region with increasing forward bias is explained by the model proposed in the following paragraph. To get an impression about the contrast variation in the quantum well and quantum wire, the solid line in Figure 1.19 displays a linescan of the EBIC signal along the path marked as a white line in the EBIC image of the inset of Figure 1.19. The applied forward bias amounts to 1.53 V. The open circled curve in Figure 1.19 shows the CL emission in the quantum wire region. It is seen that the spatial position of the quantum wire emission corresponds to the position of the EBIC minimum confirming that region B in the EBIC image is due to the quantum wire. The contrast variation between the wire region and the well region is only about 3%.

1.3.5 A model for the selective EL

It should be noted again that the inner diameter of the small ring contacts is $120 \mu\text{m}$ and there is only one stack of the quantum wires in such a large area. This suggests that the observed selective EL emission is a strong effect. Before presenting our model to explain the strong EL selectivity in the present quantum wire LED, several alternative mechanisms have to be discussed. First, enhanced carrier capture in the quantum wires due to larger layer thicknesses. However, such an enhanced carrier capture would equally

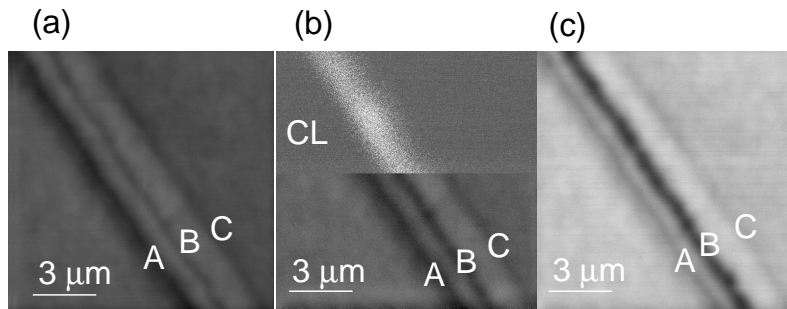


Figure 1.18: (a), (b) (the bottom part) and (c) depict the EBIC image of sample pin1 taken at 5 K with the applied forward bias of 1.45, 1.5 and 1.55 V, respectively. The acceleration voltage of electrons is 10 kV. The top part of (b) shows the CL-intensity mapping detected at the quantum wire peak position. The region B is attributed to the quantum wire region.

apply to μ -PL and CL measurements [37]. If it were true, we should observe such strong enhancement of the quantum wire emission for μ -PL and CL measurements. However, the μ -PL and CL measurements of the series of LEDs and of undoped reference structures always reveal strong emission from the quantum well for comparable electron-hole pair generation densities with similar radiative efficiency. This fact indicates that the injection mechanism for PL is different from that for EL. The principal difference between EL and PL is that, for the former case, electrons and holes are injected separately from the n-type region and p-type region, while for the latter case the photon-generated electrons and holes diffuse together from the surface [61, 62]. As the EBIC results indicate, the carrier capture in the quantum wire region is enhanced when increasing the applied forward bias. This point suggests that the operation of light-emitting devices based on lateral nanostructures, i.e., quantum wires and quantum dots, crucially depends on the underlying mechanism for carrier injection and capture. These mechanisms

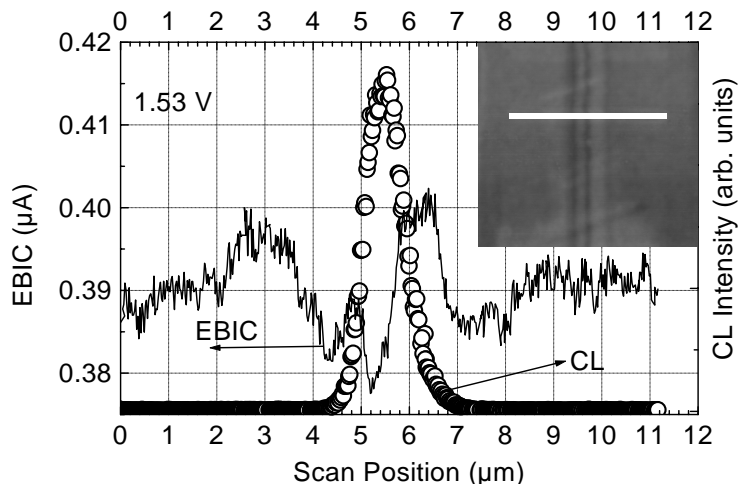


Figure 1.19: EBIC linescan (solid line) and CL linescan for sample pin1 taken at 5 K with the applied forward bias of 1.53 V. The inset shows the corresponding EBIC image and the white line depicts the linescan position.

may be remarkably different from beam excitation techniques, such as PL or CL, usually employed to characterize optical properties.

Second, reduced Al composition of the (Al,Ga)As barriers in the quantum wire regions providing injection channels of lower band gap energy. In fact, this injection mechanism has been employed to account for the selective carrier injection observed for the MOVPE-grown V-groove quantum wire structures [68]. The reduced Al composition at the top of the V-groove quantum wires, i.e., the vertical quantum well [schematically drawn in Figure 2(b)], plays a crucial role in guiding the carriers into the quantum wire regions. However, spatially resolved CL spectroscopy of the (Al,Ga)As barriers shows a negligible variation of the band gap energy, i.e., Al composition across our MBE-grown quasi-planar sidewall quantum wires. Moreover, the small 500 nm periodicity, used for the V grooves of Ref. [68], has been shown to result in almost complete suppression of the quantum well PL for our sidewall quantum wires [53] due to efficient diffusion of free carriers into the wires (the diffusion length is in the μm range) without the necessity of selective injection.

Third, nonuniform doping. As we discussed in 1.3.4, the EBIC measurements, which are very sensitive to lateral potential modulations due to

nonuniform doping (or Al composition) as well as carrier capture in the intrinsic region and neighboring doped layers, reveal a contrast variation in the quantum wire region of at most several percent. Finally, the vertical asymmetry of V-groove structures (the quantum wires are closer to the bottom contact than the quantum wells) has been considered in 4 μm pitch V-groove quantum wires showing a much smaller degree of EL selectivity [69]. However, our sidewall quantum wires are quasi-planar in geometry (for T-shaped quantum wires, no explanation has been given for the selective carrier injection at low temperatures in Ref. [17]). From the above discussion, we exclude structural nonuniformities or carrier capture mechanisms due to the larger layer thickness in the wire region to account for the observed EL selectivity in our sidewall quantum wire LED and propose the following model.

Starting from a homogeneous separate injection of electrons and holes from the n-type and p-type regions into the quantum wells and the quantum wires, the carriers in the quantum wells diffuse laterally as free electrons and holes or excitons into the wires over distances within their diffusion length because the energy level in the quantum wire is lower than that of the quantum well. From the fraction of electrons and holes diffusing separately, more electrons are trapped in the quantum wire regions due to their larger migration length. Therefore, the wires become negatively charged so that they effectively attract holes and, most importantly, reduce their injection barrier for the holes into the wire region. Namely, there is a strong selective attraction for holes into the quantum wire region and the consequence is the observed selective EL emission from the quantum wires. This reduction of injection barrier for holes into the wire region results in an enhanced carrier capture in the wire region for EL, as indicated by the EBIC measurements. Figure 1.20 schematically illustrates the whole process based on the lateral diffusion of electrons and holes in the quantum well leading to selective carrier injection into the quantum wire. The same mechanism explains the bright EL spots at low temperatures from any cluster-like defects having a locally reduced band gap energy. Hence, unlike the beam excitation techniques, such as PL and CL, the lateral diffusion of electrons and holes in EL affects the injection mechanism itself by increasing the current in the wire region. In addition, the fraction of electrons and holes diffusing separately is enhanced in EL due to their separate injection, while for optical and beam excitation the generation of electrons and holes is correlated in space and time enhancing the probability for exciton formation. The result is selective carrier injection into the quantum wires with a steeper increase of the quantum wire EL

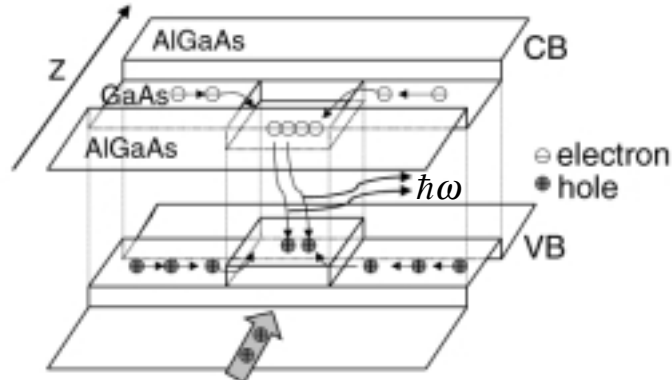


Figure 1.20: Schematic illustration of the lateral diffusion of electrons and holes in the quantum well leading to selective carrier injection into the quantum wire. Z denotes the growth direction and the horizontal direction is across the wire region, and the vertical one is energy.

compared to that of the quantum wells as a function of forward bias. As we mentioned above, two stacked or even more stacked quantum wires make no difference with one quantum wire in terms of selective carrier injection. This indicates that the selective EL is an intrinsic characteristic of the fast-growing sidewall quantum wire structures suggesting a promising potential application for optoelectronic devices.

1.3.6 Stark effect of the sidewall quantum wires

When electric fields are applied perpendicular to a semiconductor quantum well structure, the optical absorption, reflection and PL properties will be changed. A significant redshift of the exciton absorption can be observed. This effect is called the quantum confined Stark effect (QCSE) [1]. This effect can be employed to make optical modulators and switches since the optical absorption is modified by the applied electric field [70]. For a quantum wire or quantum dot structure, confinement potentials arising in two or three dimensions result in a larger oscillator strength due to enhanced excitonic effects [71]. Therefore, the QCSE in quantum wire [72, 73] or quantum

dot structures could be employed for making optoelectronic nanostructure devices. Furthermore, it is predicted that electroabsorption in quantum wires and quantum dots will be reinforced due to their enhanced oscillator strength [71].

We use the series of p-i-n type LED structures to investigate the behavior of the strongly coupled quantum wires under vertically applied electric field, i.e., the QCSE of the strongly coupled quantum wires by μ -PL spectroscopy. The μ -PL measurements were performed with an Ar⁺ laser excitation at 10 K. The spot diameter on the sample was reduced by a confocal imaging system to about 2 μ m. Figure 1.21(a) shows the dependence of μ -PL spectra on the externally applied bias measured at the fast growing sidewall for sample pin2. It can be clearly seen that the intensity of the quantum wire peak is comparable to that of the quantum well peak and no selective emission from the quantum wires is observed for PL measurements. This point has been discussed in 1.3.5. When the applied bias changes from 1.6 to -0.4 V, significant redshifts are observed for the quantum wire peak and the quantum well peak. The built-in voltage for the series of LEDs is 1.6 V. Therefore, when the applied bias changes from 1.6 to -0.4 V, the electric field is increased. It is observed that the linewidth of the quantum wire peak and the quantum well peak increases with increasing electric field. For a quantum well structure, this can be explained by an enhanced recombination lifetime of excitons due to the increase of the spatial separation of electrons and holes when increasing the applied electric field [74]. Such an increased broadening of the exciton linewidth was also observed in a short-period GaAs/(Al,Ga)As superlattice structure and explained by enhanced interface roughness scattering of electronic states due to Wannier-Stark localization [75]. The increased slope at the high energy side is attributed to the doped (Al,Ga)As layer, while such a tendency is completely quenched for the EL spectra as shown in Figures 1.11 and 1.13. The reason is that electrons and holes only recombine in the intrinsic region due to separated injection for EL, but the recombination occurs in the intrinsic layers as well as in the doped layers for PL. Figure 1.21(b) shows the μ -PL spectra measured at the fast growing sidewall of sample pin1 at different bias. The linewidth of the quantum wire peak of samples pin2 and pin1 at flat band condition (with the forward bias of 1.6 V) is 13 and 15 meV, respectively. Compared to sample pin1 [Figure 1.21(b)], the quantum well peak of sample pin2 [Figure 1.21(a)] becomes deteriorated, while the quantum wire peaks of the two samples still show a reasonable shape.

Figures 1.22(a), (b) and (c) depict the energy position of the quantum

well peak with respect to the applied electric field for the samples pin10, pin2 and pin1, respectively, and correspondingly, Figures 1.22(d), (e) and (f)

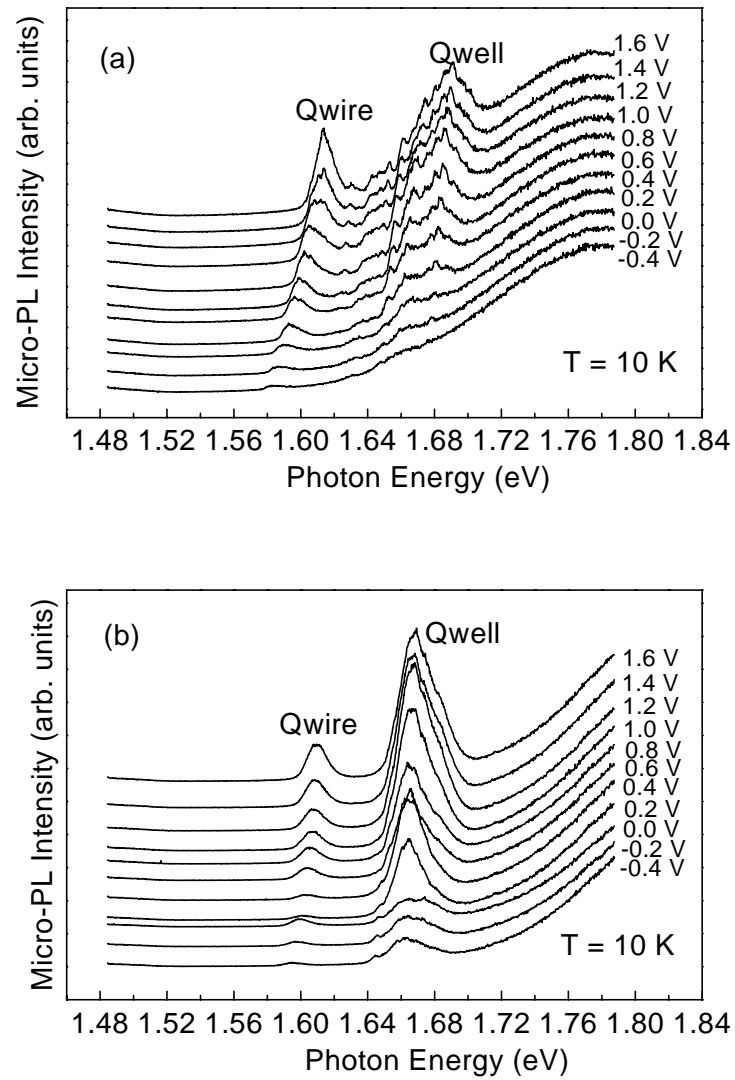


Figure 1.21: (a) μ -PL spectra taken at 10 K from the fast growing sidewall for sample pin2 when the externally applied bias changes from -0.4 to 1.6 V. (b) those for sample pin1.

show those of the quantum wire peak for the three samples. Here the energy position of the quantum well peak is obtained from the μ -PL measurements with the laser spot exciting on the flat part of the patterned stripe, i.e., not on a sidewall position. The $Al_{0.3}Ga_{0.7}As$ barrier between the two quantum wires is 10 nm thick for sample pin10, thus the two quantum wires and quantum wells are electronically weakly coupled for sample pin10, while they are strongly coupled for samples pin2 and pin1. It can be seen that the quantum well peak as well as the quantum wire peak do almost not change when increasing the applied electric field for the weakly coupled sample, while a significant redshift with increasing electric field is observed for the strongly coupled samples. For the weakly coupled sample, the wave function is localized in the two quantum wells or the two quantum wires, while for the strongly coupled sample, the wave function is more delocalized. Therefore, the behavior of the redshift when increasing the applied electric field for the strongly coupled sample is due to the strong electronic coupling compared to the weakly coupled sample. The variation of the wave function of the ground state for electrons in a strongly coupled quantum well with changing applied electric field is shown in Figure 1.23, which is obtained by solving the Schrödinger equation numerically. The potential is schematically drawn. The calculation indicates that the eigenenergy is decreased with increasing applied electric field. The redshift of the quantum wire peak is larger than that of the quantum well peak. For example, for sample pin2, when the applied electric field is changed from 0 to about 5×10^4 V/cm, the quantum wire peak is redshifted by 29 meV, but the quantum well peak is redshifted by only 10 meV. The reason is due to the larger layer thickness of the quantum wire compared to the quantum well.

Although we have observed a significant Stark effect for the strongly coupled sample, the observed effect is still difficult to directly connect to a quantum wire structure. In principle, it is possible to connect the Stark effect with a quantum wire structure by observing a blueshift of the PL peak [73]. Nevertheless, this is only true for very narrow quantum wire structures. When an external electric field E_{ext} is applied to a quantum well or quantum wire, the redshift can be observed if the following relation is satisfied:

$$E_b(0) - E_b(E_{ext}) < E_q(0) - E_q(E_{ext}), \quad (1.5)$$

where E_b and E_q denote the exciton binding energy and the quantized energies of electrons and holes without considering excitonic effect. For a quantum well structure, equation (1.5) is always satisfied. But for a very narrow

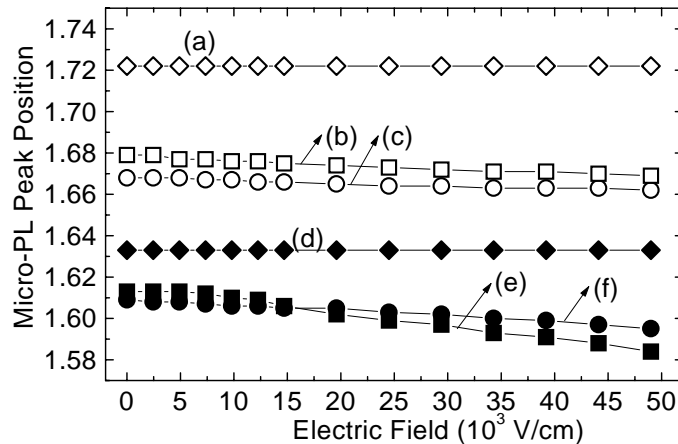


Figure 1.22: (a), (b) and (c) depict the energy position of the quantum well peaks versus the applied electric field for samples pin10, pin2, and pin1, respectively. (d), (e) and (f) show those of the quantum wire peaks for the three samples.

quantum wire structure, the exciton binding energy is very large when no electric field is applied, while, when an electric field is applied, the binding energy $E_b(E)$ is greatly decreased. The consequence is that, in a range of the applied electric field from zero to a certain value E_0 , the following relation is satisfied:

$$E_b(0) - E_b(E_{ext}) > E_q(0) - E_q(E_{ext}) \quad (0 < E_{ext} < E_0). \quad (1.6)$$

The above relation then results in a blueshift of the PL peak in quantum wire structures. Therefore, the possible blueshift is due to the enhanced binding energy of excitons in quantum wires. For a relatively wide quantum wire, equation 1.6 cannot be satisfied for any electric field E_{ext} and correspondingly, no blueshift is observed. In Ref. [73], when the lateral width of the V-groove is 35 nm, the blue shift is already completely quenched. The width of our sidewall quantum wire is about 50 nm [37]. This is probably the reason why we do not observe a blueshift when electric fields are applied to our sidewall quantum wires.

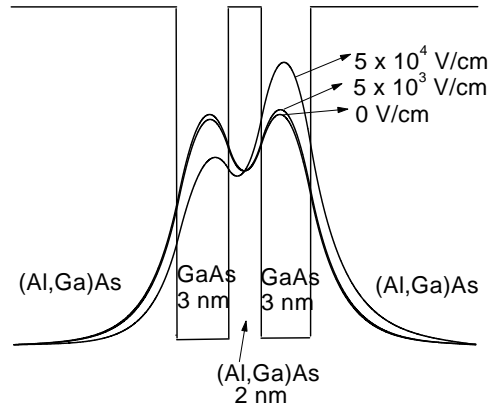


Figure 1.23: Variation of the electron wave function of the ground state in a strongly coupled quantum well when changing the applied electric field.

1.4 Atomic hydrogen effect and its application to the sidewall quantum wires

1.4.1 Introduction

Since the first report about the influence of surface-active species, called surfactants, in heteroepitaxial crystal growth [76], there has been a great interest in surfactants. During heteroepitaxy, if material A is grown on material B in a Frank-van der Merwe or Stranski-Krastanov mode, B will be grown on A in a Volmer-Weber mode, namely, if A wets B , B will not wet A [77]. The growth modes are discussed in detail in paragraph 2.1.1. Therefore, a fundamental difficulty occurs if an $A/B/A$ heterostructure is to be grown. This disadvantage can be diminished by introducing surfactants, which can reduce the surface free energy. Atomic hydrogen has been studied by different groups. Atomic hydrogen is found to be a surfactant in the heteroepitaxial growth of lattice mismatched systems [78, 79, 80, 81] on singular surfaces. The merit of introducing atomic hydrogen during growth is to promote layer-by-layer growth and to suppress island formation by delaying onset of islanding. For lattice matched homo- and hetero-epitaxy on singular GaAs(100) and InP(100), atomic hydrogen has been shown to result in a

flatter surface morphology [82, 83, 84]. On the other hand, atomic hydrogen induces step-bunching for GaAs grown on high index surfaces, like GaAs(331) and GaAs(311)A [85, 86]. Moreover, atomic hydrogen shows advantages in surface cleaning. Compared to the conventional annealing method, atomic hydrogen can greatly remove carbon and oxygen contaminants due to the formation of the hydrides of carbon and oxygen and other volatile oxides [87, 88, 80]. At the same time, the substrate temperature for atomic hydrogen cleaning is low (about 400°C), which is especially good for InP substrates due to their low congruent temperature [87].

High index surfaces play a promising and advantageous role in the fabrication of nanostructures by spontaneous pattern formation. It has been shown that a wire-like morphology can be obtained for the growth of (In,Ga)As on GaAs (311)A surface [89, 90]. The Stranski-Krastanov transformation for the growth of (In,Ga)As on GaAs (311)A substrates is delayed compared to that on conventional (100) substrates [91]. On the other hand, the spontaneous formation of surface corrugation combined with patterning the substrate offers a new pathway for synthesizing nanostructures [92]. However, studies about the atomic hydrogen effect in lattice mismatched heteroepitaxy on high index surfaces and its influence on the sidewall nanostructures is still lacking. We investigate the influence of atomic hydrogen in the growth of (In,Ga)As on GaAs(311)A and its application to the sidewall quantum wires.

1.4.2 Results and discussion

Semi-insulating GaAs (311)A substrates were patterned with mesa stripes of 75 μm width and 20 nm depth along the $[01\bar{1}]$ direction by photolithography and wet chemical etching. After cleaning with concentrated sulphuric acid and rinsing in de-ionized water, the sample was transferred into the MBE growth chamber. Although H can be used for surface cleaning, in order to compare between with and without H cases, the native oxide was desorbed at 580°C as is done by the conventional method. After a 50 nm GaAs buffer layer was grown at 610°C, the substrate was cooled down to 540°C for the growth of the other layers. A 3 nm (In,Ga)As layer was grown followed by 3-monolayer GaAs deposition without growth interruption to suppress the In segregation. Then, after a growth interruption of 10 seconds, a 50 nm GaAs layer was deposited. Finally, a 3 nm (In,Ga)As top layer was grown for the observation of the surface morphology by AFM. Here we study two samples. One is grown without H and the other one is grown by introducing H only

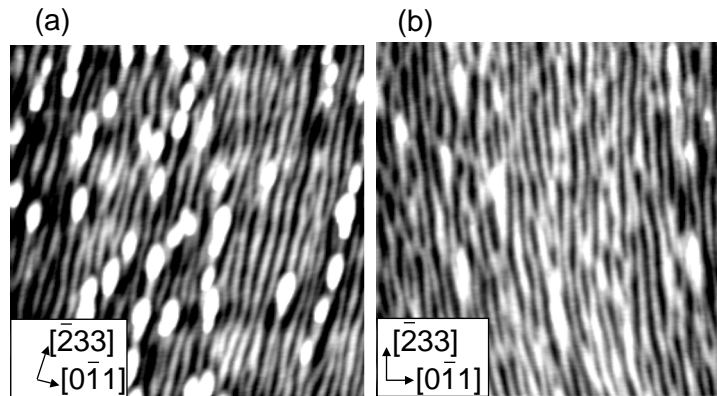


Figure 1.24: AFM top views of the (In,Ga)As/GaAs quantum well samples with In composition of 0.28 capped with 3 nm thick (In,Ga)As layer grown without (a) and with H (b), respectively, on GaAs(311)A. The scan field is $2\ \mu\text{m} \times 2\ \mu\text{m}$. The black-to-white height contrast in (a) and (b) is 5 nm.

during the deposition of the (In,Ga)As layer. H was produced by cracking molecular hydrogen through a hot tungsten filament heated to about 1800°C . During the growth with H, the background pressure in the MBE growth chamber is 3.6×10^6 Torr. The indium composition of the two samples is 0.28. The growth rate of GaAs is $0.235\ \mu\text{m}/\text{h}$ and the As to Ga flux ratio is about 5.

Figures 1.24(a) and (b) depict the AFM top views of the samples grown without and with H measured in air, respectively. Both images reveal arrays of laterally periodic wire-like islands oriented along the $[\bar{2}33]$ direction [90, 91]. The period of the lateral corrugations for the two samples amounts to about 70 nm and the width of the corrugation is about 50 nm, which is in agreement with the result of Ref.[89] by MOVPE. The periodicity of the lateral corrugation is related to the In composition [89]. For higher In composition, the lateral periodicity is decreased. For the without-H case [Figure 1.24(a)], some randomly distributed islands are superimposed on the laterally periodic corrugations, indicating that the Stranski-Krastanov transformation has occurred. On the other hand, for the with-H case, these superimposed islands are greatly reduced, implying that atomic hydrogen

suppresses island formation and delays the onset of islanding. It should be noted that such a corrugation can appear even for GaAs homoepitaxial layers grown on GaAs(311)A [91]. The reason can be found in the unique corrugation-like reconstruction of the GaAs (311)A surface [93, 94]. The corrugation of (In,Ga)As epilayers already relaxes the strain energy delaying the Stranski-Krastanov transformation. From this point of view, the corrugations on GaAs(311)A seems to behave like a “wetting” layer, although they are actually 3D islands.

For the Stranski-Krastanov growth mode, the thickness for the transition from two dimensional (2D) growth to three dimensional (3D) island formation will decrease with increasing the growth temperature [95]. Growth at high temperature is closer to equilibrium, indicating that the relaxation by islanding is energetically favored. From this point of view, we propose that H decreases the adatom migration length, thus resulting in a delay of the onset of islanding, as has been shown by our results. However, it should be noted that this is still a topic of great debate in the case of GaAs (100) surfaces [84, 96]. We also grew two (In,Ga)As single layer samples. For one of them, H was introduced during the deposition of (In,Ga)As. The 3 nm thick (In,Ga)As layer is grown after the deposition of the 50 nm thick GaAs buffer layer. The In composition of the two samples is 0.2. Figures 1.25(a) and (b) depict the AFM top views for the without- and with-H case, respectively. For both samples, no superimposed dot-like islands are observed. For this situation, the AFM images show no significant difference between the with-H and without-H samples indicating that the influence of atomic hydrogen on the growth of the wire-like corrugations is negligible. The long corrugations can be directly used to fabricate quantum wires.

Next we consider (In,Ga)As growth on patterned GaAs (311)A substrates. Figures 1.26(a) and (b) show the AFM images measured at the edge of the fast growing sidewall for the samples on patterned GaAs(311)A without and with H, respectively. For the without-H case, the superimposed islands appear at the top and the bottom of the mesa, but the edge of the mesa within about 1 μm range is completely free of islands and only the spontaneous corrugation can be seen. Two possibilities might explain the fact that no islands form on the edge of the mesa. One is that In adatoms migrate away from the edge of the mesa. The other is that the convex shape of the fast growing sidewall can partially relax strain and, thus, the relaxation by islanding is not favored at the edge of the fast growing sidewall. Because the former seems not to result in a fast growing sidewall, we tend to favor the latter

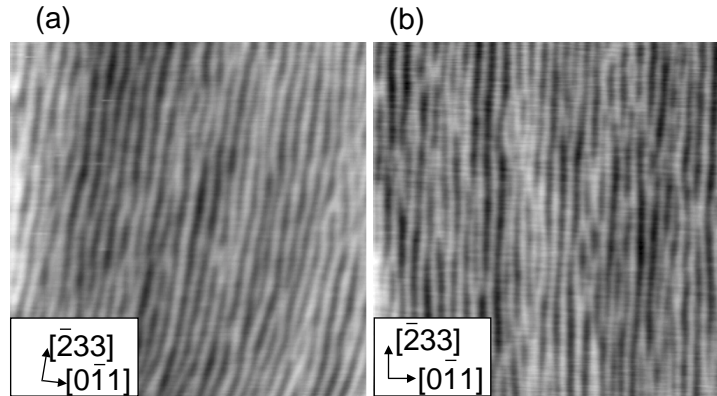


Figure 1.25: AFM top views of the single-layer (In,Ga)As samples with In composition of 0.2 grown without (a) and with H (b), respectively, on GaAs(311)A. The scan field is $2\ \mu\text{m} \times 2\ \mu\text{m}$. The black-to-white height contrast in (a) and (b) is 4 nm.

explanation. For the with-H case, the islands at the top and the bottom of the mesa have been greatly suppressed.

Figure 1.27 shows the μ -PL spectra measured at 12 K with the laser spot exciting at the fast growing sidewall for the with-H (top of Figure 1.27) and without-H (bottom of Figure 1.27) samples. The diameter of the laser spot was controlled to be about $2\ \mu\text{m}$ by a confocal imaging system. The peak located at the lower-energy side is attributed to the nanostructures from the edge of the mesa and that at the higher energy side is related to the nanostructures from the top and the bottom of the mesa. The undulation peaks appearing on the envelopes of the two peaks are due to the structural nonuniformity. The μ -PL peak separation between the two peaks are 23 meV for the with-H sample and 13 meV for the without-H sample, respectively, while both spectra reveal that the peak positions of the nanostructures at the edge of the mesa are the same for the two samples. This can be understood by examining the Figures 1.26(a) and (b). Because H strongly suppresses the island formation, the average layer thickness of (In,Ga)As at the top and the bottom of the mesa of the without-H sample is smaller than that of the with-H sample. This result in a blueshift of the peak at the higher energy side for the with-H case compared to the without-H case. For the potential

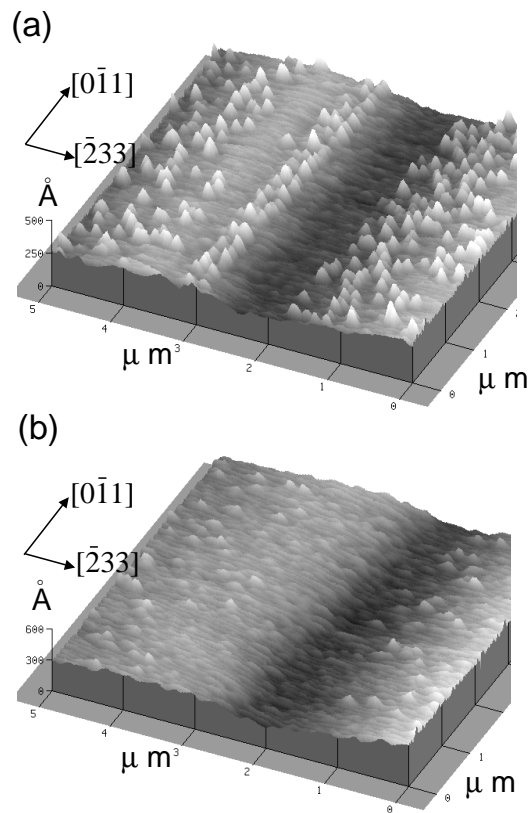


Figure 1.26: AFM images of (In,Ga)As samples grown on patterned GaAs(311)A without H (a) and with H (b), measured around the fastgrowing sidewall.

device applications of the sidewall nanostructures at room temperature, it is essential to make the peak separation larger. We thus conclude that the utilization of H is beneficial to the sidewall nanostructures.

In conclusion, atomic hydrogen plays a surfactant role in the growth of (In,Ga)As on GaAs(311)A. Atomic hydrogen suppresses island formation and delays the relaxation by islanding. We propose that atomic hydrogen decreases the adatom migration length in lattice mismatched systems. The utilization of atomic hydrogen enlarges the PL peak separation between the nanostructures located at the edge of the mesa and those at the top and the bottom of the mesa on patterned GaAs (311)A substrate.

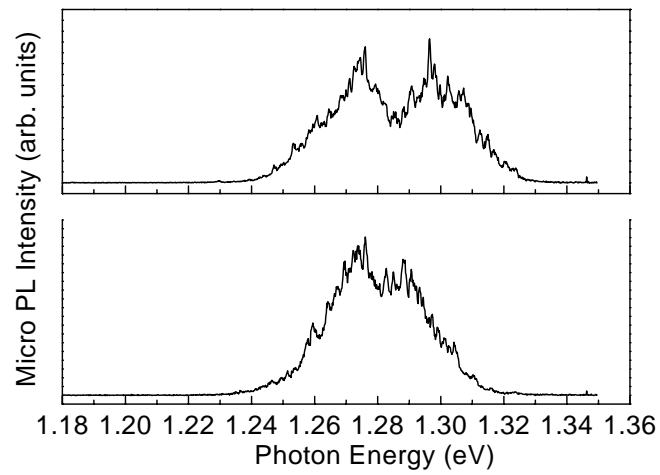


Figure 1.27: μ -PL spectra measured at 12 K with the laser spot exciting at the fast growing sidewall for the with-H (top) and the without-H (bottom) samples, respectively. The peak located at the lower energy side is attributed to the nanostructures at the edge of the mesa. The peak at the higher energy side is attributed to the nanostructures at the top and bottom of the mesa.

Chapter 2

Self-organized quantum wires on GaAs(100)

2.1 Shape transition

2.1.1 Growth mode

The study of epitaxial growth mechanisms has a long history and a large variety of material systems have been investigated. Three growth modes are usually distinguished in heteroepitaxy, called Frank-van der Merwe, Volmer-Weber, and Stranski-Krastanov, describing layer-by-layer, islanding, and layer-by-layer plus islanding [77, 97]. Theoretically, neglecting strain energy, the growth mode is determined by the surface free energy of the epitaxial film, the surface free energy of the substrate, and the interface energy. For very thin layers, if material A is deposited on material B , only two kinds of surface morphologies are possible [98]. As schematically shown in Figures 2.1(a) and (b), one case is that material A uniformly covers material B and the other case is that material A forms 3D islands on material B . Supposing that η per cent of the surface is covered by 3D islands for the latter case, the total energy per unit area corresponding to the cases (a) and (b) then is, respectively, $E_a = \gamma_A + \gamma_i$ and $E_b = \eta\gamma_A + \eta\gamma_i + (1 - \eta)\gamma_B$, where γ_A , γ_B , and γ_i denote the surface free energies per unit area of the interface between material A and the vacuum, of the interface between material B and the vacuum, and of the interface between material A and B , respectively. The growth mode is determined by the relationship of E_a and E_b which is equivalent to that of $\gamma_i + \gamma_A$ and γ_B . Hence, if $\gamma_i + \gamma_A > \gamma_B$, the growth of

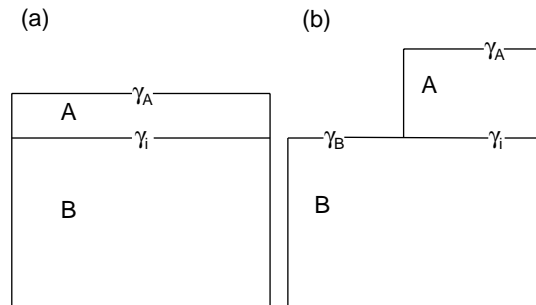


Figure 2.1: Two alternative epitaxial growth modes neglecting strain. (a): The epitaxial layer uniformly covers the surface of substrate; (b): the epitaxial layer forms 3D islands on the surface of the substrate (A. Zangwill, [98]).

3D islands is favored, i.e., Volmer-Weber growth mode occurs. On the other hand, if $\gamma_i + \gamma_A < \gamma_B$, the growth mode is Frank-van der Merwe. For strained systems, the lattice misfit introduces a strain energy which increases linearly with the overlayer thickness. This misfit induced strain energy does not allow growth of more than several monolayers and can be relaxed by formation of 3D islands. Therefore, Stranski-Krastanov growth occurs for systems with small interface energy and large lattice mismatch with the formation of a 2D “wetting” layer [99, 100] in the initial stage of growth, which is absent in the Volmer-Weber growth mode. Figure 2.2 schematically shows the topological evolution of the three distinct epitaxial growth modes [97].

Experimentally, the growth mode can be distinguished by the favored surface morphology after deposition of one monolayer of material [101]. If the morphology shows 3D clusters, it is a Volmer-Weber system. If the morphology shows a uniform layer, it is either a Frank-van der Merwe or a Stranski-Krastanov system. The latter can be distinguished by the occurrence of 3D islands at a coverage above one monolayer.

2.1.2 Surface morphology of (In,Ga)As single layers

The three growth modes discussed before are found experimentally in the epitaxy of semiconductors and metals. For semiconductors, the heteroepitaxy

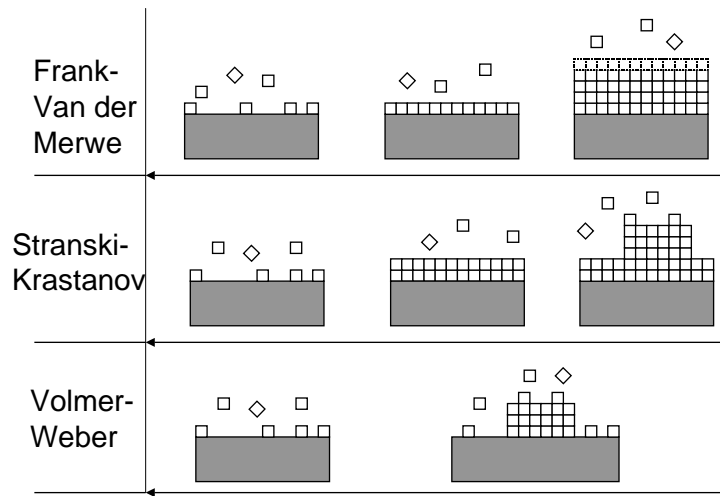


Figure 2.2: Schematic views of the three topologically distinct epitaxial growth modes (Kern, Le Lay and Metois, [97]).

of Ge on Si and (In,Ga)As on GaAs follows the Stranski-Krastanov growth mode which has been studied intensively. Traditionally, the creation of dislocations is regarded as a prerequisite for the transformation from 2D layers to 3D islands for the Stranski-Krastanov growth mode [102]. However, uniformly strained 2D layers are generally unstable or metastable [103, 104, 105] and can also relax by undergoing a morphological change of the surface profile [106, 107]. For thin films, this results in the formation of dislocation-free islands, the “coherent” Stranski-Krastanov growth mode. After the first experimental report of dislocation-free islands in the growth of Ge on Si [106], this coherent Stranski-Krastanov mode was also reported for highly strained (In,Ga)As on GaAs(100) [107]. The importance of the study of the relaxation process [108, 109, 110, 111, 112, 113, 114] lies in two aspects: one is to understand the growth mechanisms and accordingly to get optimum experimental conditions for crystal growth. The other is that these coherent 3D islands can be utilized to fabricate quantum dots, most prominent InAs quantum dots on GaAs, which is currently studied intensively [21, 22, 23, 24, 25].

Quantum dots are 3D islands of a low-band-gap semiconductor enclosed by a wide-band-gap semiconductor matrix. The size of the dots should be small enough to show quantum confinement, on the other hand, they should be large enough that at least one bound state levels exists. If elongated

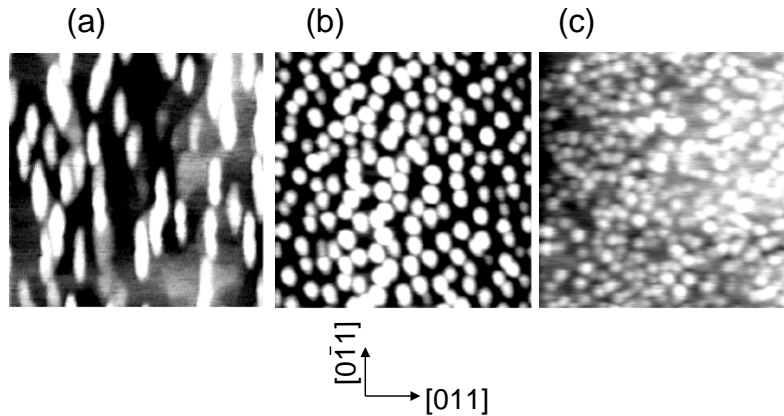


Figure 2.3: AFM top views of the 1.8-nm thick (In,Ga)As single layer samples with the In composition of 0.35 grown at 540 (a), 475 (b), and 430°C (c) on GaAs(100). The scan field of (a), (b) and (c) is $1\ \mu\text{m} \times 1\ \mu\text{m}$, $0.5\ \mu\text{m} \times 0.5\ \mu\text{m}$, and $0.5\ \mu\text{m} \times 0.5\ \mu\text{m}$, respectively. The black-to-white height contrast is 3 nm for all images.

islands can be obtained, they may be used as a template for quantum wire formation. Therefore, it is of importance to study the influence of the growth conditions on the shape and size of 3D islands [115, 116, 22, 117, 118].

A series of (In,Ga)As single layer samples with different In compositions were grown on GaAs(100) at different growth temperatures. In order to investigate the shape transition (this will be discussed in detail in paragraph 2.1.4), the thickness of the (In,Ga)As single layers is kept constant at 1.8 nm. The samples were grown by conventional solid source MBE. After the native oxide was desorbed at 580°C, a 110 nm thick GaAs buffer layer was grown before the substrate was cooled down to the temperature for the (In,Ga)As single layer deposition. The growth rate of GaAs was $0.235\ \mu\text{m}/\text{h}$ and the As to Ga flux ratio was about 5 with the As_4 background pressure during growth of about 3.8×10^{-8} Torr. The AFM measurements were performed ex situ in contact mode in air by using a $75\ \mu\text{m}$ scanner.

Figures 2.3(a), (b) and (c) display the AFM top views of the samples with In composition of 0.35 (In composition determined by XRD and RHEED

oscillations discussed later) grown at the substrate temperatures of 540, 475 and 430°C, respectively. In-situ monitoring of RHEED intensity oscillations shows that the initial growth is layer-by-layer which is already suppressed after 1.8 nm (In,Ga)As deposition (after about 20 seconds) showing that the growth follows Stranski-Krastanov mode under these growth conditions. The three AFM images in Figure 2.3 reveal the surface morphologies of 3D islands indicating that Stranski-Krastanov growth transformation has occurred. For the sample grown at 540°C [Figure 2.3(a)], the islands are slightly elongated (for most islands, the length to width ratio is about 6). At relatively low growth temperatures [Figures 2.3(b) and (c)], more symmetrically shaped islands are revealed. The average diameters of the islands in Figures 2.3(b) and (c) are about 28 and 18 nm, respectively, demonstrating that, for a fixed In composition and layer thickness, the sizes of the islands can be varied by changing the growth temperature. From AFM measurements, it is clear that different morphologies are obtained at different growth temperature. Since the growth temperature directly governs the surface diffusion length, it is thus concluded that the formation of dislocation-free islands is a kinetically limited process [116]. On the other hand, Figures 2.4(a) and (b) display AFM images of samples grown at 540°C with the In composition of 0.25 and 0.45, respectively. Comparison of Figures 2.4(a) and (b) with Figures 2.3(a), (b) and (c) reveals that, with increasing In composition, elongated islands tend to transform into more round-shaped islands suggesting that the islands shape is also controlled by adjusting the In composition. We believe that elongated island formation is possible even for layers with higher In composition if the growth temperature and layer thickness are adjusted appropriately. This shape transition will be discussed in detail in 2.1.4.

The growth of (In,Ga)As on GaAs follows the Stranski-Krastanov mode. From AFM, it is in fact surprising that we do not observe a pure 2D growth mode (also refer to the RHEED studies discussed later) even when the (In,Ga)As layer is only 1.8-nm thick and the In composition is 0.35. However, this layer-by-layer growth is also a kinetically limited process [95]. For a constant lattice mismatch, the thickness for transition from the 2D layer to coherent 3D island formation increases with decreasing growth temperature, i.e., decreasing surface diffusion length. At near-equilibrium conditions, i.e., at high growth temperature and small growth rate, where the diffusion length is large, the transition layer thickness is very thin [95]. Therefore, for the samples with dot- and wire-like morphologies, the wetting layer is expected to be very thin, as indicated by the TEM images in paragraph 2.3. It should

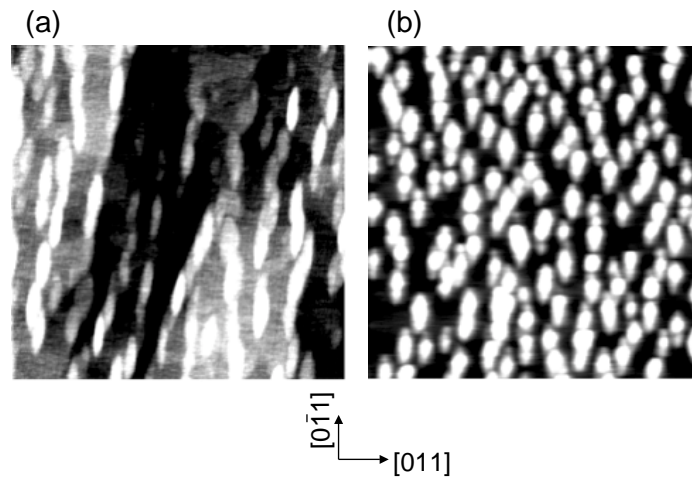


Figure 2.4: AFM top views of the 1.8-nm thick (In,Ga)As single layer samples with the In composition of 0.28 (a) and 0.45 (b) grown at 540°C on GaAs(100). The scan field of (a) and (b) is $1\ \mu\text{m} \times 1\ \mu\text{m}$. The black-to-white height contrast is 3 nm for the two images.

be emphasized that the formation of the Stranski-Krastanov growth mode is based on an equilibrium concept implying that at near equilibrium conditions the growth results in islands on a 2D wetting layer. At actual growth conditions which are far from equilibrium, the growth mode for Stranski-Krastanov systems at equilibrium can even be of Volmer-Weber type [119]. It is still not clear whether Stranski-Krastanov growth is a kinetically limited process. At actual growth conditions which are far from equilibrium, the layer-by-layer growth can be greatly increased, which is confirmed by our results. Correspondingly, the growth of a 1.8-nm-thick (In,Ga)As single layer with In composition of 0.35 grown at 330°C is found to be 2D, as shown in Figure 2.5. Our results demonstrate that the shape and size of 3D (In,Ga)As islands are kinetically controlled, i.e., strongly dependent on the growth temperature. Therefore, to control the shape and the size of the 3D islands, great attention must be paid to the growth kinetics which is determined by the substrate temperature and growth rate.

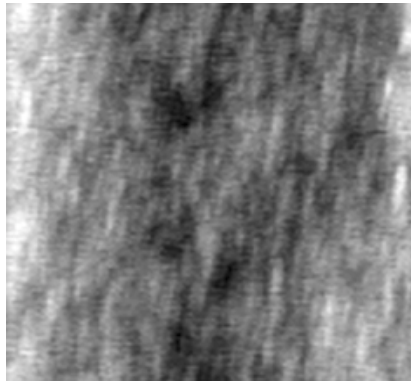


Figure 2.5: AFM top view of the 1.8-nm thick (In,Ga)As single layer sample with the In composition of 0.35 grown at 330°C (c) on GaAs(100). The scan field is $5\ \mu\text{m} \times 5\ \mu\text{m}$. The black-to-white height contrast is 2 nm.

2.1.3 RHEED characterization

Reflection high energy electron diffraction (RHEED) is the most powerful technique to monitor in situ the layer growth by MBE [120, 1]. In RHEED, electrons of a few keV to ~ 100 keV are directed towards the surface of the sample in an extremely small angles of incidence (0.5° to 2.5°). Therefore, electrons penetrate only the first to second topmost atomic layers of a smooth surface making RHEED very sensitive to surface information. RHEED is an established technique [121]. In the 1950s and 1960s, RHEED had been employed to determine the growth mode of epitaxial metal films [122]. However, its truly wide use stems from the appearance of MBE because one constraint for the employment of RHEED is that the vacuum must be high enough to avoid the scattering of electrons by the background gas molecules. Therefore, RHEED cannot be used in the normal pressure chemical vapor deposition such as metalorganic vapor phase epitaxy. Moreover, the extreme small incidence and exit angles of the electron beam facilitate the in situ observation of RHEED in MBE. In MBE, RHEED has now become a routinely used and very important tool for growth studies.

The diffraction of electrons in crystals can be understood by the classic theory developed by Bragg and Laue. When strong diffraction occurs, the condition, $\mathbf{K}_s - \mathbf{K}_i = \mathbf{G}$, must be satisfied, where \mathbf{K}_s , \mathbf{K}_i , and \mathbf{G} denote the scattered wavevector, the incident wave vector, and a reciprocal lattice

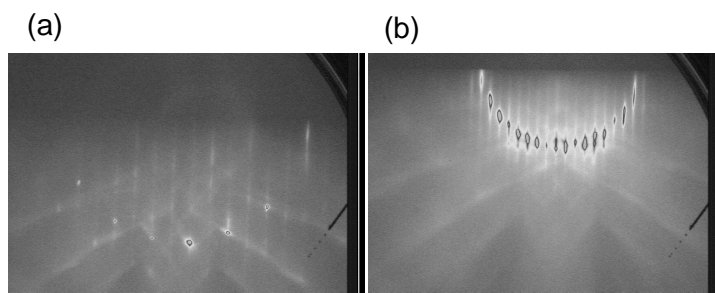


Figure 2.6: RHEED patterns of the GaAs(100) surface showing (2×4) reconstruction. (a) and (b) are viewed along the $[011]$ and $[0\bar{1}1]$ azimuths, respectively.

vector, respectively. This is the Laue condition which is equivalent to Bragg law. However, in the case of RHEED, where only a few crystal planes parallel to the surface contribute to the diffraction, the set of reciprocal lattice points perpendicular to the surface is replaced by a set of continuous reciprocal lattice "rods". This approximation can be thought of as relaxation of the Laue condition from the three dimensional case to two dimensional case [121]. Thus, the RHEED pattern reflects the corresponding surface structure in reciprocal space projected along the observation direction.

A very useful characteristic feature of RHEED for growth studies is the periodic intensity oscillation of the RHEED pattern. Intensity oscillations of RHEED patterns were first discovered in 1981 [123] and can provide a fairly precise indication of the growth rate in MBE. A simple explanation of RHEED oscillations relies on the assumption that the growth is layer-by-layer via 2D island nucleation and coalescence [122]. When atoms are impinging on the surface of the sample, they nucleate and develop as small 2D islands. These 2D islands then grow and coalesce via the Frank van der Merwe growth mode. The reflectivity maxima correspond to scattering from atomically smooth surfaces where the growth in the layer-by-layer mode is either at the initial point or at the end point of one monolayer deposition, while the reflectivity minima correspond to scattering from maximally disordered

surfaces where the growth is at the point of half a monolayer deposition. Therefore, one period of the intensity oscillations corresponds to one monolayer growth. Care should, however, be taken for the treatment of RHEED oscillations because in principle the observed intensity integrates the contributions from the elastically and the diffusely scattered electrons [122]. For a fixed observation azimuth, the “phase” [124] of the oscillations strongly depends on the incident angles, which can be qualitatively explained in terms of the relative contributions of elastic scattering and diffuse scattering to the measured intensity [122]. If intensity oscillations are recorded from locations of the RHEED pattern which correspond to a mixture of elastic and diffuse scattering, the oscillation periodicity may be maintained, but usually the oscillation period is smaller compared to that where elastic or diffuse scattering dominates [122]. This fact may partially be the reason why usually the growth rate obtained from RHEED is larger than that obtained from x-ray diffraction measurement. In practice, even for homoepitaxy such as GaAs grown on GaAs, no persistent oscillations are maintained. This damping of the oscillations can be interpreted by a step density model. When oscillations occur, the step density changes periodically. When the oscillations are completely damped, the step density reaches a constant value when the arriving adatoms migrate to the step edges of existing islands rather than to nucleate new 2D islands on the terraces. Under this condition, growth occurs by a regular step propagation.

During the deposition of the buffer layer, the RHEED pattern shows a (2×4) surface reconstruction [125] as depicted in Figures 2.6(a) and (b). Figure 2.7 shows the RHEED intensity oscillations measured at the specular spot giving the growth rate of GaAs of $0.2487 \mu\text{m/h}$, which is in agreement with the value of $0.235 \mu\text{m/h}$ obtained from x-ray diffraction. Figure 2.8(a), (b), and (c) depict the intensity oscillations of the background during the deposition of (In,Ga)As for the samples with In composition of 0.35 grown at the substrate temperatures of 540, 475, and 430°C , respectively, i.e., corresponding to the samples with surface morphologies shown in Figures 2.3(a), (b) and (c), respectively. The intensity oscillations show that the initial deposition stage of (In,Ga)As is layer-by-layer and, after about 4 monolayers deposition, the 3D island formation is initiated which suppresses the intensity oscillations, indicating that Stranski-Krastanov growth occurs. For the layer by layer growth, when growth is initiated, the diffuse scattering is increased [122]. The intensity recorded from a background spot is dominated by diffuse scattering while that from a specular spot is dominated by elastic

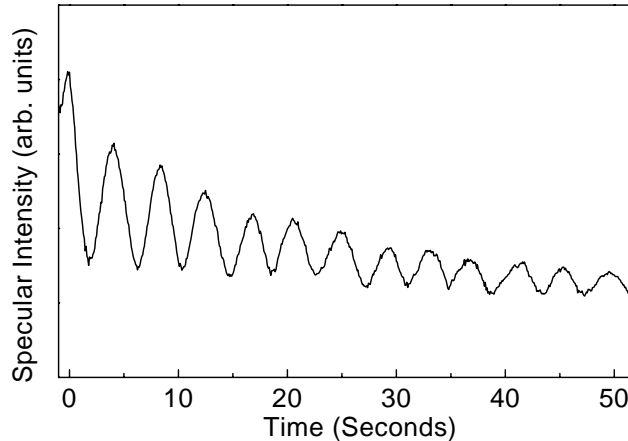


Figure 2.7: RHEED intensity oscillations for GaAs growth on GaAs(100). The observation is in the $[011]$ azimuth at the specular spot. The surface reconstruction is (2×4) .

scattering. Therefore, when growth is initiated, the intensity from a specular spot is decreased while that from a background spot is increased [as shown in Figures 2.8(a), (b) and (c)], i.e., the “phase” is different [122]. When growth transforms from the layer-by-layer to 3D islanding mode, in our case, the background intensity was found to increase continuously and then becomes stable. However, the different background intensities for the three samples in the final growth stage as shown in the inset of Figure 2.8 may indicate that the (In,Ga)As single layers grown at different substrate temperatures have a different surface morphology which results in different diffuse scattering. In Ref. [126], when growth is in 3D islanding mode, the intensity recorded from a specular spot is also found to increase continuously. The reason is probably due to the continuously increased diffuse scattering. Figure 2.9 and Figure 2.10 are the corresponding RHEED patterns recorded after deposition of 1.8 nm (In,Ga)As at the growth temperatures of 540 and 475 °, respectively. For the (In,Ga)As layer grown at 475°C, the spotty RHEED patterns [Figure 2.10(a) and (b)] looks similar when observed along the $[011]$ and the $[0\bar{1}1]$ azimuths, while, for the (In,Ga)As layer grown at 540°C, the RHEED pattern is spotty when observed along the $[011]$ azimuth [Figure 2.9(b)], but is streaky when observed along the $[0\bar{1}1]$ azimuth [Figure 2.9(a)]. The spotty RHEED patterns indicate that 3D islands exist on the surface. Although

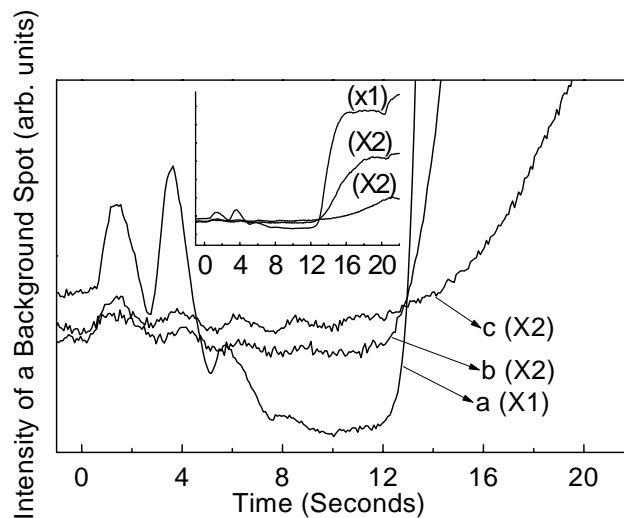


Figure 2.8: RHEED intensity oscillations during the growth of $In_{0.35}Ga_{0.65}As$ on GaAs(100) at substrate temperatures of 540 (a), 475 (b) and 430°C (c). The observation is along the [011] azimuth from a window set at the background. The inset shows the same curves with low magnification.

there are several origins accounting for streaky RHEED patterns, considering the information given by AFM (Figure 2.3), we attribute the streaky RHEED pattern observed along the [011] azimuth to the presence of elongated islands along the $[0\bar{1}1]$ direction. For the 1.8-nm thick (In,Ga)As layer grown at 430°C, the RHEED pattern looks similar to Figure 2.10 and is not shown here. The In compositions obtained for different growth temperatures from Figure 2.8(a), (b) and (c) are almost the same, indicating that In desorption can be neglected when the substrate temperature is below 540°C. The In composition determined from the RHEED oscillations, however, is 0.38, which is somewhat larger than the value of 0.35 obtained from x-ray diffraction. The reason could be that overshooting of In flux in the initial growth stage occurs when the shutter is opened.

Figures 2.11(a), (b) and (c) depict the intensity oscillations of the background during the deposition of (In,Ga)As for samples with In composition of 0.35, 0.28 and 0.20, respectively, grown at the same substrate temperature of 540°C. The In source temperatures corresponding to Figures 2.11(a), (b) and (c) are the same as those of samples SL25, SL17 and SL13, respectively. The latter three samples will be discussed in the following part. It should be

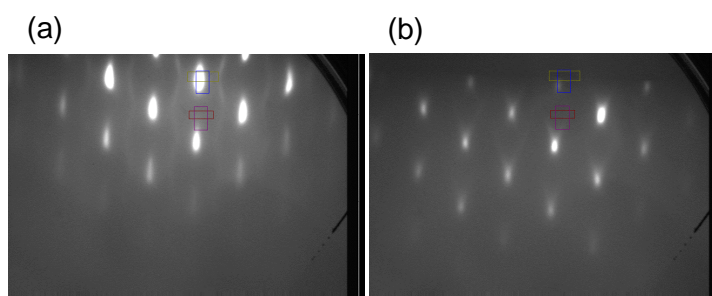
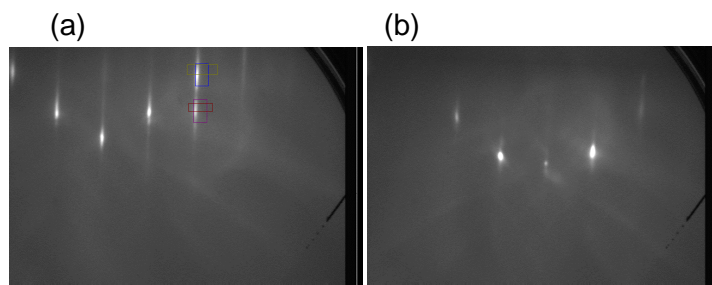


Figure 2.9: RHEED patterns after 1.8-nm thick $In_{0.35}Ga_{0.65}As$ is deposited at $540^{\circ}C$. (a) and (b) are observed along the $[0\bar{1}1]$ and $[011]$ directions, respectively.

Figure 2.10: RHEED patterns after 1.8-nm thick $In_{0.35}Ga_{0.65}As$ is deposited at $475^{\circ}C$. (a) and (b) are observed along the $[0\bar{1}1]$ and $[011]$ directions, respectively.

noticed that the background intensity for the samples with In composition of 0.35 and 0.28 increases continuously when 3D island growth starts to occur. On the other hand, such an increase of the background intensity is not

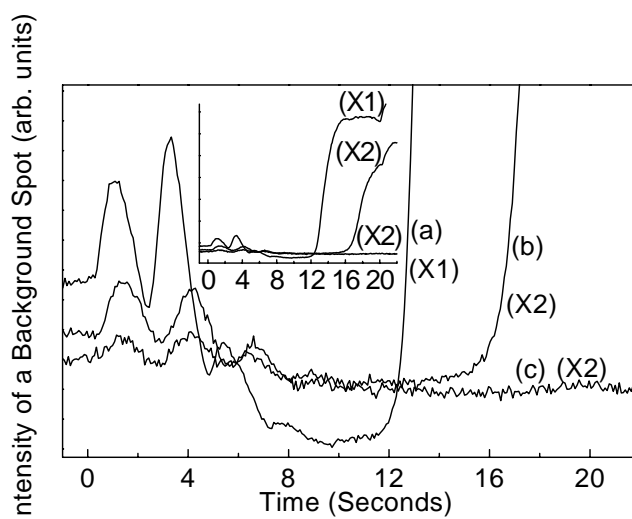


Figure 2.11: RHEED intensity oscillations during the growth of (In,Ga)As with In composition of 0.35 (a), 0.28 (b), and 0.20 (c) on GaAs(100) at the substrate temperature of 540°C. The observation is along the [011] azimuth at a background window. The inset shows the same curves with low magnification.

found for the sample with In composition of 0.20. This implies that, after 1.8 nm (about 22 seconds) deposition of (In,Ga)As, 3D island formation still does not occur, which is confirmed through the observations of the surface morphology by AFM images shown in the subsequent part (Figure 2.19). Figure 2.12 shows the RHEED pattern after 1.8 nm deposition of (In,Ga)As for the sample with In composition of 0.35 grown at 330°. The streaky RHEED patterns, rather than spotty ones (like in Figures 2.9 and 2.10) is indicative of 2D growth, which is again supported by the AFM observations (Figure 2.5).

2.1.4 Shape transition

Theory

Tersoff and Tromp [127] have predicted that elongated island formation, as an approach to the fabrication of quantum wires, is a universal property in strained systems. Subsequent theoretical work [128, 129, 130] led to the same conclusion. Their prediction has been confirmed for CoSi₂ on Si(100) [131].

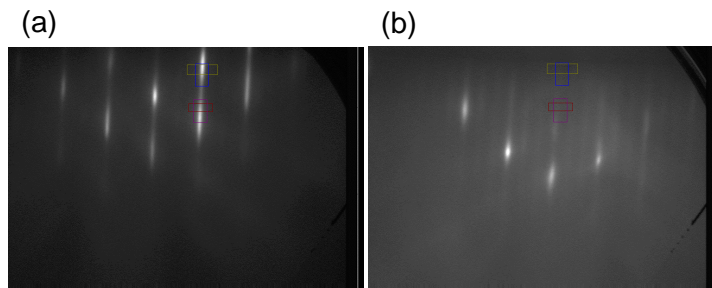


Figure 2.12: RHEED patterns after 1.8-nm thick $\text{In}_{0.35}\text{Ga}_{0.65}\text{As}$ is deposited at 330°C on $\text{GaAs}(100)$. (a) and (b) are observed along the $[0\bar{1}1]$ and $[011]$ azimuth directions, respectively.

However, although some elongated island formation has been reported, such as InAs on $\text{InP}(100)$ [27] and $(\text{In,Ga})\text{As}$ on $\text{GaAs}(100)$ [28, 132], to the best of our knowledge, an experimental demonstration of the shape transition from dot-like to elongated islands in some important strained systems, such as $(\text{In,Ga})\text{As}$ on $\text{GaAs}(100)$, still lacks. As shown in 2.1.2, our solution to realize this shape transition in $(\text{In,Ga})\text{As}/\text{GaAs}(100)$ is by changing the growth temperature. The shape transition, as shown in Figures 2.3 (a), (b) and (c), can be explained by Tersoff and Tromp's theoretical work [127] described below.

For simplicity, Ref. [127] assumes a rectangularly shaped island with contact angle θ , width s , length t , and height h , in the x , y , z directions, as schematically shown in Figure 2.13. The island energy can be written as

$$E = E_s + E_r, \quad (2.1)$$

where E_s and E_r denote the extra surface and interface energy, and the strain energy, respectively. Neglecting the edge energy, the extra surface energy is

$$E_s = st(\gamma_i + \gamma_t - \gamma_s) + 2(s + t)[h\gamma_e \csc \theta - h \cot \theta(\gamma_t + \gamma_s - \gamma_i)/2], \quad (2.2)$$

where γ_s , γ_t , γ_e are the surface energy (per unit area) of the substrate and of the island's top and edge facets, respectively, and γ_i is the interface energy between the island and the substrate. For Stranski-Krastanov growth, the appropriate reference for the substrate is not the bare substrate surface, but the surface of the wetting layer. Thus, with $\gamma_t = \gamma_s$ and $\gamma_i = 0$, equation (2.2) becomes

$$E_s = 2(s + t)h\Gamma, \quad (2.3)$$

where $\Gamma = \gamma_e \csc \theta - \gamma_s \cot \theta$. For very thin films, where $s \gg h$ and $t \gg h$, the strain energy can be written as [127]

$$E_r = -2ch^2[s \ln(\frac{t}{\phi h}) + t \ln(\frac{s}{\phi h})], \quad (2.4)$$

where $c = \sigma_b^2(1 - \nu)/2\pi\mu$, ν and μ are the Poisson ratio and the shear modulus of the substrate, and $\phi = e^{-3/2} \cot \theta$ for convenience. σ_b is the xx or yy component of the bulk stress of the epilayer uniformly strained to fit the substrate along the x and y directions. From equations (2.3) and (2.4), the island energy per unit volume can be written as

$$\frac{E}{V} = 2\Gamma(\frac{1}{s} + \frac{1}{t}) - 2ch[\frac{1}{s} \ln(\frac{s}{\phi h}) + \frac{1}{t} \ln(\frac{t}{\phi h})], \quad (2.5)$$

where $V = hst$ denotes the volume of the island.

The island growth not only depends on energetics, but also on kinetics. Ref. [127] considers the growth kinetics by assuming that as atoms arriving on the surface diffuse towards the islands, where they tend to stick to the beveled edge rather than to diffuse to the top facet of the island. This growth kinetics results in a roughly constant height h of the island because the island height h grows slowly compared to the island width s and length t . Thus, the growth kinetics can be taken into account by minimizing the energy with respect to s and t , keeping h constant. θ is also fixed for simplicity. There are two distinct cases of the theory, which should be discussed separately.

(a), The energy per unit volume $\frac{E}{V}$ is minimized with respect to the island width s and length t by optimizing the volume of the island instead of fixing it. The resulting minimum $\frac{E}{V}$ corresponds to the island size where $s = t = a_0 = e\phi h e^{\frac{E}{ch}}$. This corresponds to the case where the adatom diffusion length is large enough to pass materials between islands such that isolated islands reach their optimized shape where the energy per unit volume

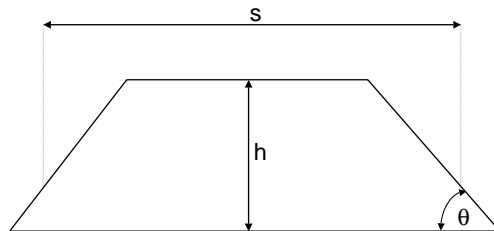


Figure 2.13: Schematic drawing of the elongated shape of the island assumed in the theory by Tersoff and Tromp, [127]. s , h and θ denote width, height and contact angle, respectively.

is minimum. Namely, this case applies to very slow growth rates close to the thermodynamic limit.

The physical origin of this case is that small islands have a large surface energy per unit volume due to the large surface-to-volume ratio, and thus are unfavorable. Large islands have a small surface energy per unit volume, but cannot relax their elastic energy efficiently. The best trade-off between surface energy and strain energy is thus realized at intermediate size.

(b), The energy per unit volume $\frac{E}{V}$ is minimized with respect to the island shape, i.e., t/s , by fixing the volume of the island. This corresponds to the case where the adatom diffusion length is small enough that the diffusion between islands can be neglected and deposited material will attach to the nearest island. The island then will grow without bounds, but for a fixed island volume, the island shape is determined through the restriction relationship of equation (2.5). This case applies to rapid growth and is probably more suitable for typical growth conditions, where the islands are too far apart to coalesce or ripen. For the compactness of description, we use a “reduced energy equation” by defining $\varepsilon = \frac{E}{2Vch}$ and $s = \sigma a_0$, $t = \tau a_0$. Then equation (2.5) becomes

$$a_0\varepsilon = -\frac{\sigma + \tau}{\sigma\tau} - \frac{1}{\tau} \ln \tau - \frac{1}{\sigma} \ln \sigma. \quad (2.6)$$

Set $\lambda = \sigma\tau \implies \tau = \frac{\lambda}{\sigma}$, and fix the volume $V = hst$. Because h is kept

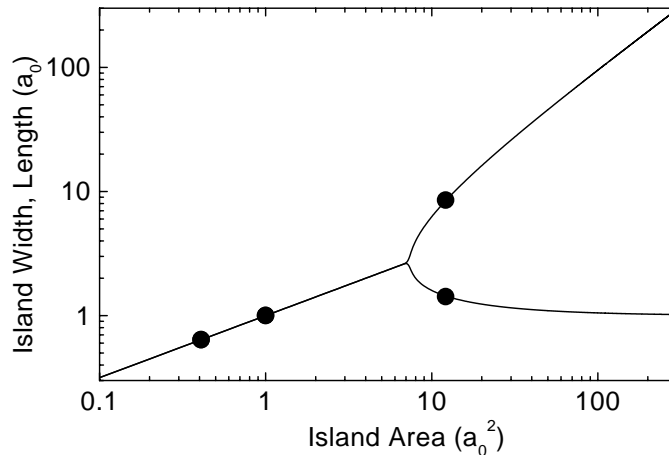


Figure 2.14: The solid line shows the width and length of island vs the area of island recalculated numerically according to the theory by Tersoff and Tromp, Ref. [127]. The solid circles are the experimental points corresponding to (a), (b) and (c) in Figure 2.3, showing the shape transition from square to elongated islands. The unit of the width and the length of the island is $a_0 = 281.4\text{\AA}$. The unit of the area of the island is $a_0^2 = 79185.96 \text{\AA}^2$. The island becomes elongated when the area of the island is larger than $ea_0 \times ea_0$. The scales are logarithmic.

constant, fixing V is equivalent to fixing λ and equation (2.6) becomes

$$a_0\varepsilon = -\frac{\sigma}{\lambda} - \frac{1}{\sigma} - \frac{\sigma}{\lambda} \ln \frac{\lambda}{\sigma} - \frac{1}{\sigma} \ln \sigma. \quad (2.7)$$

Minimizing ε with respect to σ gives

$$\frac{\partial \varepsilon}{\partial \sigma} = \frac{1}{\sigma^2} \ln \sigma - \frac{1}{\lambda} \ln \frac{\lambda}{\sigma} = 0. \quad (2.8)$$

Equation (2.8) can only be solved numerically. The solid line in Figure 2.14 shows the result of the numerical calculation of the island width σ and length $\tau = \lambda/\sigma$ with respect to the island area λ^2 . Please note that in Figure 2.14, the unit of the island width and length is a_0 and the unit of the island area is a_0^2 . It can be seen that the shape of the island remains squared, i.e., $s = t$, when the island area is smaller than $e^2 a_0^2$. However, the island becomes elongated when its area increases beyond $e^2 a_0^2$. As indicated in Figure 2.14, the

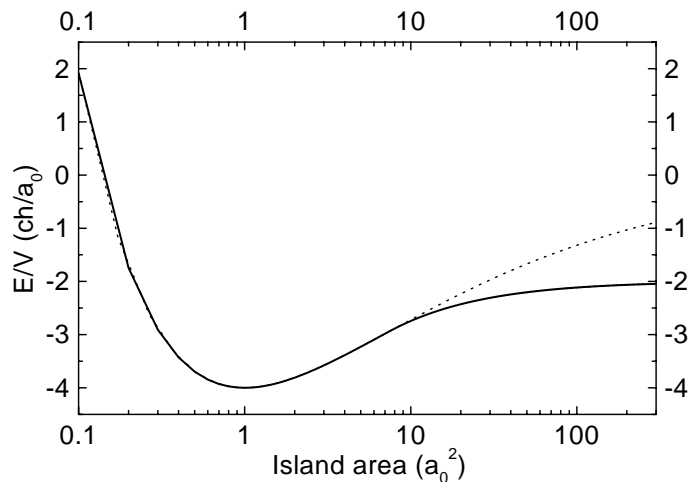


Figure 2.15: The solid line shows energy per unit volume of the island, in units of $\frac{ch}{a_0}$, vs the area of the island recalculated numerically according to the theory by Tersoff and Tromp, Ref. [127], by assuming fixed h and θ . The dotted line shows the energy if the shape of the island remained square.

island width asymptotically equals a_0 for large island areas. This conclusion can be directly deduced from equation (2.8). From equation (2.8), it follows $\ln \sigma = \frac{\sigma^2}{\lambda + \sigma^2} \ln \lambda$, therefore, when $\lambda \rightarrow \infty$, we get $\sigma \rightarrow 1 \implies s = \sigma a_0 \rightarrow a_0$.

When the island becomes large enough, if the island is still square-shaped, the elastic relaxation becomes negligible as the island grows. The island can then achieve the optimal trade-off between surface energy and strain energy by transforming into a rectangular shape. As shown by the calculated solid line in Figure 2.14, the island can grow arbitrarily large, but the island width is almost kept constant, implying that the uniformity of the islands could be very good. This offers a very promising mechanism for self-organization of quantum wires. The solid line in Figure 2.15 depicts the energy per unit volume, in units of ch/a_0 , as a function of the island area calculated by assuming the island shape as shown in Figure 2.14, while the dotted line shows the energy per unit volume by assuming a square shape of the island. It can be seen that, when the island area is larger than $e^2 a_0^2$, the symmetrically-shaped island has a larger energy and is therefore not favored.

Results and discussion

The three AFM images shown in Figure 2.3 in fact demonstrate the existence of the shape transition from isotropic islands to elongated islands. For a quantitative comparison between the theory and the experiments, we use the island height $h = 1.8$ nm and the contact angle $\theta = 9.3^\circ$, which are obtained from AFM line-scans. As mentioned above, the appropriate reference for the substrate in this case is the (In,Ga)As wetting layer. The In composition corresponding to the three AFM images is 0.35. The elastic moduli of (In,Ga)As are $C_{11} = 10.592 \times 10^{11}$ dyn/cm², and $C_{12} = 5.042 \times 10^{11}$ dyn/cm² [55]. Poisson ratio ν , shear modulus μ , and bulk stress σ_b are related to C_{11} and C_{12} , and can be directly determined by the relationships:

$$\nu = \frac{C_{11}}{C_{11} + C_{12}}, \quad (2.9)$$

$$\mu = \frac{C_{11}^2 + C_{11}C_{12} - 2C_{12}^2}{2(C_{11} + C_{12})}, \quad (2.10)$$

and

$$\sigma_b = (C_{11} + C_{12} - \frac{2C_{12}^2}{C_{11}})\varepsilon^{\parallel}. \quad (2.11)$$

Here ε^{\parallel} is the lattice mismatch between the (In,Ga)As wetting layer and the GaAs substrate. We use $\gamma_e = 57$ meV/Å² and $\gamma_s = 57$ meV/Å², which are obtained by linearly interpolating between the surface free energy data of GaAs and InAs [133, 134].

Finally, we get $\Gamma = 4.63$ meV/Å² and $a_0 = 281.4$ Å. The solid circles in Figure 2.14 correspond to the experimental points determined from Figure 2.3. A good agreement between the theory and our experimental data can be obtained for $a_0 = 280$ Å, implying that the theoretical considerations in the model describes the principal features of island growth and are thus sufficient.

Several important features should be considered when comparing the model with the experimental data. First, the key point to test the model is to keep the island height h relatively constant. Our approach to realize this shape transition is to deposit a constant number of monolayers of material at different growth temperatures. In principle, 3D coherent strained islands can lower their strain energy by increasing their height. However, if the increase in height of a 3D island is kinetically limited, the island may

grow only laterally keeping its height constant. Then shape transition occurs. This is the key point for understanding the observed shape transition. From the AFM images [Figure 2.3(a), (b), and (c)], the average height of the islands corresponding to the samples grown at different temperatures is relatively constant. Second, the surface free energy data for (In,Ga)As for arbitrary In composition are not well documented in the literature. Therefore, the data for the calculation are obtained by linearly interpolating between the data of GaAs and InAs according to the In composition. The used data of surface free energy for GaAs(100) and InAs(100) are 65 and 44 meV/Å², respectively [133, 134]. The value of γ_e used in the calculation is equal to γ_s . This may be justified by the small contact angle between the two planes of only about 9.3° by considering the Wulff plot [98, 135], which is a polar plot of the surface free energy with respect to the surface orientation. Finally, the model in Ref. [127] assumes that the islands are well separated and island-island interaction is not taken into account. Tersoff, however, pointed out that the correction by considering island-island interaction is of relatively little importance, even when the surface is half covered [136].

2.2 Self-organized quantum wires

2.2.1 Fabrication of self-organized quantum wires

Self-organized correlation

In section 2.1.4, we have demonstrated the shape transition from squared to elongated islands for the growth of single layer (In,Ga)As on GaAs (100) substrates and discussed the growth mechanism. In the following, fabrication of quantum wires based on these elongated islands will be pursued. The uniformity of these elongated islands by the growth of (In,Ga)As single layer can be rather good, however, it is not yet satisfactory for most practical applications. For potential applications in optoelectronic devices, it is crucial to fabricate uniform and long wires. Fabrication of quantum wires and quantum dots with regular in-plane spatial distribution and enhanced size uniformity has always been a challenge for crystal growth technology. Thanks to the nature of strained island formation, vertical self-organization, i.e., vertically correlated arrangements of 3D islands, may be a key solution to this problem [137]. Due to the strain field induced by the buried 3D islands on the surface, subsequent island deposition will be favored at those substrate locations

where the strain field induces a local minimum of lattice mismatch [138, 139]. Therefore, new islands tend to nucleate on the top of the buried strained islands and a vertical correlation is then generated. Therefore, the growth of a superlattice is a good scheme to generate such a vertical self-organization. In fact, this vertical correlation has been reported for InAs dots on GaAs(100) and $\text{Si}_x\text{Ge}_{1-x}$ dots on Si(100). Xie et al [138] studied the vertical correlation of InAs islands separated by GaAs spacer layers in dependence of the spacer layer thickness and the lateral separation of the islands. A phenomenological model was proposed to treat the interacting island-induced strain field, which brings about a preferential migration of In adatoms, as the driving force for vertical self-organization. They pointed out that a high pairing probability, i.e., an obvious vertical alignment, is related to the thickness of the spacer layer. Obvious vertical correlation occurs only when the spacer layer is smaller than a critical value. Tersoff et al [139] gave a simple generic model treating island formation as a process in which nucleation only occurs at the surface locations where the misfit is at a local minimum, and nowhere else. The simulated island positions show not only a vertical ordering but also, astonishingly, a more uniform island size distribution and spacing with increasing growth periods.

Uniformity enhancement by superlattice growth

In order to improve the uniformity of elongated islands, we grew two 15-period (In,Ga)As/GaAs superlattice samples with In composition of 0.35 and 0.28, respectively. For both samples, a 120 nm thick GaAs buffer layer was grown at 580°C before the substrate was cooled down to 540°C within 60 seconds for the superlattice growth. After the (In,Ga)As was deposited, 3-monolayer GaAs were deposited without growth interruption to suppress indium segregation and then, after 10 second growth interruption, GaAs growth was started. The layer thicknesses of (In,Ga)As and GaAs are 1.8 and 19 nm, respectively. Finally, to observe the influence of the superlattice growth on the (In,Ga)As island formation by AFM, a 1.8 nm thick (In,Ga)As top layer was deposited for both samples. The growth rate of GaAs and the As to Ga flux ratio were the same as for the single layer growth.

Figure 2.16(a) and (b) depict the AFM top views of the two 15-period samples with In composition of 0.35 and 0.28, denoted as SLC35 and SLC28, respectively. Compared to the single layer samples [Figures 2.3(a) and 2.4(a)], the uniformity of the (In,Ga)As islands for both samples is greatly

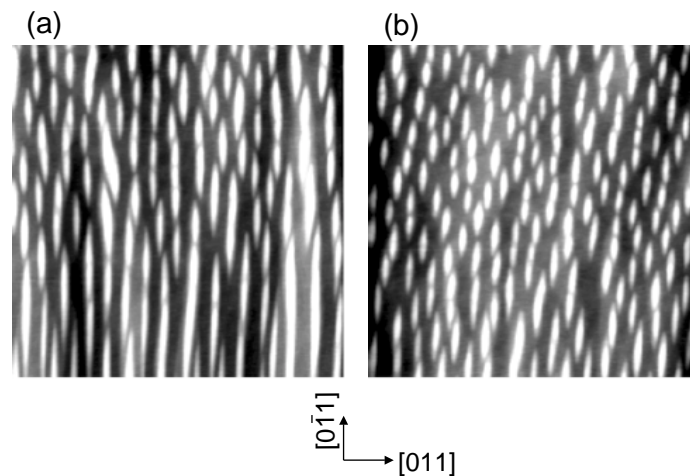


Figure 2.16: AFM top views of the 15-period (In,Ga)As/GaAs superlattice samples continuously grown at 540°C on GaAs(100) with the In composition of 0.35 (a) and 0.28 (c). The scan field of (a) and (b) is $2\ \mu\text{m} \times 2\ \mu\text{m}$. The black-to-white height contrast is 8 nm for all images.

improved. For the sample with In composition of 0.35 [Figure 2.16(a)], the islands become more elongated in some regions, while Figure 2.16(b) (the sample with In composition of 0.28) does not reveal further island elongation compared to the single layer sample with the same In composition. The question now arises if it is possible to further improve the uniformity of the elongated (In,Ga)As islands and make them even more elongated. For this purpose, a second series of samples was grown and the details of the sample preparation are described below.

The series of samples are comprised of three 15-period (In,Ga)As/GaAs superlattice structures grown at different indium source temperatures, denoted as SL25, SL17, and SL13, respectively. The indium source temperature of samples SL25 and SL17 were the same as that of samples SLC35 and SLC28, respectively. The thicknesses of the (In,Ga)As and GaAs layers in the superlattice structures for the three samples were again 1.8 and 19 nm, respectively, for the purpose of comparison with the samples mentioned above. The GaAs buffer layer of 120 nm was grown at 580°C and then the substrate was cooled down to 540°C within 60 seconds. After the growth of each (In,Ga)As layer at 540°C , three monolayers GaAs were

deposited without growth interruption to suppress indium segregation before the substrate was heated up to 580°C for GaAs growth. Finally, a 1.8 nm (In,Ga)As top layer was grown for the observation of the surface morphology by AFM. The difference of the growth conditions between this series of samples and the series of SLC35 and SLC28 is that the heating of the substrate from 540°C to 580°C occurs for the preceding ones after the growth of each (In,Ga)As layer covered by three monolayers GaAs. Some features of the superlattice samples are displayed in the table below.

sample number	SLC35	SLC28	SL25	SL17	SL13
In composition	0.35	0.28	0.25	0.17	0.13
period	15	15	15	15	15
(In,Ga)As layer thickness	1.8 nm	1.8 nm	1.8 nm	1.8 nm	1.8 nm
GaAs layer thickness	19 nm	19 nm	19 nm	19 nm	19 nm
growth temperature for (In,Ga)As	540°C	540°C	540°C	540°C	540°C
growth temperature for GaAs	540°C	540°C	580°C	580°C	580°C

Figure 2.17(a) and (b) display the AFM top views of samples SL25 and SL17, respectively. For comparison, Figure 2.17(c) and (d) show the AFM top views of the single layer samples which are grown at 540°C at the same indium source temperatures as that for samples SL25 and SL17, respectively. Compared to the two single layer samples [Figures 2.17(c) and (d)] and also the superlattice samples continuously grown at 540°C [Figures 2.16(a) and (b)], the AFM images manifest that the uniformity of the (In,Ga)As islands for samples SL25 and SL17 has been greatly improved and the islands become much longer (most islands for samples SL25 and SL17 are longer than 3 μm). The process resulting in the improvement of the island uniformity is not yet well understood. It might be possible that, during the heating of the substrate from 540 to 580°, Ostwald ripening [101] occurs. But the ripening process here seems to result in a more ordered arrangement of the islands rather than a random one, which might be due to and proves the anisotropic distribution of the strain field. It can be seen from the AFM images that the spacing between these cigar-like islands along the [011] direction for the single

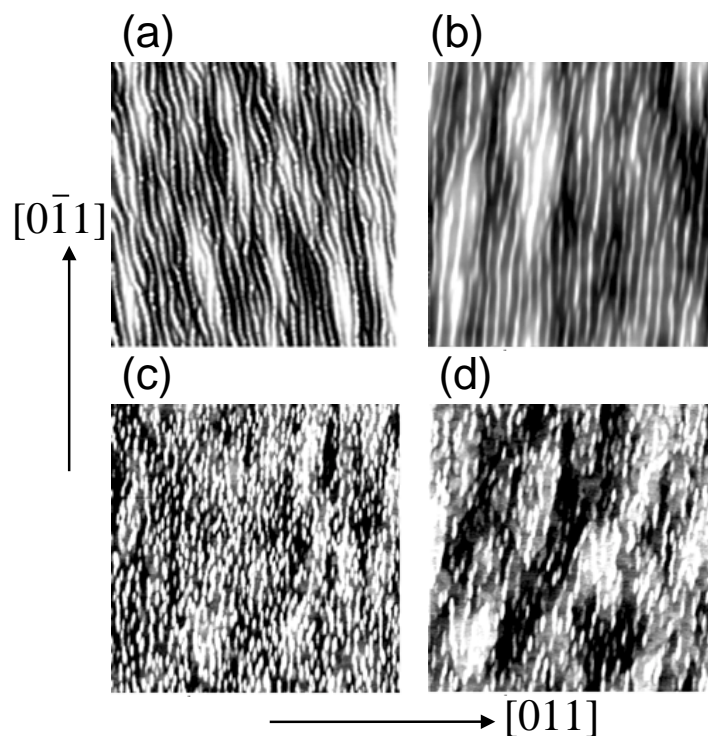


Figure 2.17: (a) and (b) are the AFM images of samples SL25 and SL17 (refer to the table on page 69), respectively; (c) and (d) are those of the 1.8-nm thick (In,Ga)As single layer samples grown at 540°C on GaAs(100) with the same In source temperatures as SL25 and SL17, respectively. The black-to-white height contrast for (a), (b), (c) and (d) is 15, 10, 3, and 3 nm, respectively. The scan field for all images is $5\ \mu\text{m} \times 5\ \mu\text{m}$.

layer samples is the same as the lateral period of the corresponding superlattice samples (SLC35 and SLC28, and SL25 and SL17, respectively). This fact indicates that the islands predominantly align and thus connect each other along the $[0\bar{1}1]$ direction during the ripening. Therefore, the islands become longer and more laterally ordered. The islands in Figure 2.17(a) are comprised of dots arranged very closely along the wire direction, which can be easily seen from the AFM image with enhanced scale depicted in Figure 2.18(a), while those in Figure 2.17(b) show a more uniform contrast as can be seen from Figure 2.18(b). The closely arranged dots along the $[0\bar{1}1]$ direction may be treated as a template for the fabrication of strongly coupled

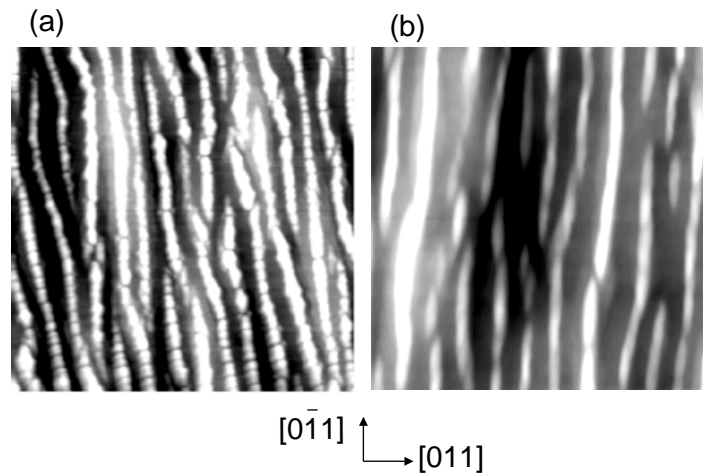


Figure 2.18: (a) Magnified image of Figure 2.17(a). (b) Magnified image of Figure 2.17(b). The scan field for (a) and (b) is $2\ \mu\text{m} \times 2\ \mu\text{m}$. The black-to-white height contrast is 15 and 10 nm for (a) and (b), respectively.

quantum dots. The root mean square (rms) roughness of the samples SL25 and SL17 over several μm amounts to 4 and 1.9 nm, respectively. The AFM peak to valley height differences of samples SL25 and SL17 are 18 and 8 nm, respectively. In contrast, the surface morphology of sample SL13 with the smallest In composition is smooth, as shown in Figure 2.19. Within several μm , the RMS roughness is only 0.2 nm and the AFM peak-to-valley height difference is 0.8 nm. This finding indicates that, for a fixed layer thickness and growth temperature, the wire-like morphology is obtained when the In composition surpasses a critical value, and then changes to a dot-like morphology for large In composition. Because AFM only shows the topmost layer, in the following we employ double crystal x-ray diffractometry (XRD) and transmission electron microscopy (TEM) to present detailed information on the layered structure [140].

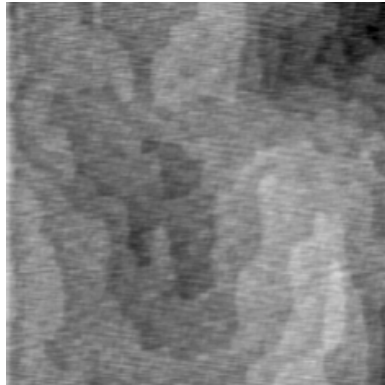


Figure 2.19: AFM top view of sample SL13 (refer to the table on page 69). The scan field is $3\ \mu\text{m} \times 3\ \mu\text{m}$. The black-to-white height contrast is 2 nm.

2.2.2 X-ray diffraction characterization

Double crystal x-ray diffraction

The technique of x-ray diffraction (XRD) is one of the most widely used tools for structural characterization. The advantage of this technique lies in the fact that it is nondestructive and does not require any particular process of sample preparation. XRD can provide a very accurate determination of the strain state, the chemical composition, and the individual layer thickness of semiconductor heterostructures and superlattices. Double crystal XRD is by far the most common XRD technique utilized to characterize the structure of epitaxial layers and superlattices [141]. Figure 2.20 schematically shows the experimental setup of a double crystal x-ray diffractometer employing the $+-$ nondispersive Bragg geometry [142]. The x-rays from the source tube first pass through the “first crystal” which is usually a single- or multi-scattering dislocation-free Ge crystal serving as a monochromator and collimator designed to diffract only $\text{CuK}\alpha_1$ radiation. In order to minimize the angular divergence of the x-rays striking on the sample, the surface of the first crystal is usually miscut with respect to the diffraction plane to achieve an optimal choice of the asymmetry factor. In our case, a rotating anode of $\text{Cu K}\alpha_1$ radiation is used. A four-crystal Bartels-type configuration using the Ge (220) reflection with the crystal surface miscut by 15° serves as the monochromator and collimator. The monochromatic x-rays strike on the

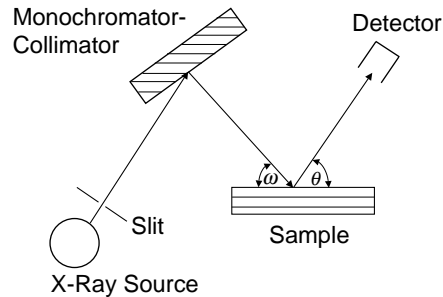


Figure 2.20: Schematic drawing of the set-up of the double crystal x-ray diffractometer (L. Tapfer, [142]).

sample, the so-called “second crystal”, to diffract and finally are recorded by a NaI scintillation detector. The angle between the incident beam and the surface of the sample is usually denoted as ω , and that between the diffracted beam and the surface of the sample as θ . The sample and the detector rotations are driven by computer-controlled stepping motors.

There are two commonly used scanning modes for double crystal x-ray diffraction. One is called ω scan, i.e., rocking curve mode, and the other is called $\omega - 2\theta$ scan. The ω scan is realized by rocking the sample and fixing the detector at the $2\theta_B$ position, where θ_B denotes the kinematical Bragg angle. The $\omega - 2\theta$ scan is achieved by following the orientation of the sample and the detector such that $\Delta\omega = \Delta\theta$ is maintained, where $\Delta\omega$ and $\Delta\theta$ denote the angle separations of the incident x-ray beam and the detector, respectively, from the position where the condition of Bragg diffraction is satisfied. If there is no slit mounted in front of the detector, namely, an open detector is used, these two scanning modes are equivalent. However, the rocking curve scan mode has only a limited angular detection range of about several degrees, while the angular detection range for $\omega - 2\theta$ scan mode, in principle, can be arbitrarily large. The conventional double crystal x-ray diffractometer uses an open detector and therefore integrates the scattering from the sample over all angles within its aperture [143, 144, 145]. Therefore, it mixes the information about orientation distribution and lattice spacing distribution. This disadvantage can be diminished by performing ω scans and/or $\omega - 2\theta$ scans

with a very small slit mounted in front of the detector. This disadvantage can be almost completely overcome by using an analysis crystal called analyzer in front of the detector instead of a small slit [143]. Such a system is called triple-axis diffractometer. The triple-axis diffractometer has the same geometry as a double crystal XRD, and can be regarded as a double crystal XRD with a detector probe of almost zero width achieved by a certain diffraction of the analyzer. ω scan and $\omega - 2\theta$ scan are different and complementary for triple axis diffraction. Therefore, triple axis diffraction can distinguish between contributions to the intensity from mosaic spread (by ω scan) and from lattice spacing distribution (by $\omega - 2\theta$ scan) [146]. Reciprocal space mappings are obtained with triple axis diffraction by performing a series of independent $\omega - 2\theta$ scans where ω is varied independently, and then transforming the series of $\{\Delta\omega - \Delta\theta\}$ data into reciprocal space coordinates through the equations below [141]:

$$|\mathbf{k}| = (k_{\perp}^2 + k_{\parallel}^2)^{\frac{1}{2}} = \frac{4\pi \sin(\theta_B + \Delta\theta)}{\lambda}, \quad (2.12)$$

and

$$k_{\parallel}/k_{\perp} = \tan(\alpha - \Delta\theta + \Delta\omega). \quad (2.13)$$

Here, α is the angle between the diffraction planes and the surface of the sample. Reciprocal space mapping can give more complete and detailed information about the sample structure and the strain state, however, the measurement is much more time-consuming and not convenient. In spite of the disadvantage, it is more accurate and clear to understand crystal diffraction by using the reciprocal space (k -space) description. Therefore, the basic rationale of how to transform XRD data into reciprocal space coordinates is described here. In the following part, the diffraction of strained epitaxial layers and that of quantum wires arrays are described by using the reciprocal space description.

Theory

The fundamental understanding of x-ray diffraction in a crystal is given by the famous Bragg law:

$$n\lambda = 2d \sin \theta_B, \quad (2.14)$$

Where n is the diffraction order, λ is the wavelength of the incident x-rays, d is the spacing between the diffracting planes, and θ_B is the angle between the

incident x-rays and the diffracting planes, usually called kinematical Bragg angle. Although the theory of x-ray diffraction was established quite long time ago and is regarded as a “ripe” theory, a relatively deep and complete understanding of the diffraction behavior can hardly be qualified by the mere use of Bragg’s law. Some books, for example, those written by Kittel [147] and Zachariassen [148], provide a complete and clear description about the theory of x-ray diffraction. The dynamical theory of x-ray diffraction takes into account the effect of multiple scattering and thus is very accurate for arbitrary layer thickness. The dynamical theory can be derived from the Takagi-Taupin differential equation and can only be expressed as a recurrence formalism [142]. Its concrete application to multi-layers and superlattice structures can be found in scientific journal papers, for example, those by Vardanyan and Manoukyan et al. [149, 150], and by Bartels et al [151]. The kinematical approximation is valid when the total thickness of the heteroepitaxial layers is smaller than the extinction length l_{ex} , which is expressed as

$$l_{ex} = \frac{\lambda \sqrt{(\gamma_0 |\gamma_h|)}}{\pi \sqrt{|X_h X_{\bar{h}}|}}. \quad (2.15)$$

Here, $\gamma_0 = \cos[\frac{\pi}{2} - (\alpha - \theta_B)]$ and $\gamma_h = \cos[\frac{\pi}{2} - (\alpha + \theta_B)]$ are the direction cosines of the incident and diffracted waves, respectively, with respect to the inward normal of the sample surface, and X_h and $X_{\bar{h}}$ are the h th and \bar{h} th Fourier coefficients of the polarizability, respectively, which are proportional to the structural factor of the corresponding diffraction. The typical value of the extinction length for III-V compound semiconductors is 0.5-1.5 μm for $\text{CuK}\alpha_1$ radiation [142]. The application of the kinematical theory to the diffraction of strained superlattice structures has been developed by Mathieson [152], Speriosu [153], and Speriosu and Vreeland [154]. A semi-kinematical theory, which can be regarded as in between the dynamical and kinematical theories, but is easier to mathematically deal with, has been established by Tapfer and Ploog [155]. Here we will only describe the related theories which are applied to this work rather than give a complete and detailed description of the dynamical and kinematical theories.

Chemical composition and layer thickness of superlattice structure

The feature of x-ray diffraction for a single strained layer can be expressed very clearly in reciprocal space. The lattice point in reciprocal space, $\mathbf{G}_{\mathbf{hkl}}$,

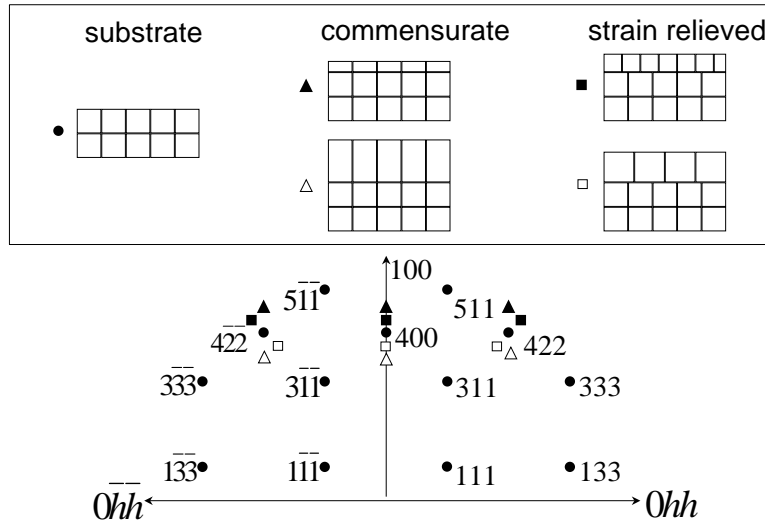


Figure 2.21: Illustration of the changes in reciprocal space positions in the $\{110\}$ plane for unstrained, compressive, and tensile commensurately strained layers and strain-relieved layers for the 400 and 422 positions (Picraux et al, [141]).

is expressed as

$$\mathbf{G} = h\mathbf{A} + k\mathbf{B} + l\mathbf{C}. \quad (2.16)$$

Here, \mathbf{A} , \mathbf{B} , and \mathbf{C} are the basic vectors in reciprocal space and are defined as

$$\mathbf{A} = 2\pi \frac{\mathbf{b} \times \mathbf{c}}{\mathbf{a} \cdot (\mathbf{b} \times \mathbf{c})} \quad \mathbf{B} = 2\pi \frac{\mathbf{c} \times \mathbf{a}}{\mathbf{a} \cdot (\mathbf{b} \times \mathbf{c})} \quad \mathbf{C} = 2\pi \frac{\mathbf{a} \times \mathbf{b}}{\mathbf{a} \cdot (\mathbf{b} \times \mathbf{c})}. \quad (2.17)$$

\mathbf{a} , \mathbf{b} , and \mathbf{c} are the basic vectors in real space. The choice of the conventional cell instead of the primitive cell is more convenient for the cubic diamond and zinc-blend lattices. When a strained single crystalline layer is grown on top of the substrate crystal, the strain will distort the lattice constants of the epitaxial layer and therefore results in changes of reciprocal space points of the epitaxial layer through the definitions of equations (2.16) and (2.17). The concrete position of the epitaxial layer relative to that of the substrate in reciprocal space depends on the strain state. A detailed treatment of the problem is given in Ref. [141], which is outlined in the following. Figure 2.21 schematically depicts the position changes in reciprocal

space of the $\{011\}$ plane for unstrained (substrate), compressive, and tensile commensurately strained and strain-relieved layers for the 400 and 422 positions [141]. For pseudomorphic growth, where the epitaxial layers have the same in-plane lattice constant as the substrate, the filled and open triangles show the compressive- and tensile-distorted lattice positions. It can be seen that for the pseudomorphic growth, the positions of both the symmetric and asymmetric diffraction, for example, the (400) and (422) diffractions, are vertically aligned relative to that of the substrate along the growth direction. On the other hand, for strain-relieved lattices (depicted as filled and open squares), the vertical alignment relative to the substrate along the growth direction breaks down. Therefore, to determine the vertical and in-plane strain, at least two diffractions, a symmetric one and an asymmetric one, are required.

For a strained single layer, the peak separation $\Delta\omega$ for the epitaxial layer with respect to the substrate can be expressed by the relation

$$-\Delta\omega = \tan\theta_B \frac{\Delta d}{d_{hkl}} + \Delta\alpha, \quad (2.18)$$

where the first term describes the contribution due to the change of the hkl plane spacing Δd , and the second term describes that due to the rotation of these planes. The two terms are related to the perpendicular and parallel strains by

$$\frac{\Delta d}{d} = \varepsilon_{epi}^\perp \cos^2\alpha + \varepsilon_{epi}^\parallel \sin^2\alpha, \quad (2.19)$$

and

$$\Delta\alpha = \pm(\varepsilon_{epi}^\perp - \varepsilon_{epi}^\parallel) \sin\alpha \cos\alpha, \quad (2.20)$$

and equation (2.18) then becomes

$$-\Delta\omega = (\varepsilon_{epi}^\perp \cos^2\alpha + \varepsilon_{epi}^\parallel \sin^2\alpha) \tan\theta_B \pm (\varepsilon_{epi}^\perp - \varepsilon_{epi}^\parallel) \sin\alpha \cos\alpha. \quad (2.21)$$

Here, the + and - signs correspond to the cases of incident angles of $\theta_B - \alpha$ and $\theta_B + \alpha$, respectively. ε_\perp and ε_\parallel are the perpendicular and parallel strains with respect to the substrate, defined as

$$\varepsilon_{epi}^\perp = \frac{a_{epi}^\perp - a_{sub}}{a_{sub}}, \quad \varepsilon_{epi}^\parallel = \frac{a_{epi}^\parallel - a_{sub}}{a_{sub}}. \quad (2.22)$$

Here a_{epi}^\perp , a_{epi}^\parallel , and a_{sub} denote the vertical and parallel lattice constants of the epitaxial layer, and that of the substrate. If a symmetric and an asymmetric

diffractions are measured, the perpendicular and parallel strain relative to the substrate can be determined by equation(2.21), and then the vertical and parallel lattice constants are determined by equation (2.22). It should be noted that ε_{epi}^\perp and $\varepsilon_{epi}^\parallel$ are the strains with respect to the substrate, called “x-ray strains” [141], while the “true” perpendicular and in-plane strains are defined as

$$e_\perp = \frac{a_{epi}^\perp - a_{epi}^0}{a_{epi}^0} \quad e_\parallel = \frac{a_{epi}^\parallel - a_{epi}^0}{a_{epi}^0}. \quad (2.23)$$

Here, a_{epi}^0 denotes the lattice constant of the unstrained epitaxial layer. If the epitaxial layer is an alloy material, a_{epi}^0 can be expressed by Vegard’s law and the chemical composition can be determined by the relation

$$e_\perp = -\frac{2\nu}{1-\nu}e_\parallel, \quad (2.24)$$

where ν is the Poisson ratio, which was defined in equation (2.9).

For the superlattice structure, the average strain $\langle\varepsilon_{SL}\rangle$ and the average chemical composition \bar{x} can be determined analogously through the equations (2.21)-(2.24), but $\Delta\omega$ should be the peak separation between the zeroth order satellite of superlattice and the substrate peak, and ε_{epi}^\perp and $\varepsilon_{epi}^\parallel$ should be substituted by the average perpendicular $\langle\varepsilon_{SL}\rangle^\perp$ and parallel $\langle\varepsilon_{SL}\rangle^\parallel$ strains, respectively. $\langle\varepsilon_{SL}\rangle^\perp$ and $\langle\varepsilon_{SL}\rangle^\parallel$ are defined as

$$\langle\varepsilon_{SL}\rangle^\perp = \frac{T_a\varepsilon_{SL(a)}^\perp + T_b\varepsilon_{SL(b)}^\perp}{P}, \quad \langle\varepsilon_{SL}\rangle^\parallel = \frac{T_a\varepsilon_{SL(a)}^\parallel + T_b\varepsilon_{SL(b)}^\parallel}{P}, \quad (2.25)$$

where T_a and T_b are the individual layer width of the superlattice within one period and $P = T_a + T_b$ is the period. The period is determined according to the peak separation between the satellites, $\Delta\theta$, by

$$P = \frac{\lambda|\gamma_h|}{\Delta\theta \sin 2\theta_B}. \quad (2.26)$$

In principle, the chemical composition and the thickness of the individual layer can be obtained by simulating the experimental curves with x-ray diffraction theory. But if the deposition time of the individual layer is known, all these parameters can be directly obtained without simulation. Supposed there are two different layers within one period denoted as AC and $B_xA_{1-x}C$ and the deposition time for AC and $B_xA_{1-x}C$ is t_a and t_b , respectively. In

this case, the growth rate for AC and BC layers denoted as v_{AC} and v_{BC} , respectively, can be determined by

$$v_{AC} = \frac{P(1 - \bar{x})}{t_a + t_b}, \quad v_{BC} = \frac{P\bar{x}}{t_a + t_b}. \quad (2.27)$$

The chemical composition x is then determined by

$$x = \frac{v_{BC}}{v_{BC} + v_{AC}}. \quad (2.28)$$

Accordingly, the individual layer thicknesses of AC and $B_xA_{1-x}C$ are calculated by $t_a v_{AC}$ and $t_b v_{B_xA_{1-x}C}$.

X-ray diffraction of quantum wire arrays

X-ray diffraction is not only a powerful tool to characterize the vertically periodic structure, but is also sensitive to laterally surface-corrugated or periodic surface-modulated structures such as quantum wire [156, 157, 158, 159, 160] or quantum dot [161, 162, 163] arrays. The x-ray diffraction of a surface grating (or quantum wire arrays) can be regarded as a multi-slit Fraunhofer diffraction. The reason is, because the distance between the detector and the sample is much larger than the size of the sample, the diffraction belongs to the Fraunhofer regime. When the corrugation depth is much smaller than the extinction length, the kinematical theory can be used. The reflectivity, R , of quantum wire arrays for the Bragg case can be expressed as [157, 164]

$$R(\Delta\theta) = \Phi_h^2 D^2 I^2, \quad (2.29)$$

where $\Delta\theta$ is the angular deviation with respect to the Bragg angle. Φ_h can be expressed by the kinematical theory. If the corrugation is located in a vertical superlattice matrix, this term is written by the kinematical theory for the superlattice. D is called the diffraction term, which describes the contribution of the diffraction of a single slit (one period for the quantum wire array). Its concrete form can be obtained from the Fourier transform of the shape of the wire. If the quantum wire is rectangular-shaped, D becomes

$$D = \frac{\sin \beta}{\beta}, \quad (2.30)$$

with

$$\beta = \frac{\pi d \sin(2\theta_B) \cdot \Delta\theta}{\lambda \cos \theta_e}. \quad (2.31)$$

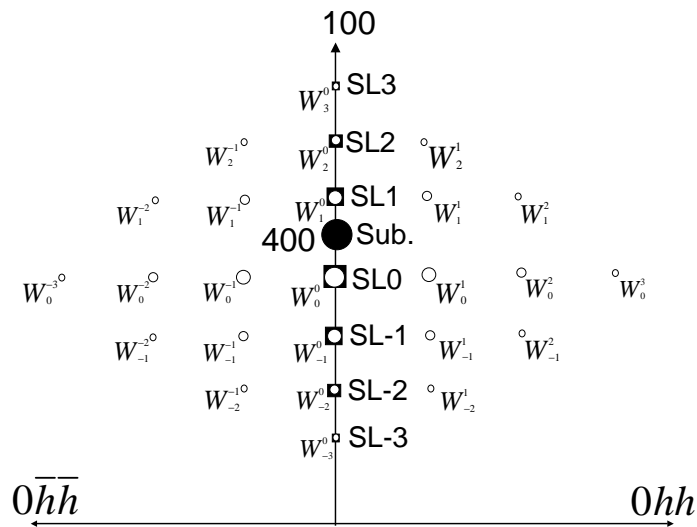


Figure 2.22: Schematic drawing showing the feature of x-ray diffraction of an ideal quantum wire array in reciprocal space in the vicinity of the 400 point of the substrate. SL and W denote the satellites due to superlattice and due to quantum wire array, respectively.

d is the width of the quantum wire and θ_e is the angle between the reflected beam and the surface of the sample. I in equation (2.29) is called the interference term, which describes the interference among the quantum wires:

$$I = \frac{\sin(N\alpha)}{N \sin \alpha}, \quad (2.32)$$

with

$$\alpha = \frac{\pi L \sin(2\theta_B) \cdot \Delta\theta}{\lambda \cos \theta_e}. \quad (2.33)$$

Here L is the period of the quantum wires and N is the number of the coherently illuminated quantum wires by the x-ray beam. This term is obtained from the Fourier transform of a Dirac- δ lattice with period L . When $\sin(N\alpha)/\sin \alpha = N$, i.e., $\alpha = \pm n\pi$, there are local maxima for the interference term. These local maxima of the interference term are called satellites of the quantum wires. Therefore, comparing to vertical superlattice structures, an extra series of satellites induced by the quantum wires will appear in the diffraction curve. Figure 2.22 schematically shows the features of the diffraction pattern of the quantum wire arrays in the vicinity of the substrate

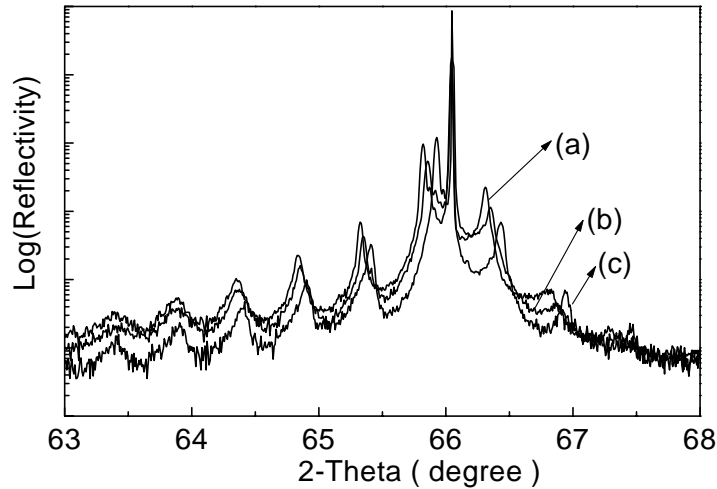


Figure 2.23: $\omega - 2\theta$ scans of samples SL25 (a), SL17 (b), and SL13 (c) (refer to the table on page 69) in the vicinity of the GaAs (400) reflection.

(400) diffraction in reciprocal space. The filled squares, denoted as SLi , are the satellites of the superlattice and the open circles, denoted as W_i^j , are the satellites due to the quantum wires. Accordingly, the period of the quantum wires is derived from the angular separation between the n_1 th and n_2 th satellites, $\Delta\theta_{n_1, n_2}$:

$$L = \frac{|n_1 - n_2| \lambda \cos \theta_e}{\Delta\theta_{n_1, n_2} \cdot \sin(2\theta_B)}. \quad (2.34)$$

As mentioned above, the XRD of the quantum wire arrays can be regarded as a multi-slit Fraunhofer diffraction. When the x-ray beam is perpendicular to the quantum wire arrays, the quantum wire satellites will appear, while for the x-ray beam parallel to the quantum wires, no quantum wire satellites will be available. Therefore, for the characterization of the quantum wire arrays, at least two diffractions with the x-ray beam perpendicular and parallel are required.

It should be noted that the period derived from equation (2.34) is not related to the wire shape because this relationship is deduced only from the interference term which is not related to the wire shape. If the sidewalls of the quantum wires are not rectangular-shaped, however, the satellites of quantum

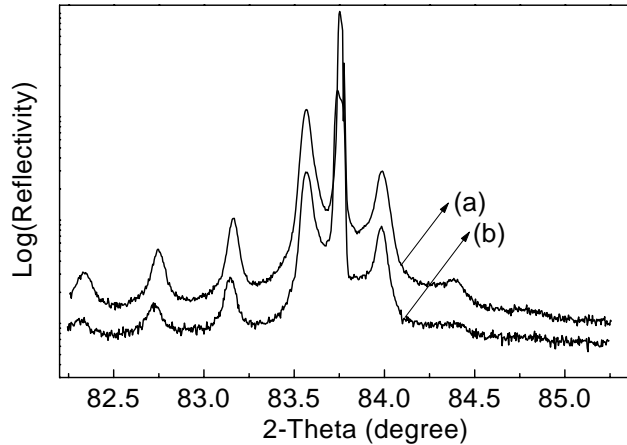


Figure 2.24: $\omega - 2\theta$ scans of the (422) glancing incidence reflections for sample SL25 (refer to the table on page 69) measured with the x-ray beam parallel (a) and perpendicular (b) to the wire axis.

wires will be smeared out to some degree. N in the interference term does not influence the positions of the wire satellites but their linewidths. The linewidth of the wire satellites decreases with increasing N . If $N \rightarrow \infty$, the satellites will become δ -like functions.

2.2.3 Results and discussions

Chemical composition

Figure 2.23(a), (b), and (c) depict the $\omega - 2\theta$ scans of samples SL25, SL17 and SL13 (refer to the table on page 69), respectively, measured with an open detector. The asymmetric measurements around the substrate GaAs (422) diffraction for sample SL25 are performed to reveal the in-plane lattice mismatch. Figures 2.24(a) and (b) show the glancing incidence (422) diffractions in the $[0\bar{1}1]$ and the $[011]$ azimuths, i.e., parallel and perpendicular to the wire direction, respectively. In principle, it is possible that the in-plane lattice strain along the wire could be different from that perpendicular to the wire owing to anisotropic elastic strain relaxation for the two directions [142]. However, the angular spacings between the zeroth order satellite and

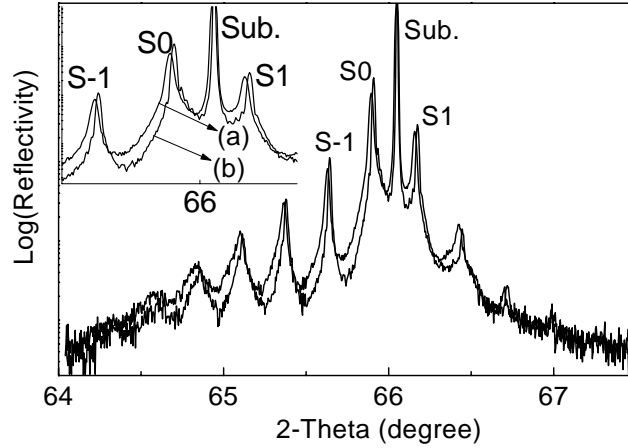


Figure 2.25: $\omega - 2\theta$ scans of samples SLC35 (a) and SLC28 (b) (refer to the table on page 69) in the vicinity of the GaAs (400) reflection. The inset shows the magnified spectrum around the 0-th satellite (S0).

the substrate peak for the (422) reflections measured with the x-ray beam parallel and perpendicular to the wire direction do not show a clear difference within the measurement resolution (14.4 arc seconds). Calculations by combining the (400) and (422) reflections prove that the growth of (In,Ga)As on GaAs for sample SL25 is coherent and the In composition is 25.6%. Since sample SL25 has the largest In composition among the three samples, it is thus reasonable to assume that (In,Ga)As growth on GaAs for samples SL17 and SL13 is also coherent. Accordingly, the obtained values of the In composition for samples SL17 and SL13 are 0.17 and 0.13, respectively.

Samples SLC35 and SLC28, which were continuously grown at 540°C, are characterized by XRD in the same way. Figure 2.25 depict the $\omega - 2\theta$ scans for samples SLC35 and SLC28, respectively. The In compositions of the (In,Ga)As single layer samples grown with the same In source temperatures as samples SLC35 and SLC28 should be the same as those of SLC35 and SLC28, respectively. The obtained values of the In composition for samples SLC35 and SLC28 are, however, 0.35 and 0.28 respectively, indicating that, during the growth of samples SL25 and SL17, the heating of the substrate from 540 to 580°C results in a desorption of In. As discussed above, the heating process might result in ripening, on the other hand, it causes In

desorption as proved by the results of x-ray diffraction. Evidently, to get more ordered 3D islands with low In composition, the heating of the substrate plays a crucial role.

Asymmetric x-ray diffraction for the self-organized quantum wires

For the characterization of the quantum wires with XRD, the choice of the diffraction geometry is very critical. The number of the coherently illuminated wires can be estimated by using the wave-coherence theory [159]:

$$N \approx \frac{\lambda}{\pi \Delta\theta \gamma_0 L}, \quad (2.35)$$

where $\Delta\theta$ denotes the horizontal divergence of the x-ray beam diffracted from the monochromator and incident on the sample, and the other symbols have been defined in the preceding part. After the diffraction on the sample, the divergence $\Delta\theta_h$ of the diffracted waves becomes:

$$\Delta\theta_h = |b| \Delta\theta. \quad (2.36)$$

Here, b , defined as $b = \gamma_0/\gamma_h$, is the asymmetry factor. Because only the waves whose wave fronts can overlap before reaching the detector can interfere, only a fraction of the coherently diffracted waves N can interfere on the detector. If the distance between the sample and the detector is denoted as D_0 , the fraction p can be expressed as:

$$p = \frac{b^2 \Delta\theta^2 \pi D_0}{\lambda}. \quad (2.37)$$

It can be seen that the number of the coherently diffracted waves which can interfere on the detector is proportional to the square of the asymmetry factor, b^2 . Thus, asymmetric diffraction with large incident angle and small exit angle, i.e., glancing exit reflection, is more sensitive than symmetric one to detect and analyze periodic surface corrugations like quantum wire or quantum dot arrays. As an example, for the commonly used asymmetric diffraction geometry, let's compare the (422) and (311) diffractions. b^2 for the glancing exit (422) and (311) reflections is 71.8 and 774.3, respectively, indicating that the glancing exit (311) reflection is the preferential choice.

Figures 2.26(a) and (b) show the (311) glancing exit diffractions ($\omega - 2\theta$ scans) for samples SL25 and SL17 measured with an open detector. When the

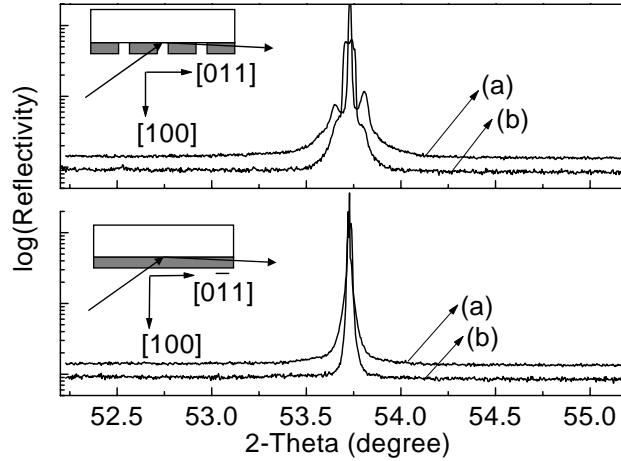


Figure 2.26: $\omega - 2\theta$ scans of the (311) glancing exit reflection. The top (bottom) is measured when the x-ray beam is perpendicular to (parallel to) the wire direction. (a) and (b) correspond to samples SL25 and SL17 (refer to the table on page 69), respectively. The insets show the schematic diffraction geometry.

x-ray beam is parallel to the $[0\bar{1}1]$ direction, i.e., the wire direction, only the substrate peak appears. On the other hand, for the x-ray beam perpendicular to the wires, three satellite peaks are visible with one of them having the same position as the substrate reflection. This confirms that the laterally periodic modulation exists in the whole epilayer stack. The satellite peaks are due to the interference induced by different slits (different gratings), therefore, the lateral period can be directly determined from the spacing between the satellites by using equation (2.34). The obtained values for samples SL25 and SL17 are 145 and 188 nm, respectively, implying that the lateral periodicity is related to the In composition and thus can be adjusted by it. Considering that x-ray diffraction averages over a relatively large volume, the appearance of the satellite peaks indicates that the lateral periodicity of the two samples is uniform.

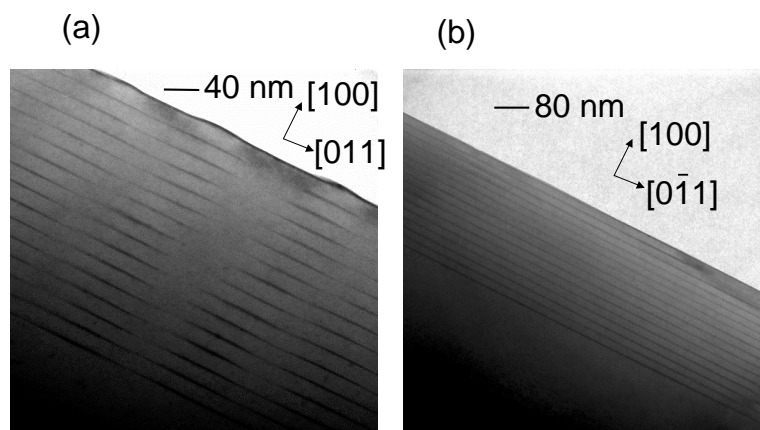


Figure 2.27: Bright field cross-sectional TEM images viewed along the $[0\bar{1}1]$ (a) and $[011]$ (b) directions of sample SL17 (refer to the table on page 69), respectively.

2.3 TEM characterization

To get detailed information about whether or not there are dislocations in the superlattice samples, transmission electron microscopy (TEM) measurements were performed. Different techniques usually have their advantages and, on the other hand, disadvantages, and usually are complimentary to each other. The technique of x-ray diffraction is very important, but it is only sensitive to the average strain state and is not sensitive to local dislocations. TEM is typically employed to characterize and image the defects in heteroepitaxial films [165, 166]. It is very sensitive to strain-relieving dislocations. In TEM, the image contrast is ascribed to differences in local diffraction caused by the strain field around the dislocations. But TEM is a microscopic technique and has a very small view field. It is only very sensitive to the local strain field on the order of 10 nm away from the dislocation core. TEM can only find the dislocations distributed very closely in space.

Figures 2.27(a) and (b) [Figures 2.28(a) and (b)] show the bright field cross-sectional TEM images viewed along the $[0\bar{1}1]$ and $[011]$ directions, respectively, of sample SL17 (SL25). Figures 2.27(a) and Figure 2.28(a) clearly

reveal that the wires are vertically aligned along the growth direction for the two samples. This vertical correlation of islands occurs because, as already discussed in section 2.2.1, island formation is favored at substrate locations where strain induces a local minimum of lattice mismatch if the spacer layer thickness is appropriately selected. For sample SL17 [Figure 2.27(a)], the lateral periodicity of the wires starting from the first layer is nearly as uniform as that of the other stacked wires. The cross-sectional TEM image of sample SL17 viewed along the $[011]$ direction shows a uniform superlattice structure. For sample SL25 [Figure 2.28(b)], some nonuniformity occurs, which is probably due to the wiggle of the wires along the $[0\bar{1}1]$ direction, as can be seen from the AFM image in Figure 2.17(a). Further cross-sectional TEM investigations were carried out, where the samples were tilted against the (011) zone axis, i.e., the $(\text{In,Ga})\text{As}/\text{GaAs}$ interface was inclined to the electron beam. The heavy contrast demonstrates that sample SL17 is dislocation-free from the first layer at the bottom to the topmost layer. For sample SL25, no dislocations are detected in the 13 layers from the bottom, however, in some parts of the top three layers, stacking faults are found. These stacking faults may be due to the accumulation of strain in the top layers as compared to the bottom ones.

In Figure 2.28(c), the islands in between the periodic wires in the initial several layers are attributed to nucleation sites where the strain field is not at a distinct minimum. Therefore, these intermediate islands disappear upon stacking more layers. This phenomenon can be well understood through the simulation developed by Tersoff et al using a generic model [139]. Figure 2.28(a) demonstrates this process in a very clear and direct way. Conclusively, our TEM results indicate that the growth of a superlattice improves the uniformity of the wires.

2.4 Lateral confinement of the quantum wires

2.4.1 Lateral confinement induced polarization anisotropy

In quantum wire structures, quantum confinement of electrons and holes is present in two dimensions with one dimension of free motion. The tailored density of states due to the two dimensional quantum confinement in such 1D system is directly reflected in the optical properties. Polarization analysis of the optical spectra has been used to evaluate the extent of the lateral carrier

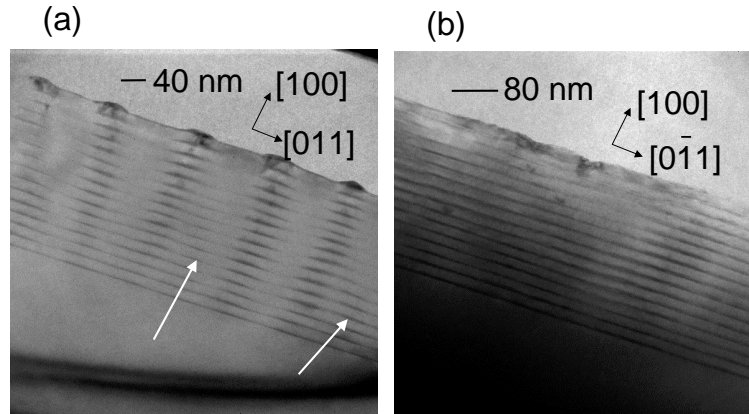


Figure 2.28: Bright field cross-sectional TEM images viewed along the $[0\bar{1}1]$ (a) and $[011]$ (b) directions of sample SL25 (refer to the table on page 69), respectively. The arrows denote the areas of the intermediate islands.

confinement in unstrained quantum wires [167, 168, 169, 170, 171, 172, 173, 20, 174]. First, we will give a very brief explanation about the origin of the lateral confinement induced linear polarization effect in the absorption and luminescence spectra for quantum wire structures, for which we follow the theoretical analysis done by Bockelmann and Bastard [175]. Instead of giving the detailed deduction process, only conclusions are presented.

The conduction-band (Γ_6) wave functions are written as

$$\Psi_{m_s}^c(\mathbf{r}) = f(\mathbf{r})^c u_{m_s}^c(\mathbf{r}), \quad (2.38)$$

where f^c denotes the envelope wave function and $u_{m_s}^c$ are the two spin-degenerate ($s = \frac{1}{2}$, $m_s = \pm\frac{1}{2}$) Bloch functions at the bottom of the Γ_6 bulk band ($\mathbf{K} = 0$). The valence band (Γ_8) at $\mathbf{K} = 0$ is four-fold degenerate including the two-fold degenerate subbands for heavy holes ($m_j = \pm\frac{3}{2}$) and the two-fold degenerate subbands for light holes ($m_j = \pm\frac{1}{2}$). The valence band wave functions are written as

$$\Psi^v(\mathbf{r}) = \sum_{m_j} f_{m_j}^v(\mathbf{r}) u_{m_j}^v(\mathbf{r}). \quad (2.39)$$

Here, $u_{m_j}^v(\mathbf{r})$ are the degenerate Bloch functions at the top of the Γ_8 bulk bands. The eigen wave function of the conduction band is obtained by solving the Schrödinger equation based on the effective mass approximation and that of the valence band is obtained by solving the Schrödinger equation using the Luttinger Hamiltonian. If the polarization vector of the light wave, ε , is expressed in spherical coordinates as $\varepsilon = (\cos \varphi \sin \theta, \sin \varphi \sin \theta, \cos \theta)$, finally, the dipole matrix element of the transition between the conduction band and the valence band is written as

$$\sum_{m_s} |\langle \Psi_{m_s}^c | \varepsilon \cdot \mathbf{p} | \Psi^v \rangle|^2 = \left[\frac{m_0 P}{\hbar} \right]^2 \begin{cases} \frac{2}{3}(J_{\frac{1}{2}}^2 + J_{-\frac{1}{2}}^2), & \text{for } \theta = 0 \\ \frac{1}{2}(J_{\frac{3}{2}}^2 + J_{-\frac{3}{2}}^2) + \frac{1}{6}(J_{\frac{1}{2}}^2 + J_{-\frac{1}{2}}^2) \\ -\frac{1}{\sqrt{3}}(J_{\frac{3}{2}} J_{-\frac{1}{2}} + J_{\frac{1}{2}} J_{-\frac{3}{2}}) \cos(2\varphi), & \text{for } \theta = \frac{\pi}{2} \end{cases} \quad (2.40)$$

and

$$\langle \Psi_{m_s}^c | \varepsilon \cdot \mathbf{p} | \Psi^v \rangle = \sum_{m_j} J_{m_j} \langle u_{m_s}^c | \varepsilon \cdot \mathbf{p} | u_{m_j}^v \rangle, \quad J_{m_j} = \langle f^c(\mathbf{r}) | f_{m_j}^v(\mathbf{r}) \rangle. \quad (2.41)$$

It can be seen from equation (2.40) that the in-plane anisotropy of the transition probability is related to the term proportional to $\cos(2\varphi)$. In 2D systems, this term is eliminated by the summation over the in-plane wave vectors. In 1D systems, this term survives the integration over the in-wire momentum. Therefore, the appearance of a linear polarization anisotropy in the absorption and luminescence spectra in 1D systems is due to the mixing of the $j = \pm\frac{3}{2}$ and $j = \pm\frac{1}{2}$ hole states of the valence subbands. Decoupled states would not result in an in-plane polarization anisotropy. Anything changing the total symmetry of the valence band will bring about the effect of polarization anisotropy in the absorption or luminescence spectra. In quantum wire structures, the lateral carrier confinement results in such a breaking of the symmetry of the valence band. Therefore, polarization anisotropy can be used as a test of the lateral carrier confinement in quantum wire structures. However, this only holds for unstrained systems. The strain in quantum wire structures is intrinsically nonbiaxial, but triaxial [176]. Thus, the anisotropic strain can also cause polarization effects by modifying the symmetry of the valence band [177]. It has been realized quite recently that the polarization anisotropy of strained quantum wire structures arises from the contributions mixed with the strain and the lateral carrier confinement [178].

2.4.2 Separation of strain and lateral confinement induced polarization anisotropy

Magneto-optical measurements can separate the contributions of lateral confinement and strain to the polarization anisotropy [176, 179, 180]. When the magnetic field is applied normal to the in-wire plane (xy plane), a magnetic potential which is quadratically proportional to the magnetic field B is introduced in the xy plane [181]. The in-plane motions of the excitons are then quantized into a series of separate orbits, called cyclotron orbits and the corresponding energy states are a series of quantized Landau levels. The magnetic field does not influence the motion of the excitons along its direction. The quantum wire states are determined by the magnetic potential and the lateral confinement potential. The magnetic field confinement will compete with the lateral confinement. The cyclotron orbit diameter is expressed as

$$2\left(\frac{\hbar}{eB}\right)^{\frac{1}{2}}(2n+1)^{\frac{1}{2}}, n = 0, 1, 2, 3, \dots \quad (2.42)$$

where n denotes the different Landau levels. When the magnetic field is small and the diameter of the Landau orbit is larger than the width of the quantum wire, lateral confinement dominates over the diamagnetic shift and the magnetic confinement can be regarded as a perturbation [182, 183]. In this case, the diamagnetic shift has a B^2 dependent tendency. When the magnetic field is large enough so that the diameter of the Landau orbit is smaller than the width of the quantum wire, the diamagnetic shift is dominated by the magnetic confinement [184, 185, 186, 187]. Then the diamagnetic shift is linearly dependent on the magnetic field B . Therefore, the changeover point of magnetic field for diamagnetic shift from parabolic to linear tendency is a quantitative measure for the lateral carrier confinement in the quantum wires. The larger the changeover magnetic field is, the larger the lateral confinement of carriers is. On the other hand, since the influence of the magnetic field on the strain can be ignored [182], if the optical polarization anisotropy is only induced by the strain, the polarization anisotropy will not change with the magnetic field. If the optical polarization anisotropy is only induced by the lateral confinement, polarization anisotropy should be suppressed at a high magnetic field. As a rough estimation, the difference of the degree of polarization anisotropy measured between 0 Tesla and a high magnetic field can be considered as only induced by the lateral confinement.

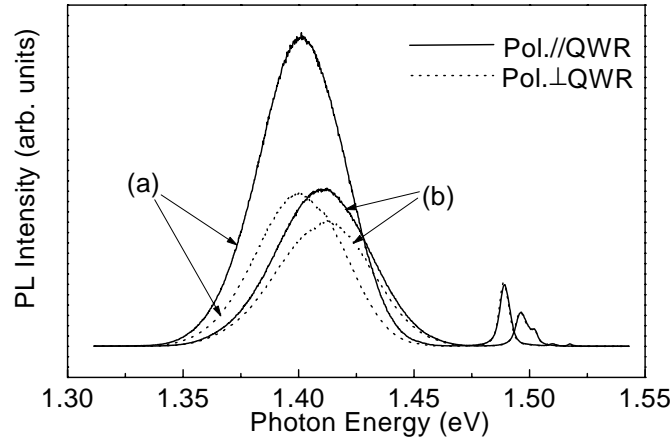


Figure 2.29: Linear polarization resolved magneto-PL spectra of sample SL17 (refer to the table on page 69) measured at 10 K with the applied vertical magnetic field of 0 (a) and 14 Tesla (b). The solid and dotted lines are measured for the detected polarization parallel and perpendicular to the wire axis, respectively.

2.4.3 Results and discussion

For the magneto-PL measurements, the 514.5 nm line of an Ar^+ laser is used as the excitation light which passes through an optical fiber attached to the surface of the sample. The luminescence from the sample is collected through the same fiber and is then dispersed through a monochromator. The sample is mounted in a superconducting magnet which generates the magnetic field. In our case, the maximum magnetic field available is 14 Tesla. The magnetic field is applied in the Faraday configuration in which the applied magnetic field is parallel to the normal of the surface of the sample (z direction), i.e., $\mathbf{B} \parallel z$. The emitted light is also collected in z direction.

Figures 2.29(a) and (b) depict the linear polarization dependent PL spectra of sample SL17 measured at 10 K with the applied vertical magnetic field of 0 and 14 Tesla, respectively. The solid and the dotted lines correspond to the PL spectra measured with the detected polarization parallel and perpendicular to the wire direction, respectively. But the polarization anisotropy is decreased in the presence of the magnetic field. Significant in-plane polarization anisotropy with the preferential emission along the wire axis is observed.

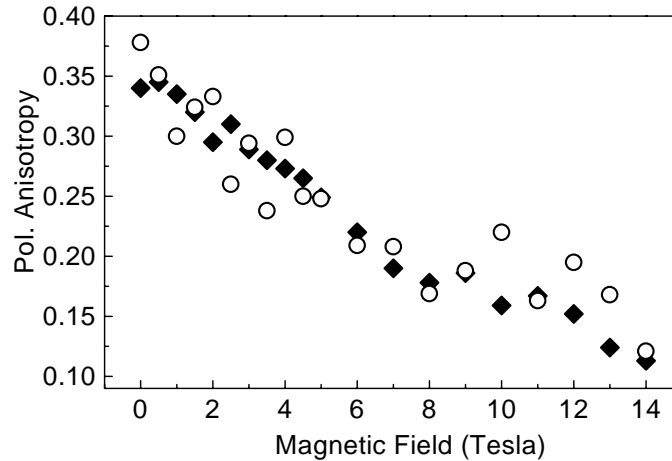


Figure 2.30: Degree of the polarization anisotropy measured under magnetic field with the excitation power of 0.664 mW (solid squares) and 0.013 mW (open circles) for sample SL17 (refer to the table on page 69).

The linewidth of the PL spectra is 46 meV and does almost not change with changing the applied magnetic field. The blueshift of the peak when the magnetic field is applied is the so-called “diamagnetic shift”. When no magnetic field is applied, the peak at 1.490 eV is related to carbon acceptors in the substrate and the peak at 1.510 eV is related to bulk GaAs. When the applied magnetic field is 14 Tesla, the shoulder at the high energy side of the peak related to the carbon acceptors in the substrate is regarded to be due to Zeeman splitting. Polarization measurements should, however, be treated very carefully since many things can cause polarization effects [188]. Because the gratings in the monochromator might also have a polarization effect, in order to eliminate this grating effect, the measured PL spectra are carefully calibrated by the peak of the bulk GaAs and the carbon acceptor induced peak, for which there should be no polarization effects.

Figure 2.30 displays the dependence of the polarization anisotropy at the wire peak position as a function of the applied vertical magnetic field measured with the excitation power of 0.664 mW (solid squares) and 0.0133 mW (open circles), respectively. When the excitation power is 0.664 mW, the degree of the polarization anisotropy, defined as $(I_{\parallel} - I_{\perp}) / (I_{\parallel} + I_{\perp})$, decreases continuously from 0.34 to 0.11 when increasing the vertical magnetic from 0

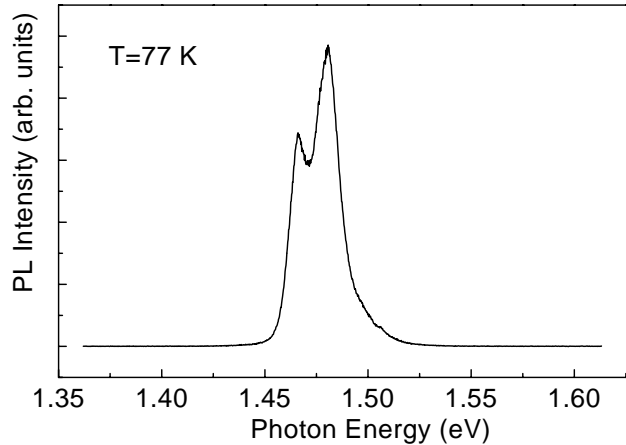


Figure 2.31: PL spectrum of sample SL13 (refer to the table on page 69) measured at 77 K.

to 14 Tesla, where I_{\parallel} and I_{\perp} denote the PL intensities with the detected polarization parallel and perpendicular to the wire direction, respectively. This demonstrates that the polarization anisotropy is predominantly induced by the lateral confinement. As discussed above, the degree of the polarization anisotropy induced by the lateral confinement in this sample is at least 0.23 demonstrating that the lateral confinement is strong. Because piezoelectric effects are found for this sample (which will be discussed in 2.5), we measured the polarization anisotropy at different excitation power. The open squares in Figure 2.30 depict the measured polarization anisotropy with the applied magnetic field at the excitation power of 0.0133 mW. In principle, a piezoelectric field can influence the polarization effect by modifying the confinement potential. As can be seen in Figure 2.30, the polarization anisotropy measured under different excitation power reveals the same tendency and shows a difference of only several percent. We thus conclude that the degree of polarization anisotropy due to piezoelectric effects is less than several percents. The piezoelectric effect plays thus only an insignificant role for the polarization effect.

As a comparison, for sample SL13 whose surface morphology does not exhibit any islands as shown in Figure 2.19, we did not observe any polarization effects. Figure 2.31 shows the PL spectrum of sample SL13 measured at

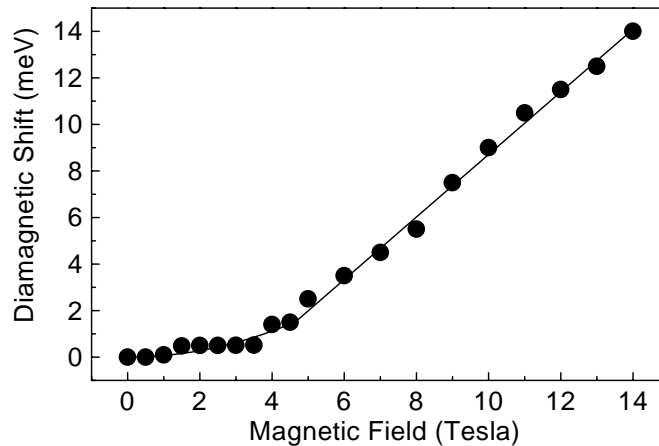


Figure 2.32: Diamagnetic shift of the PL peak of the quantum wire of sample SL17 (refer to the table on page 69). The solid lines show parabolic and linear fit to the experimental points for the magnetic field smaller and larger, respectively, than 4.5 Tesla.

77 K. The peak located at 1.467 eV is due to the (In,Ga)As/GaAs quantum well. The very small peak at 1.508 eV is due to the bulk GaAs and the peak position is in agreement with the empirical relation of the bulk GaAs band gap: $E_g = 1.519 - 5.408 \times 10^{-4}T^2/(T + 204)$, where T denotes the temperature in units of K. The peak located at 1.483 eV is attributed to the carbon acceptors in the substrate. Compared to the quantum wire samples, the peak due to the carbon acceptors is very strong for sample SL13. The reason could be that, because the peak separation between the wire and the carbon acceptor peaks for the quantum wire samples is larger than that between the (In,Ga)As/GaAs quantum well and the carbon acceptors, the photogenerated carriers in the substrate, which have a higher energy than those in the wire region, more easily diffuse to the wire region and then recombine [189]. For sample SL13, no peak shift is observed upon changing the excitation power indicating the absence of a piezoelectric effect. These results reflect in another perspective that the polarization anisotropy observed for sample SL17 indeed arises from the lateral carrier confinement in the quantum wires.

Figure 2.32 depicts the measured diamagnetic shift as a function of the applied magnetic field from 0 to 14 Tesla. At low magnetic fields, a parabolic tendency is observed, while a linear tendency is observed at high magnetic

fields. This transition clearly indicates the changeover from the dominant lateral carrier confinement to the dominant magnetic confinement. The changeover point of the magnetic field for the diamagnetic shift from the parabolic to the linear tendency occurs at 4.5 Tesla and the corresponding diameter of the cyclotron orbit is 24.2 nm for $n = 0$. This value is even smaller than the wire width obtained from the cross-sectional TEM image. The difference could arise from the fact that the edges of the wires are usually highly strained area and the excitons are only confined in the central part of the wire region resulting in a smaller effective confinement area. A similar phenomenon has been reported for self-organized InAs/InP quantum wire structures [190]. The parabolic tendency of the diamagnetic shift for a magnetic field smaller than 4.5 Tesla is fitted by $\Delta E = \beta B^2$ with $\beta = 73 \mu\text{eV}/\text{Tesla}^2$ as shown as solid line in Figure 2.32, where ΔE denotes the diamagnetic field. The fitted curve agrees well with the experimental curve.

2.5 Piezoelectric effect

Zincblende III-V semiconductors are piezoelectric crystals. They should demonstrate piezoelectric effect. Smith first predicted large piezoelectric effects in strained heterostructures grown on (111) oriented substrate in 1986 [191]. Because the strain induced piezoelectric field can modify the band gap structure of quantum well structures, it offers another design parameter for novel optical and electronic devices. Since then great efforts have been devoted to the study of the piezoelectric effect in semiconductors [192, 193, 194, 195, 196, 197, 198, 199, 200, 201, 202, 203, 204]. The strain brings about the piezoelectric polarization whose direction depends on the symmetry of the lattice of the substrate and the orientation of the surface [205]. When the piezoelectric polarization crosses from one heterostructure to another, an abrupt change will occur [192]. The divergence of piezoelectric polarization gives piezopolarization charges expressed as $\rho_{pol} = -\nabla \cdot \mathbf{P}$, where ρ_{pol} and \mathbf{P} denote the piezopolarization charges and the piezopolarization, respectively. Therefore, the piezopolarization charges are only distributed at the interface of the heterostructure thus generating a piezoelectric field. The distribution of the piezoelectric field can be obtained by solving Poisson's equation. Piezopolarization is connected to the strain by the piezoelectric tensor which is the third rank. For zincblende symmetry, using the contracted

denotation for the piezoelectric tensor, the relationship between the piezopolarization and the strain is given by $P_i = e_{14}\varepsilon_{jk}$ [191], which is equivalent to the matrix format below

$$\begin{pmatrix} P_1 \\ P_2 \\ P_3 \end{pmatrix} = \begin{pmatrix} 0 & 0 & 0 & e_{14} & 0 & 0 \\ 0 & 0 & 0 & 0 & e_{14} & 0 \\ 0 & 0 & 0 & 0 & 0 & e_{14} \end{pmatrix} \begin{pmatrix} \varepsilon_{11} \\ \varepsilon_{22} \\ \varepsilon_{33} \\ \varepsilon_{23} \\ \varepsilon_{31} \\ \varepsilon_{12} \end{pmatrix}, \quad (2.43)$$

where the subscripts 1, 2, 3 represent the x, y, z axes, respectively, and ε_{jk} denote the different components of the strain tensor referred to the crystalline axes. The symmetry of the strain tensor leads to $\varepsilon_{13} = \varepsilon_{31}$, $\varepsilon_{23} = \varepsilon_{32}$ and $\varepsilon_{12} = \varepsilon_{21}$. It can be seen from equation 2.43 that only shear strain induces piezopolarization for zinblende structure [206, 207, 208], namely, the piezopolarization is generated only if the strain distorts the angles of the cubic unit cell away from 90° .

For a pseudomorphic layer grown on (110) substrates, the piezopolarization occurs and its direction is parallel to the surface, but the piezoelectric field is absent because there are no “boundaries ” for the piezopolarization charges to generate piezoelectric field [205]. In practice, even for a quantum well structure grown on (110) substrates, the lateral piezoelectric field exists due to the consequence of interface fluctuations which always exist and can be regarded as such “boundaries ” for piezopolarization charges [209]. The lateral piezoelectric field on (110) oriented substrates have been demonstrated experimentally [209]. For a quantum well structure grown on (111) substrates, the piezopolarization is along the growth direction, therefore, only a vertical piezoelectric field exist. For the other non-(100) substrate orientations, piezopolarization and piezoelectric field usually have both lateral and vertical components [210, 211]. For a quantum well structure grown on (100) oriented substrates, because shear strains are zero, no piezopolarization and piezoelectric field exist. However, for a quantum wire structure on (100) substrates, shear deformations could be present at the edges of the wires, then piezopolarization is generated. But the shear strain is related to the wire axis in this case. If the quantum wire is along the [001] direction, shear deformations vanish, while, if the quantum wire is along the $[0\bar{1}1]$ direction, shear strain survives [212]. In this case, if we denote the growth direction as z , ε_{xy} , i.e., ε_{12} is not zero. It can be seen from equation 2.43 that the

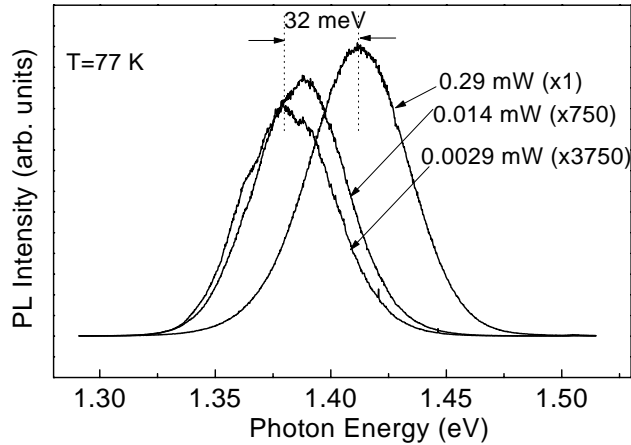


Figure 2.33: PL spectra of sample SL17 (refer to the table on page 69) measured at different excitation power.

piezopolarization is along the z axis, i.e., the growth direction and accordingly, also the piezoelectric field [212]. This problem has been treated in Ref. [212]. This point can be understood as due to a change of “boundary conditions”. For a quantum well on (100) substrates, the boundary condition requires the stress along the $[100]$ direction to be zero, i.e., $T_{[100]} = 0$, but for a quantum wire structure oriented along the $[0\bar{1}1]$ direction, the boundary condition becomes $T_{[100]} = T_{[011]} = 0$, i.e., the stresses along the $[100]$ and the $[011]$ directions are zero. This point has been confirmed in quantum well structures which are grown on $[100]$ substrate orientation, but mesa-etched along the $[0\bar{1}1]$ direction [212].

The self-organized (In,Ga)As quantum wires grown on (100) substrates are oriented along the $[0\bar{1}1]$ direction. Thus piezoelectric effects are expected. For this purpose, excitation power dependent PL measurements are performed. Figure 2.33 depicts the PL spectra of sample SL17 measured at different excitation power. The measurement temperature is 77 K. When changing the power of the excitation light from 0.0029 to 0.29 mW, the quantum wire peak blueshifts by about 32 meV, which is strikingly large. Because the photogenerated carriers partly screen the internal piezoelectric field, the reduced internal electric field results in a blueshift. In this case, due to the direction of the piezoelectric field along the growth direction, it

is similar to the Stark effect. A larger excitation power results in more photogenerated carriers, then the screening of the internal piezoelectric field is more pronounced. For comparison, the superlattice quantum well sample, SL13, was measured in the same way. The PL peak position does not change with changing the excitation power indicating the absence of piezoelectric effects. Therefore, the observed blueshift for sample SL25 proves the existence of piezoelectric effects.

Summary

This work has described fabrication technologies and properties of two types of quantum wire structures based on the selective growth on the mesa stripe patterned GaAs(311)A and on the self-organized formation of elongated 3D islands in the strained (In,Ga)As/GaAs(100) system by MBE. For the former case, single stacked sidewall quantum wires with strong electronic coupling have been fabricated. p-i-n type LED's of the sidewall quantum wires on patterned GaAs (311)A substrates using all Si doping for the n- and p-type regions have been fabricated. The EL spectra have shown strong selectivity of the quantum wire emission with a steeper increase in intensity compared to that of the surrounding quantum wells with increasing forward bias. The EL from the quantum wires has been directly observed through an optical microscope as a bright line within the otherwise rather dark region inside the ring contacts of the diode. The selectivity of carrier injection was reduced when increasing the temperature due to the increased thermal escape of carriers from the quantum wire region into the quantum well region. But even up to room temperature, the emission density in the quantum wire region is locally enhanced by two orders of magnitude compared to that from the quantum-well regions. The samples were characterized by micro-PL, CL, as well as EBIC measurements. The EBIC results have shown an enhanced carrier capture in the quantum wire region when increasing the applied forward bias. To account for the highly selective EL, a model has been proposed, which is based on the lateral diffusion of electrons and holes resulting in self-enhanced carrier injection into the quantum wires. The results have provided insight into the operation of light-emitting devices based on lateral nanostructures, which may be advantageous for optical fiber applications utilizing a locally enhanced emission density from single quantum wires and quantum dots.

The influence of atomic hydrogen on the surface morphology of (In,Ga)As

grown on GaAs(311)A has been studied. It was found that atomic hydrogen suppresses island formation and delays the relaxation by islanding thus playing a surfactant role in the growth of (In,Ga)As on GaAs(311)A. It has been proposed that atomic hydrogen decreases the adatom migration length in lattice mismatched systems. Atomic hydrogen has been applied to the growth of strained (In,Ga)As sidewall quantum wires enlarging the PL peak separation between the quantum wires and the quantum well.

For the latter case, the growth of (In,Ga)As single layers on GaAs (100) substrate has been investigated. It was shown that the growth of the coherent 3D islands is a kinetically limited process. The transition from square shaped islands to elongated islands was observed by changing the growth temperature of (In,Ga)As single layers. Under certain growth conditions, the increase in height of 3D islands is kinetically limited and the islands may grow only laterally keeping their height almost constant. This is the prerequisite for the shape transition. The elongation of the islands is a tradeoff between the surface free energy and the strain energy. A quantitative comparison between our experimental results and the theoretical work done by Tersoff and Tromp shows a good agreement. Self-organized quantum wires based on the elongated islands have been fabricated. The uniformity of the quantum wires has been greatly improved by a superlattice growth scheme which also makes the wires much longer (several μm). The structural characterization of the quantum wires has been performed by AFM, XRD, and TEM. The quantum wires are dislocation-free and vertically correlated. A large polarization anisotropy of PL for the quantum wires has been observed. Magneto-PL measurements have demonstrated that the polarization anisotropy is predominantly induced by the lateral carrier confinement. Piezoelectric effects of the quantum wires were also discussed. Our results may experimentally pave a way to the fabrication of very long and uniform quantum wires. The quantum wires may have practical applications in optoelectronic devices.

References

- [1] E. O. Göbel and K. H. Ploog *Prog. Quant. Electr.*, **14**, 289 (1991).
- [2] W. T. Tsang *Appl. Phys. Lett.*, **39**, 786 (1981).
- [3] Y. Arakawa and H. Sakaki *Appl. Phys. Lett.*, **40**, 939 (1982).
- [4] Y. Arakawa and A. Yariv *IEEE J. Quant. Electr.*, **QE-22**, 1887 (1982).
- [5] M. Asada, Y. Miyamoto, and Y. Suematsu *Jpn. J. Appl. Phys.*, **24**, L95 (1985).
- [6] P. M. Petroff, A. C. Gossard, R. A. Logan, and W. Wiegmann *Appl. Phys. Lett.*, **41**, 635 (1982).
- [7] Y. Hirayama, S. Tarucha, Y. Suzuki, and H. Okamoto *Phys. Rev. B*, **37**, 2774 (1988).
- [8] K. Yamaguchi and K. Okamoto *Appl. Phys. Lett.*, **59**, 3580 (1991).
- [9] S. Koshiba, H. Noge, H. Akiyama, T. Inoshita, Y. Nakamura, A. Shimizu, Y. Nagamune, M. Tsuchiya, H. Kano, H. Sakaki, and K. Wada *Appl. Phys. Lett.*, **64**, 363 (1994).
- [10] W. Stolz, in *Low dimensional structures prepared by epitaxial growth or regrowth on patterned substrates*, edited by K. Eberl and P. M. Petroff and P. Demeester, p. 301. Dordrecht: Kluwer Academic Publishers, 1995.
- [11] E. Kapon, M. C. Tamargo, and D. M. Hwang *Appl. Phys. Lett.*, **50**, 347 (1987).
- [12] E. Kapon, G. Biasiol, D. M. Hwang, and E. Colas, in *Low dimensional structures prepared by epitaxial growth or regrowth on patterned substrates*, edited by K. Eberl and P. M. Petroff and P. Demeester, p. 291. Dordrecht: Kluwer Academic Publishers, 1995.
- [13] F. Vouilloz, D. Y. Oberli, M.-A. Dupertuis, A. Gustafsson, F. Reinhardt, and E. Kapon *Phys. Rev. B*, **57**, 12378 (1998).
- [14] E. Kapon, D. M. Hwang, and R. Bhat *Phys. Rev. Lett.*, **63**, 430 (1989).
- [15] L. Pfeiffer, H. L. Störmer, K. West, and K. W. Baldwin *J. Cryst. Growth*, **111**, 333 (1991).
- [16] Y. C. Chang, L. L. Chang, and L. Esaki *Appl. Phys. Lett.*, **47**, 1324 (1985).
- [17] W. Wegscheider, L. Pfeiffer, K. West, and R. E. Leibenguth *Appl. Phys. Lett.*, **65**, 2510 (1994).
- [18] P. M. Petroff, A. C. Gossard, and W. Wiegmann *Appl. Phys. Lett.*, **45**, 620 (1984).
- [19] M. Sundaram, S. A. Chalmers, P. Hopkins, and A. C. Gossard *Science*, **254**, 1326 (1991).

- [20] M. S. Miller, H. Weman, C. E. Pryor, M. Krishnamurthy, P. M. Petroff, H. Kroemer, and J. L. Merz *Phys. Rev. Lett.*, **68**, 3464 (1992).
- [21] P. M. Petroff and S. P. DenBaars *Superlattices and Microstructures*, **15**, 15 (1994).
- [22] A. Madhukar, Q. Xie, P. Chen, and A. Konkar *Appl. Phys. Lett.*, **64**, 2727 (1994).
- [23] N. N. Ledentsov, M. Grundmann, N. Kirstaedter, O. Schmidt, R. Heitz, J. Böhrer, D. Bimberg, V. M. Ustinov, V. A. Shchukin, A. Y. Egorov, A. E. Zhukov, S. Zaitsev, P. S. Kop'ev, Z. I. Alferov, S. S. Ruvimov, A. O. Kosogov, P. Werner, U. Gösele, and J. Heydenreich *Solid State Electronics*, **40**, 785 (1996).
- [24] N. N. Ledentsov, V. M. Ustinov, V. A. Shchukin, P. S. Kopev, Z. I. Alferov, and D. Bimberg *Semiconductors*, **32**, 343 (1998).
- [25] V. A. Shchukin and D. Bimberg *Appl. Phys. A*, **67**, 687 (1998).
- [26] A. Ponchet, A. L. Corre, H. L'Haridon, B. Lambert, and S. Salaün *Appl. Phys. Lett.*, **67**, 1850 (1995).
- [27] H. Li, T. Daniels-Race, and Z. Wang *J. Cryst. Growth*, **200**, 321 (1999).
- [28] K. Tillmann, D. Gerthsen, P. Pfundstein, A. Förster, and K. Urban *J. Appl. Phys.*, **78**, 3824 (1995).
- [29] L. González, J. García, R. García, F. Briones, J. Martínez-Pastor, and C. Ballesteros *Appl. Phys. Lett.*, **76**, 1104 (2000).
- [30] C. Walther, J. Erxmeyer, E. Schippel, L. Hoering, and W. T. Masselink, in *26th Int. Symp. Compound Semiconductors*, Inst. Phys. Conf. Ser. No. 166, p. 195, IOP, Bristol, 2000.
- [31] R. Nötzel, J. Menninger, M. Ramsteiner, A. Ruiz, H.-P. Schönherr, and K. H. Ploog *Appl. Phys. Lett.*, **68**, 1132 (1996).
- [32] R. Nötzel, J. Menninger, M. Ramsteiner, A. Trampert, H.-P. Schönherr, L. Däweritz, and K. H. Ploog *J. Cryst. Growth*, **175/176**, 1114 (1997).
- [33] J. Fricke, R. Nötzel, U. Jahn, H.-P. Schönherr, L. Däweritz, and K. H. Ploog *J. Appl. Phys.*, **85**, 3576 (1999).
- [34] R. Nötzel *Microelectronics J.*, **28**, 875 (1997).
- [35] R. Nötzel, M. Ramsteiner, J. Menninger, A. Trampert, H.-P. Schönherr, L. Däweritz, and K. H. Ploog *J. Appl. Phys.*, **80**, 4108 (1996).
- [36] Q. Gong, R. Nötzel, H.-P. Schönherr, and K. H. Ploog *J. Cryst. Growth*, **220**, 23 (2000).
- [37] R. Nötzel, M. Ramsteiner, J. Menninger, A. Trampert, H.-P. Schönherr, L. Däweritz, and K. H. Ploog *Jpn. J. Appl. Phys.*, **35**, L297 (1996).
- [38] P. V. Santos, R. Nötzel, and K. H. Ploog *J. Appl. Phys.*, **85**, 8228 (1999).
- [39] A. Richter, G. Behme, M. Süptitz, C. Lienau, T. Elsaesser, M. Ramsteiner, R. Nötzel, and K. H. Ploog *Phys. Rev. Lett.*, **79**, 2145 (1997).
- [40] H. Weman, D. Y. Oberli, M.-A. Dupertuis, F. Reinhardt, A. Gustafsson, and E. Kapon *Phys. Rev. B*, **58**, 1150 (1998).

- [41] G. Schedelbeck, W. Wegscheider, M. Bichler, and G. Abstreiter *Science*, **278**, 1792 (1997).
- [42] S. Fafard, M. Spanner, J. P. McCaffrey, and Z. R. Wasilewski *Appl. Phys. Lett.*, **76**, 2268 (2000).
- [43] H. G. Roskos, M. C. Nuss, J. Shah, K. Leo, D. A. B. Miller, A. M. Fox, S. Schmitt-Rink, and K. Köhler *Phys. Rev. Lett.*, **68**, 2216 (1992).
- [44] J. Shah, in *Optics of semiconductor nanostructures*, edited by F. Henneberger and S. Schmitt-Rink and E. O. Göbel, p. 149. Berlin: Akademie Verlag, 1993.
- [45] J. A. del Alamo and C. C. Eugster *Appl. Phys. Lett.*, **78**, 78 (1990).
- [46] G. S. Solomon, J. A. Trezza, A. F. Marshall, and J. S. Harris Jr. *Phys. Rev. Lett.*, **76**, 952 (1996).
- [47] G. S. Solomon, M. C. Larson, and J. S. Harris Jr. *Appl. Phys. Lett.*, **69**, 1897 (1996).
- [48] L. Aigouy, T. Holden, F. Pollak, N. N. Ledentsov, W. M. Ustinov, P. S. Kop'ev, and D. Bimberg *Appl. Phys. Lett.*, **70**, 3329 (1997).
- [49] A. Tackeuchi, Y. Nakata, S. Muto, Y. Sugiyama, T. Inata, and N. Yokoyama *Jpn. J. Appl. Phys.*, **34**, L405 (1995).
- [50] K. Komori, X. Wang, M. Ogura, H. Matsuhata, and H. Imanishi *Appl. Phys. Lett.*, **68**, 3787 (1996).
- [51] K. Komori, X. Wang, M. Ogura, and H. Matsuhata *Appl. Phys. Lett.*, **71**, 3350 (1997).
- [52] K. Komori and M. Arakawa *Jpn. J. Appl. Phys.*, **36**, 1927 (1997).
- [53] R. Nötzel, U. Jahn, Z. Niu, A. Trampert, J. Fricke, H.-P. Schönherr, T. Kurth, D. Heitmann, L. Däweritz, and K. H. Ploog *Appl. Phys. Lett.*, **72**, 2002 (1998).
- [54] D. Gershoni, I. Brener, G. A. Baraff, S. N. G. Chu, L. N. Pfeiffer, and K. West *Phys. Rev. B*, **44**, 1930 (1991).
- [55] O. Madelung, ed., *Landolt-Börnstein*, **17a**. Berlin: Springer Verlag, 1982.
- [56] J.-B. Xia *Phys. Rev. B*, **43**, 9856 (1991).
- [57] R. Nötzel and K. H. Ploog *International J. Modern Phys. B*, **7**, 2743 (1993).
- [58] R. L. Greene, K. K. Bajaj, and D. E. Phelps *Phys. Phys. B*, **29**, 1807 (1984).
- [59] W. Q. Ma, R. Nötzel, M. Ramsteiner, U. Jahn, H.-P. Schönherr, H. Kostial, and K. H. Ploog *Appl. Phys. Lett.*, **75**, 1836 (1999).
- [60] N. Sakamoto, K. Hirakawa, and T. Ikoma *Appl. Phys. Lett.*, **67**, 1444 (1995).
- [61] F. Williams, in *Luminescence of inorganic solids*, edited by P. Goldberg, p. 42. New York and London: Akademie Press, 1966.
- [62] M. Gershenson, in *Luminescence of inorganic solids*, edited by P. Goldberg, p. 603. New York and London: Akademie Press, 1966.
- [63] L. O. Bubulac and W. E. Tennant *Appl. Phys. Lett.*, **52**, 1255 (1988).
- [64] G. Panin *Semicond. Sci. Technol.*, **7**, A150 (1992).

- [65] H. T. Lin, D. H. Rich, O. Sjölund, M. Ghisoni, and A. Larsson *Appl. Phys. Lett.*, **69**, 1602 (1996).
- [66] L. Reimer, *Scanning electron microscopy: physics of image formation and microanalysis*, p. 272. Berlin: Springer Verlag, 1966.
- [67] C. Díaz-Guerra and J. Piqueras *Appl. Phys. Lett.*, **71**, 2830 (1985).
- [68] H. Weman, E. Martinet, A. Rudra, and E. Kapon *Appl. Phys. Lett.*, **73**, 2959 (1998).
- [69] W. R. Tribe, M. J. Steer, D. J. Mowbray, M. S. Skolnick, A. N. Forshaw, J. S. Roberts, G. Hill, M. A. Pate, C. R. Whitehouse, and G. M. Williams *Appl. Phys. Lett.*, **70**, 993 (1997).
- [70] D. A. B. Miller, D. S. Chemla, and T. C. Damen *IEEE Quant. Electron.*, **QE-21**, 1462 (1985).
- [71] D. A. B. Miller, D. S. Chemla, and S. Schmitt-Rink *Appl. Phys. Lett.*, **52**, 2154 (1988).
- [72] H. Weman, E. Martinet, M.-A. Dupertuis, A. Rudra, K. Leifer, and E. Kapon *Appl. Phys. Lett.*, **74**, 2334 (1999).
- [73] T. Arakawa, Y. Kato, F. Sogawa, and Y. Arakawa *Appl. Phys. Lett.*, **70**, 646 (1997).
- [74] H.-J. Polland, L. Schultheis, J. Kuhl, E. O. Göbel, and C. W. Tu *Phys. Phys. Lett.*, **55**, 2610 (1985).
- [75] Y. Zhang, D. Jiang, F. Li, R. Wu, J. Zhou, and X. Mei *Phys. Phys. B*, **48**, 12296 (1993).
- [76] M. Copel, R. Kaxiras, and R. M. Tromp *Phys. Rev. Lett.*, **63**, 632 (1989).
- [77] E. Bauer and J. H. van der Merwe *Phys. Rev. B*, **33**, 3657 (1986).
- [78] Y. Okada, S. Ohta, H. Shimomura, A. Kawabata, and M. Kawabe *Jpn. J. Appl. Phys.*, **32**, L1556 (1993).
- [79] Y. J. Chun, Y. Okada, and M. Kawabe *Jpn. J. Appl. Phys.*, **32**, L1085 (1999).
- [80] Y. Okada, H. Shimomura, and M. Kawabe *J. Appl. Phys.*, **73**, 7376 (1993).
- [81] Y. J. Chun, Y. Okada, and M. Kawabe *J. Cryst. Growth*, **150**, 497 (1992).
- [82] Y. Okada, T. Fujita, and M. Kawabe *Appl. Phys. Lett.*, **67**, 676 (1995).
- [83] Y. Okada and S. Harris *J. Vac. Sci. Technol. B*, **14**, 1725 (1996).
- [84] R. R. LaPierre, B. J. Robinson, and D. A. Thompson *J. Cryst. Growth*, **191**, 319 (1998).
- [85] H.-P. Schönherr, J. Fricke, Z. C. Niu, K.-J. Friedland, R. Nötzel, and K. H. Ploog *Appl. Phys. Lett.*, **72**, 566 (1998).
- [86] R. Nötzel, H.-P. Schönherr, Z. C. Niu, L. Däweritz, and K. H. Ploog *J. Cryst. Growth*, **201/202**, 814 (1999).
- [87] Y. J. Chun, T. Sugaya, Y. Okada, and M. Kawabe *Jpn. J. Appl. Phys.*, **32**, L287 (1993).
- [88] Y. Ide and M. Yamada *J. Vac. Sci. Technol. A*, **12**, 1858 (1993).
- [89] R. Nötzel, J. Temmyo, and T. Tamamura *Appl. Phys. Lett.*, **64**, 3557 (1994).

- [90] P. O. Vaccaro, K. Fujita, and T. Watanabe *Jpn. J. Appl. Phys.*, **36**, 1948 (1997).
- [91] P. O. Vaccaro, M. Hirai, K. Fujita, and T. Watanabe *J. Phys. D: Appl. Phys.*, **29**, 2221 (1996).
- [92] R. Nötzel, Z. C. Niu, M. Ramsteiner, H.-P. Schönherr, A. Trampert, L. Däweritz, and K. H. Ploog *Nature*, **392**, 56 (1998).
- [93] R. Nötzel, N. N. Ledentsov, L. Däweritz, M. Hohenstein, and K. H. Ploog *Phys. Rev. Lett.*, **67**, 3812 (1991).
- [94] M. Wassermeier, J. Sudijono, M. D. Johnson, K. T. Leung, B. G. Orr, L. Däweritz, and K. H. Ploog *Phys. Rev. B*, **51**, 14721 (1995).
- [95] C. W. Snyder, J. F. Mansfield, and B. G. Orr *Phys. Rev. B*, **46**, 9551 (1992).
- [96] Y. Morishita, Y. Nomura, S. Goto, and Y. Katayama *Appl. Phys. Lett.*, **67**, 2500 (1995).
- [97] R. Kern, G. L. Lay, and J. J. Metois, *Basic mechanisms in the early stages of epitaxy: Current Topics in Materials Science*, ch. 3. Amsterdam: North-Holland, 1979.
- [98] A. Zangwill, *Epitaxy: Physics at Surfaces*, ch. 3, p. 421. New York: Cambridge University Press, 1988.
- [99] K. Binder *Phys. Rev. B.*, **37**, 1745 (1988).
- [100] E. Bauer and H. Poppa *Thin Solid Films*, **12**, 167 (1972).
- [101] M. Zinke-Allmang, L. C. Feldman, and M. H. Grabow *Surf. Sci. Reports*, **16**, 377 (1992).
- [102] R. Heitz, T. R. Ramachandran, A. Kalburge, Q. Xie, I. Mukhametzhanov, P. Chen, and A. Madhukar *Phys. Rev. Lett.*, **78**, 4071 (1997).
- [103] B. J. Spencer, P. W. Voorhees, and S. H. Davis *Phys. Rev. Lett.*, **67**, 3696 (1991).
- [104] W. H. Yang and D. J. Srolovitz *Phys. Rev. Lett.*, **71**, 1593 (1993).
- [105] G. Patriarche, A. Ougazzaden, and F. Glas *Appl. Phys. Lett.*, **76**, 306 (2000).
- [106] D. J. Eaglesham and M. Cerullo *Phys. Rev. Lett.*, **64**, 1943 (1990).
- [107] S. Guha, A. Madhukar, and K. C. Rajkumar *Appl. Phys. Lett.*, **57**, 2110 (1990).
- [108] T. S. Kuan and S. S. Iyer *Appl. Phys. Lett.*, **59**, 2242 (1990).
- [109] Y.-M. Mo, D. E. Savage, B. S. Swartzentruber, and M. G. Lagally *Phys. Rev. Lett.*, **65**, 1020 (1990).
- [110] J. Tersoff and F. K. LeGoues *Phys. Rev. Lett.*, **72**, 3570 (1994).
- [111] C. W. Snyder, B. G. Orr, D. Kessler, and L. M. Sander *Phys. Rev. Lett.*, **66**, 3032 (1991).
- [112] D. E. Jesson, S. J. Pennycook, J.-M. Baribeau, and D. C. Houghton *Phys. Rev. Lett.*, **71**, 1744 (1994).
- [113] A. G. Cullis, A. J. Pidduck, and M. T. Emeny *J. Cryst. Growth*, **158**, 15 (1996).
- [114] J. Y. Yao, T. G. Andersson, and G. L. Dunlop *J. Appl. Phys.*, **69**, 2224 (1991).

- [115] B. J. Spencer and J. Tersoff *Phys. Rev. Lett.*, **79**, 4858 (1997).
- [116] G. S. Solomon, J. A. Trezza, and J. S. Harris Jr. *Appl. Phys. Lett.*, **66**, 991 (1995).
- [117] J. M. García, G. Medeiros-Ribeiro, K. Schmidt, T. Ngo, J. L. Feng, A. Lorke, J. Kotthaus, and P. M. Petroff *Appl. Phys. Lett.*, **71**, 2014 (1997).
- [118] S. A. Chaparro, Y. Yang, J. Drucker, D. Chandrasekhar, and D. J. Smith *J. Appl. Phys.*, **87**, 2245 (2000).
- [119] J. Shigetomi, K. Fuwa, S. Shimizu, and H. Yamakawa *J. Cryst. Growth*, **111**, 110 (1991).
- [120] P. I. Cohen, G. S. Petrich, and G. J. Whaley, in *Molecular beam epitaxy: applications to key materials*, edited by R. F. C. Farrow, p. 669. New Jersey: Noyes Publications, 1995.
- [121] P. J. Dobson, in *Surface and interface characterization by electron optical methods*, edited by A. Howie and U. Valdrè, p. 159. New York: Plenum Press, 1988.
- [122] P. J. Dobson, B. A. Joyce, J. H. Neave, and J. Zhang, in *Surface and interface characterization by electron optical methods*, edited by A. Howie and U. Valdrè, p. 185. New York: Plenum Press, 1988.
- [123] J. J. Harris, B. A. Joyce, and P. J. Dobson *Surf. Sci.*, **103**, L90 (1981).
- [124] W. Braun. PhD thesis, Humboldt-Universität zu Berlin, 1996.
- [125] L. Däweritz and R. Hey *Surf. Sci.*, **236**, 15 (1990).
- [126] N. S. Chokshi and J. M. Millunchick *Appl. Phys. Lett.*, **76**, 2382 (2000).
- [127] J. Tersoff and R. M. Tromp *Phys. Rev. Lett.*, **70**, 2782 (1993).
- [128] B. J. Spencer and J. Tersoff *Phys. Rev. Lett.*, **79**, 4858 (1997).
- [129] C. D. Rudin and B. J. Spencer *J. Appl. Phys.*, **86**, 5530 (1999).
- [130] I. Daruka, J. Tersoff, and A.-L. Barabási *Phys. Rev. Lett.*, **82**, 2753 (1999).
- [131] S. H. Brongersma, M. R. Castell, D. D. Perovic, and M. Zinke-Allmang *Phys. Rev. Lett.*, **80**, 3795 (1998).
- [132] G. E. Cirlin, G. M. Guryanov, A. O. Golubok, S. Y. Tapishev, N. N. Ledentsov, P. S. Kop'ev, M. Grundmann, and D. Bimberg *Appl. Phys. Lett.*, **67**, 97 (1995).
- [133] N. Moll, M. Scheffler, and E. Pehlke *Phys. Rev. B.*, **58**, 4566 (1998).
- [134] N. Moll, A. Kley, E. Pehlke, and M. Scheffler *Phys. Rev. B.*, **54**, 8844 (1996).
- [135] H. van Beijeren and I. Nolden, *The roughening transition in Structure and dynamics of surfaces II*, ch. 3, p. 259. Berlin: Springer Verlag, 1987.
- [136] J. Tersoff, in *Low dimensional structures prepared by epitaxial growth or regrowth on patterned substrates*, edited by K. Eberl and P. M. Petroff and P. Demeester, p. 13. Dordrecht: Kluwer Academic Publishers, 1995.
- [137] R. Nötzel *Semicond. Sci. Technol.*, **11**, 1365 (1996).

- [138] Q. Xie, A. Madhukar, P. Chen, and N. Kobayashi *Phys. Rev. Lett.*, **75**, 2542 (1995).
- [139] J. Tersoff, C. Teichert, and M. G. Lagally *Phys. Rev. Lett.*, **76**, 1675 (1996).
- [140] W. Q. Ma, R. Nötzel, A. Trampert, M. Ramsteiner, H. J. Zhu, H.-P. Schönherr, and K. H. Ploog *Appl. Phys. Lett.*, **78**, 1297 (2001).
- [141] S. T. Picraux, B. L. Doyle, and J. Y. Tsao, in *Strained-layer superlattices: materials science and technology*, edited by T. P. Pearsall, p. 139. San Diego: Academic Press, INC, 1991.
- [142] L. Tapfer, in *III-V quantum system research*, edited by K. H. Ploog, p. 225. London: Peter Peregrinus Ltd., on behalf of The Institution of Electrical Engineers, 1995.
- [143] B. K. Tanner and D. K. Bowen *J. Cryst. Growth*, **126**, 1 (1993).
- [144] P. F. Fewster *Semicond. Sci. Technol.*, 8 (1993).
- [145] P. F. Fewster *J. Appl. Cryst.*, **25**, 714 (1992).
- [146] N. Itoh and K. Okamoto *J. Appl. Phys.*, **25**, 714 (1992).
- [147] C. Kittel, *Introduction to Solid State Physics*. New York: John Wiley, 1976.
- [148] W. H. Zachariasen, *Theory of x-ray diffraction in crystals*. New York: John Wiley, 1945.
- [149] D. M. Vardanyan, H. M. Manoukyan, and H. M. Petrosyan *Acta. Cryst.*, **A41**, 212 (1985).
- [150] D. M. Vardanyan, H. M. Manoukyan, and H. M. Petrosyan *Acta. Cryst.*, **A41**, 218 (1985).
- [151] W. J. Bartels, J. Hornstra, and D. J. W. Lobeek *Acta. Cryst.*, **A42**, 539 (1986).
- [152] A. M. Mathieson *Acta. Cryst.*, **A38**, 378 (1982).
- [153] V. S. Speriosu *J. Appl. Phys.*, **52**, 6094 (1981).
- [154] V. S. Speriosu and T. J. Vreeland *J. Appl. Phys.*, **56**, 1591 (1984).
- [155] L. Tapfer and K. H. Ploog *Phys. Rev. B.*, **33**, 5565 (1986).
- [156] A. T. Macrander and S. E. G. Slusky *Appl. Phys. Lett.*, **56**, 443 (1990).
- [157] L. Tapfer and P. Grambow *Appl. Phys. A.*, **50**, 3 (1990).
- [158] L. Tapfer, G. C. L. Rocca, H. Lage, O. Brandt, D. Heitmann, and K. H. Ploog *Appl. Surf. Sci.*, **267**, 227 (1992).
- [159] L. D. Caro, P. Sciacovelli, and L. Tapfer *Appl. Phys. Lett.*, **64**, 34 (1994).
- [160] Q. Shen, C. C. Umbach, B. Weselak, and J. M. Blakely *Phys. Rev. B.*, **48**, 17967 (1993).
- [161] V. Holý, A. A. Darhuber, and G. Bauer *Phys. Rev. B.*, **52**, 8348 (1995).
- [162] A. Krost, F. Heinrichsdorff, and Bimberg *Appl. Phys. Lett.*, **68**, 785 (1996).
- [163] B. Jenichen and K. H. Ploog *Appl. Phys. Lett.*, **63**, 156 (1993).

- [164] A. Krost, G. Bauer, and J. Woitok, in *Optical characterization of epitaxial semiconductor layers*, edited by G. Bauer and W. Richter, p. 365. Berlin-Heidelberg: Springer-Verlag, 1996.
- [165] A. Howie, in *Surface and interface characterization by electron optical methods*, edited by A. Howie and U. Valdrè, p. 1. New York: Plenum Press, 1988.
- [166] R. Hull and J. C. Bean, *Strained-layer superlattice: materials science and technology*, edited by T. P. Pearsall, p. 1. San Diego: Academic Press, INC, 1991.
- [167] D. S. Citrin and Y. C. Chang *Phys. Rev. B.*, **43**, 11703 (1991).
- [168] F. Vouilloz, D. Y. Oberli, M.-A. Dupertuis, A. Gustafsson, F. Reinhardt, and E. Kapon *Phys. Rev. Lett.*, **78**, 1580 (1997).
- [169] H. Weman, D. Y. Oberli, M.-A. Dupertuis, F. Reinhardt, A. Gustafsson, and E. Kapon *Phys. Rev. B.*, **58**, 1150 (1998).
- [170] H. Akiyama, T. Someya, and H. Sakaki *Phys. Rev. B.*, **53**, R4229 (1996).
- [171] T. Uenoyama and L. J. Sham *Phys. Rev. Lett.*, **64**, 3070 (1990).
- [172] C. Pryor *Phys. Rev. B.*, **44**, 12912 (1991).
- [173] Y. Qian, L. Chen, and Q. Wang *Solid State Communications*, **87**, 285 (1993).
- [174] P. C. Sercel and K. J. Vahala *Appl. Phys. Lett.*, **57**, 545 (1990).
- [175] U. Bockelmann and G. Bastard *Phys. Rev. B.*, **45**, 1688 (1992).
- [176] M. Notomi, J. Hammersberg, J. Zeman, H. Weman, M. Potemski, H. Sugiura, and T. Tamamura *Phys. Rev. Lett.*, **80**, 3125 (1998).
- [177] I. Vurgaftman and J. Singh *J. Appl. Phys.*, **77**, 4931 (1995).
- [178] E. Martinet, M.-A. Dupertuis, F. Reinhardt, G. Biasiol, and E. Kapon *Phys. Rev. B.*, **61**, 4488 (2000).
- [179] Y. Nagamune, Y. Arakawa, S. Tsukamoto, M. Nishioka, S. Sasaki, and N. Miura *Phys. Rev. Lett.*, **69**, 2963 (1992).
- [180] U. Bockelmann and G. Bastard *Phys. Rev. B.*, **45**, 1700 (1992).
- [181] K. J. Nash, M. S. Skolnick, P. A. Claxton, and J. S. Roberts *Phys. Rev. B.*, **39**, 10943 (1989).
- [182] M. Notomi, J. Hammersberg, H. Weman, S. Nojima, H. Sugiura, M. Pkamoto, T. Tamamura, and M. Potemski *Phys. Rev. B.*, **52**, 11147 (1995).
- [183] T. Someya, H. Akiyama, and H. Sakaki *Phys. Rev. B.*, **52**, 11147 (1995).
- [184] M. Bayer, P. Ils, M. Michel, A. Forchel, T. L. Reinecke, and P. A. Knipp *Phys. Rev. B.*, **53**, 4668 (1996).
- [185] J. Hammersberg, H. Weman, M. Notomi, and Tamamura *Superlattices and Microstructures*, **16**, 143 (1994).
- [186] H. Weman, E. D. Jones, C. R. McIntyre, M. S. Miller, P. M. Petroff, and J. L. Merz *Superlattices and Microstructures*, **13**, 5 (1993).

- [187] M. Kohl, D. Heitmann, P. Grambow, and K. H. Ploog *Phys. Rev. Lett.*, **63**, 2124 (1989).
- [188] M. Notomi, M. Okamoto, H. Iwamura, and T. Tamamura *Appl. Phys. Lett.*, **62**, 1094 (1993).
- [189] Y. Nabetani, T. Ishikawa, S. Noda, and A. Sasaki *J. Appl. Phys.*, **76**, 347 (1994).
- [190] J. A. Prieto, G. Armelles, C. Priester, J. M. García, L. González, and R. García *Appl. Phys. Lett.*, **76**, 2197 (2000).
- [191] D. L. Smith *Solid State Commun.*, **57**, 919 (1986).
- [192] D. L. Smith and C. Mailhot *Phys. Rev. Lett.*, **58**, 1264 (1987).
- [193] C. Mailhot and D. L. Smith *Phys. Rev. B.*, **37**, 10415 (1988).
- [194] T. S. Moise, L. J. Guido, R. C. Barker, J. O. White, and A. R. Kost *Appl. Phys. Lett.*, **60**, 2637 (1992).
- [195] R. André, C. Deshayes, J. Cibert, L. S. Dang, S. Tatarenko, and K. Saminadayar *Phys. Rev. B.*, **42**, 11392 (1990).
- [196] J. A. Prieto, G. Armelles, J. Groenen, and R. Carles *Appl. Phys. Lett.*, **74**, 99 (1999).
- [197] E. A. Caridi, T. Y. Chang, K. W. Goossen, and L. F. Eastman *Appl. Phys. Lett.*, **56**, 659 (1990).
- [198] X. R. Huang, D. R. Harken, A. N. Cartwright, A. L. Smirl, J. L. Sánchez-Rojas, A. Sacedó, E. Calleja, and E. Muñoz *Appl. Phys. Lett.*, **67**, 950 (1995).
- [199] K. W. Goossen, E. A. Caridi, T. Y. Chang, J. B. Stark, D. A. B. Miller, and R. A. Morgen *Appl. Phys. Lett.*, **56**, 715 (1990).
- [200] P. Boring, B. Gil, and K. J. Moore *Phys. Rev. Lett.*, **71**, 1875 (1993).
- [201] B. K. Laurich, K. Elcess, C. G. Fonstad, J. G. Beery, C. Mailhot, and D. L. Smith *Phys. Rev. Lett.*, **62**, 649 (1989).
- [202] J. D. Bruno and R. L. Tober *J. Appl. Phys.*, **85**, 2221 (1999).
- [203] E. A. Khoo, J. P. R. David, J. Woodhead, R. Grey, and G. J. Rees *Appl. Phys. Lett.*, **75**, 1929 (1999).
- [204] A. Ramakrishnan, J. Wagner, M. Kunzer, H. Obloh, K. Köhler, and B. Johs *Appl. Phys. Lett.*, **76**, 79 (2000).
- [205] E. Anastassakis *Phys. Rev. B.*, **46**, 4744 (1992).
- [206] L. D. Caro and L. Tapfer *Phys. Rev. B.*, **48**, 2298 (1993).
- [207] D. L. Smith *Microelectronics J.*, **28**, 707 (1997).
- [208] F. H. Pollak and M. Cardona *Phys. Rev.*, **172**, 816 (1968).
- [209] M. Ilg, K. H. Ploog, and A. Trampert *Phys. Rev. B.*, **50**, 17111 (1994).
- [210] P. O. Vaccaro, M. Takahashi, K. Fujita, and T. Watanabe *Jpn. J. Appl. Phys.*, **34**, L13 (1995).

- [211] R. Nötzel, M. Ramsteiner, Z. C. Niu, H.-P. Schönherr, L. Däweritz, and K. H. Ploog *Appl. Phys. Lett.*, **70**, 1578 (1997).
- [212] R. Rincón, C. Priester, G. Fierling, X. Letartre, and P. Viktorovitch *Microelectronics J.*, **28**, 1031 (1997).

*

Acknowledgments

I got much help from many people during this work. First, I would like to thank my advisor, Prof. Dr. K. H. Ploog for his continuous support and guidance and encouragements. Second, I would like to thank Dr. R. Nötzel. Many ideas were created from the frequent discussions, and, more recently, e-mail correspondence with him. I also thank him for the careful reading of the thesis.

I wish to thank Mr. H.-P. Schönherr for his constant technical support. If there were not his careful maintenance of the MBE system, this work would have been difficult. I want to thank Dr. M. Ramsteiner and Dr. U. Jahn. I got much help from Dr. Ramsteiner for the optical measurements. The EBIC results were contributed by Dr. Jahn. It was always a pleasant time to discuss and talk with them.

I want to thank our group leader, Dr. L. Däweritz, for the frequent discussions about my work and for the careful reading of the thesis. I thank Dr. A. Trampert for the TEM measurements. Frau Wiebicke prepared the patterned GaAs(311)A substrates. Dr. H. Kostial helped with the Ohmic contacts of the LEDs. I also got help from many other colleagues. Here, I express my sincere thanks to them.

Finally, I want to thank my parents and Rongli.

List of Abbreviations and Symbols

AFM	atomic force microscopy
CL	cathodoluminescence
EBIC	electron beam induced current
EL	electroluminescence
GaAs(hkl)A	Ga terminated GaAs (hkl) surface
GaAs(hkl)B	As terminated GaAs (hkl) surface
LED	light emitting diode
MBE	molecular beam epitaxy
MOVPE	metalorganic vapor phase epitaxy
PL	photoluminescence
μ -PL	micro-photoluminescence
PLE	photoluminescence excitation
QCSE	quantum confined Stark effect
RHEED	reflection high energy electron diffraction
TEM	transmission electron microscopy
XRD	x-ray diffraction
C_{11}, C_{12}	elastic moduli
e	electron charge
e_{14}	piezoelectric constant
h	Plank's constant
\hbar	Plank's constant divided by 2π
k	Boltzmann's constant
m_0	free electron mass
ε_{ij}	strain tensor
ν	Poisson ratio
μ	shear modulus
θ_B	kinematical Bragg angle

Publications

W. Q. Ma, R. Nötzel, M. Ramsteiner, U. Jahn, H.-P. Schönherr, H. Kostial, and K. H. Ploog, *Selective electroluminescence from a single stack of sidewall quantum wires on patterned GaAs (311)A substrates*, Appl. Phys. Lett. **75**, 1836 (1999).

W. Q. Ma, R. Nötzel, A. Trampert, M. Ramsteiner, H.-J. Zhu, H.-P. Schönherr, and K. H. Ploog, *Self-organized quantum wires formed by elongated dislocation-free islands in (In,Ga)As/GaAs(100)*, Appl. Phys. Lett. **78**, 1297 (2001).

H.-P. Schönherr, R. Nötzel, W. Q. Ma, and K. H. Ploog, *Evolution of the surface morphology of Fe grown on GaAs (100), (311)A, and (331)A substrates by molecular beam epitaxy*, J. Appl. Phys. **89**, 169 (2001).

W. Q. Ma, R. Nötzel, H.-P. Schönherr, and K. H. Ploog, *Shape transition of coherent three-dimensional (In,Ga)As islands on GaAs(100)*, Appl. Phys. Lett. (to be published).

Curriculum vitae

Name: Wenquan Ma
Date of Birth: March 22, 1968
Birthplace: Gansu, P. R. China
1975 - 1980 primary school
1981 - 1986 middle school
9/1986 - 7/1990 undergraduate student
majoring in semiconductor devices,
in physics department
of Lanzhou University, P. R. China
7/1990 - 5/1994 Tianguang Integrated Circuit
Manufacturer, P. R. China
work area: design of the mask for
TTL, LSTTL IC, photolithography
7/1994 - 7/1995 MSc student in Graduate School,
Chinese Academy of Sciences
7/1995 - 7/1997 MSc student in Institute of Semiconductors,
Chinese Academy of Sciences
speciality: Structural characterization
of superlattice and quantum wires
by double crystal and triple-axis
x-ray diffractometries
4/1998 - 3/2001 PhD student in
Paul-Drude-Institut für Festkörperelektronik
speciality:
fabrication and properties of quantum wires

Selbständigkeitserklärung

Hiermit erkläre ich, die vorliegende Arbeit selbständig und ohne unerlaubte Hilfe angefertigt zu haben.

Ich habe mich anderwärts nicht um einen Doktorgrad beworben und besitze einen entsprechenden Doktorgrad nicht.

Ich erkläre die Kenntnisnahme der dem Verfahren zugrunde liegenden Promotionsordnung der Mathematisch-Naturwissenschaftlichen Fakultät I der Humboldt-Universität zu Berlin.

Wenquan Ma
Berlin, February 20th, 2001